JPRS-CST-86-031

7 AUGUST 1986
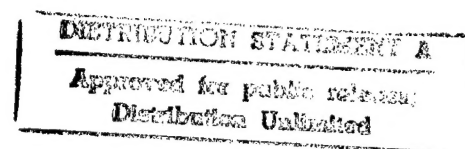
CHINA REPORT

SCIENCE AND TECHNOLOGY

19981021 115

FOREIGN BROADCAST INFORMATION SERVICE

NOTE

PROCUREMENT OF PUBLICATIONS

CHINA REPORT

SCIENCE AND TECHNOLOGY

CONTENTS

PEOPLE'S REPUBLIC OF CHINA

PHYSICAL SCIENCES

/12223

EXISTENCE SEEN OF CYCLONIC EDDY IN NORTHERN EAST CHINA SEA

[Article by Zaho Baoren [6392 0202 0088] of Institute of Oceanography at Qingdao, Chinese Academy of Sciences: "Recent Observation Evidence on the Presence of Cyclonic Eddy in the Northern Part of East China Sea"]

[Text] Abstract: This paper briefly summarizes the results of the surveys conducted in the cyclonic eddy zone in northern East China Sea in recent years. Based on the temperature field, mass field and flow field measured in these surveys, cyclonic eddy did exist in the area southwest of Cheju Island during the period. The residual current vector obtained in the survey was plotted with those measured in the past in the same season, resulting in a complete cyclonic eddy flow field. In addition, fundamental characteristics of the Huanghai Sea coastal current in northern East China Sea is also discussed. Our results further confirm that the diagnosis that this cyclonic eddy exists year round and its position is stable is correct.

Based on temperature, salinity and current data gathered in July-August 1972, Hu Dunxin [5170 2415 2946] et al [2,3] pointed out in 1980 that a cyclonic eddy, approximately 60-90 nautical miles in diameter and 40 m in verticle scale, exists southwest of Cheju Island. In 1983, Mao Hanli [3029 3352 4409] et al further confirmed that this cyclonic eddy in northern East China Sea exists year round. In addition, the variation of this eddy in the summer season over the years was discussed based on the temperature field[5,6]. All authors mentioned above believes that the principal reason for the presence of this eddy is due to the horizontal velocity shear of the Huanghai Sea warm current and Huanghai Sea coastal current.

Based on historic data, considerable information on the current north, east and south of the eddy is available. According to the vector diagram thus prepared, the flow field shows a tendency to rotate as a cyclonic eddy. Furthermore, these current vectors are consistent with other currents in the area such as the Taiwan Warm Current, Tsushima Warm Current and Huanghai Sea Warm Current. On

the west side, i.e. the area reached by Hunghai Sea *cold Current and Coastal Current, however, there is relatively little information on the currents in that area. Hence, there are questions and doubts concerning whether there is a cyclonic eddy southwest of Cheju Island. To this end, we conducted three surveys on the hydrologic characteristics of the eddy in recent years. The focus of the measurements was to clarify the currents on the west side of the eddy.
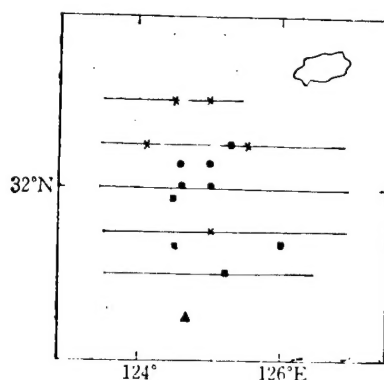
Figure 1. The Survey Area[1)]

Key:
- • buoy; current measuring station in July 1982
- ▪ current measuring station in April 1984
- ▲ buoy installed in joint Chinese-American survey in June 1980
- — cross-section position

1) A buoy station installed during the joint Chinese-American survey in June 1980 is also included in the fugure.

The hydrologic cross-sections and current measuring stations in these three surveys are shown in Figure 1. Based on an analysis, the flow of the Huanghai Sea Cold Current in the northern part of East China Sea was more or less understood. Once again, we proved that there is a cyclonic eddy in northern East China Sea southwest of Cheju Island. These observation results will be briefly discussed in this paper.

––––––––––––––––––––

2

A. The Three Marine Surveys

1. Results of Observation in July 1980

The survey results centered around buoy arrays deployed in July 1980 were
analyzed in detail in references [1,4]. References [5,6] also used some of the
results. Hence, only a brief introduction is given here. Figures 2a and 2b
show the temperature distribution and dynamic height distribution of the 10 m
layer as measured in July 1980, respectively, as well as the average flow
velocity vector of the 10 m layer as determined by an anchored array of buoys.
In addition, we also included the average velocity vectors of the 14 m and 17 m
layers obtained in the Chinese-American joint survey of the mouth of
Changjiang River (from early to late June 1980)[7]. Based on Figure 2 we can
see that (1) there is a cold center southwest of Cheju Island (125°30'E, 31°N).
The lowest temperature is 19.2°C which is at least 2.7°C lower than those
measured in surrounding stations. It was also found that the salinity in this
cold center is 3.32 percent which is .15 percent higher than those measured in
nearby stations. In the dynamic height plot, there is a corresponding closed
contour. The Huanghai Sea Warm Current flows by the east and north sides of
this contour, as shown in Figure 2 in reference [3], where there is an even
higher dynamic height line. Hence, if we set up hydrological stations in this
region, there will be more enclosed contours. The geostrophic cold water cir-
culation will be clearer than that shown in Figure 2. (2) Based on the measured
flow velocity vectors, the measured flow is very close to the geostrophic flow
not only in direction but also in quantity. This fact shows that a geostrophic
flow field can be used to approximately express the seawater flow in this
region, at least in the summer. (3) As compared to the temperature chart
(Figure 2a in this paper and Figure in reference [4]), the direction of the
geostrophic current in the middle upper level and that of the measured residual
current are in agreement with that of the isothermal lines in the area west of
126°E. There is an overall tendency for the cold current of the Huanghai Sea to
move southward. This shows that there is indeed a cyclonic cold eddy in the
northern part of the East China Sea southeast of Cheji Island.
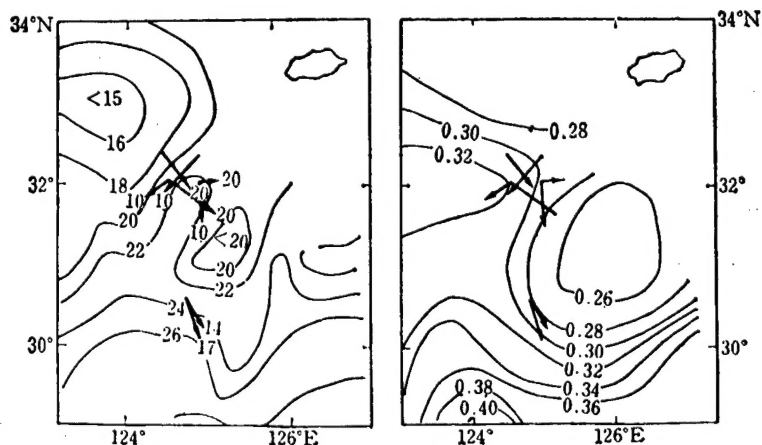
Figure 2. Temperature, Dynamic Height Distribution and Measured Flow Speed at
10 m Depth in July 1980. a. Temperature distribution; b. dynamic height dis-
tribution (vectors shows are measured residual currents and values shown near the
vectors are water depth levels.)

3

2. Results of Observation in July 1982

In order to further understand the hydrological structure of this eddy region in the summer and the flow west of this area, the survey vessel "Science 1" conducted a hydrological survey in July 1980. Figures 3a and b are the salinity distributions at 20 m and 35 m levels. Based on Figure 3, on the east side of the area surveyed, a cold center with an enclosed isotherm was found at 20 m. Its temperature is at least 5°C lower and its salinity is at least .05 percent higher than its surrounding environment. The center of this cold water region is located near 31°30'N and 125°45'E. At 35 m depth, this cold center has already shifted northward by about 1 degree latitude to 32°30'N and 126°00'E. In addition, we can also see that there is a warm water tongue north of the cold center extending southwestward. This type of warm water tongue has been found several times before such as in July 1973 and June 1979[1]. We believe that this is due to the branching of the Huanghai Warm Current before entering the Huanghai Sea. It is called the west branch of the Huanghai Warm Current. It often partially or completely cuts off the southbound Huanghai Cold Water to create an isolated cold water zone southwest of Cheju Island.

Based on the residual current vectors shown in Figure 3 (Figure 3b shows vectors at 30 m depth), the flow direction is south on the west side of the cold center, which more or less agrees with the temperature distribution. Based on the data shown in Figure 3a on the flow on either side of the warm water tongue, the residual currents at 20 m and 30 m are mostly southwest, approximately agreeing with the axis of the warm water tongue. Furthermore, the residual currents measured at the two most north stations showed eastward flow. Based on the temperature field, this was a sign that the cold water eddy of the Huanghai Sea reached there.

The cross-sectional diagram (Figure 4) shows that the high salinity cold water at the bottom is rising between 125° and 126°30'E. The cold water only reached 20 m level, lower than previous years.

In summary, in July 1982 the cross-sectional diagram clearly shows that cold water is rising. The horizontal chart shows a relatively strong high salinity cold center with an enclosed isotherm. Moreover, a warm water tongue extending southwestward was found on the northwest side of the cold center. Southward residual currents were measured west of the cold center. In addition, the direction of the residual current is more or less in agreement with the temperature field. Based on these facts, the cyclonic eddy did exist southwest of Chenju during this survey.

3. Results of Observation in July 1983

Based on the data gathered in the spring of 1973 (April-May), Mao Hanli[5,6] et all believed that a cyclonic eddy southwest of Cheju Islands also existed in the spring. As shown in Figure 3 of references [5,6], the residual current

---

1) Zhao Baoren, Current Structure in Cold Eddy Region in Northern East China Sea, [OCEAN AND LAKES], to be published.

distribution measured in April-May 1973 is located south, east and north of the eddy. There is no data west of the region. For this reason, we conducted another hydrological survey in this area in April 1983. Five ocean current observation stations were set up on the west side in order to gather data regarding the expansion of the Huanghai Cold Current into northern East China Sea in the spring.
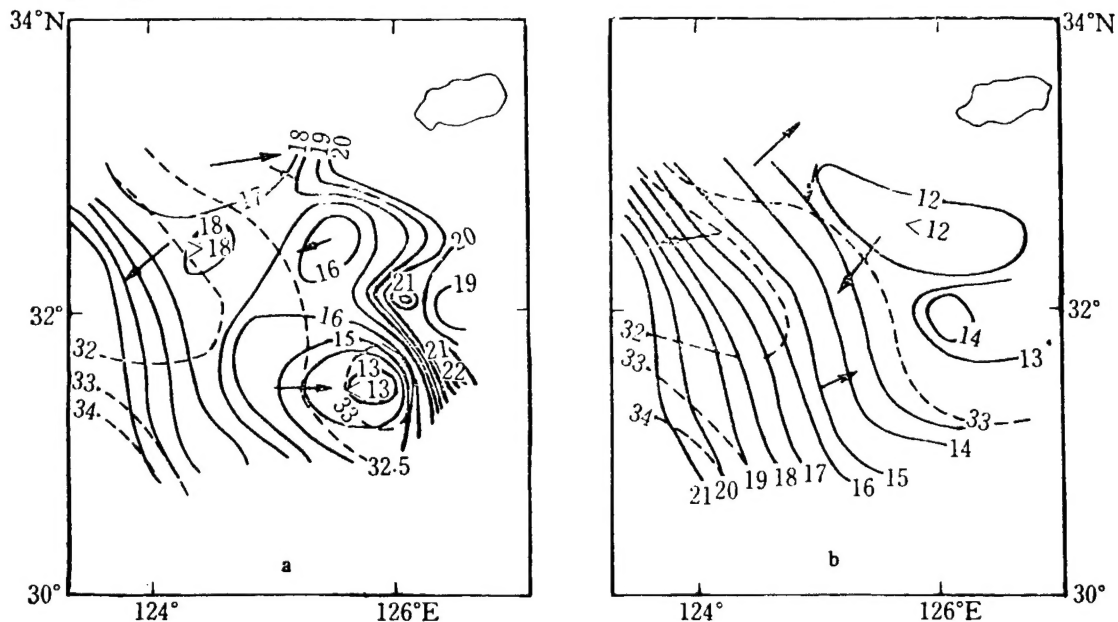
Figure 3. Horizontal Distribution of Temperature, Salinity and Residual Current in July 1982

a.   20 m depth   —— temperature
b.   35 m depth   --- salinity
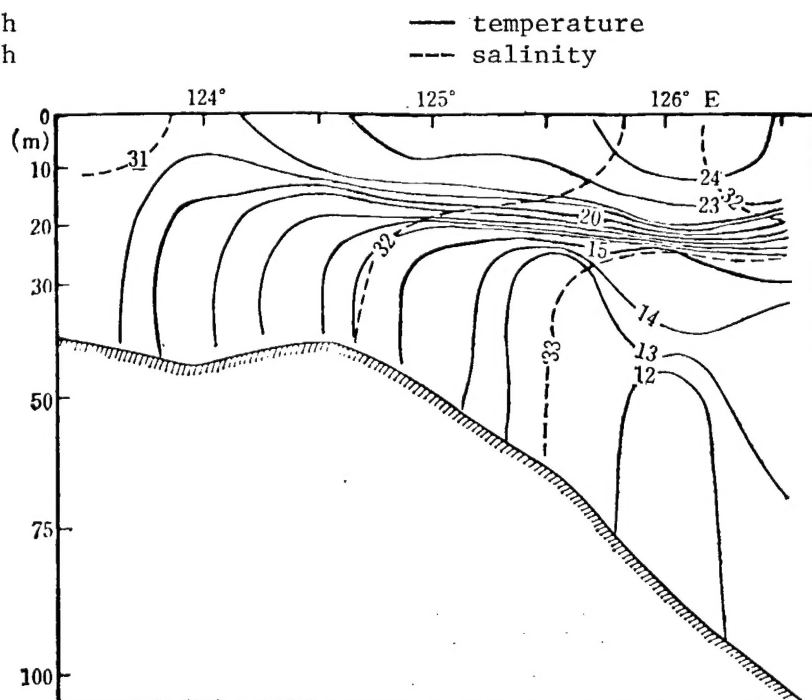
Figure 4. Temperature Cross-section at 32°N in July 1982

—— temperature
--- salinity
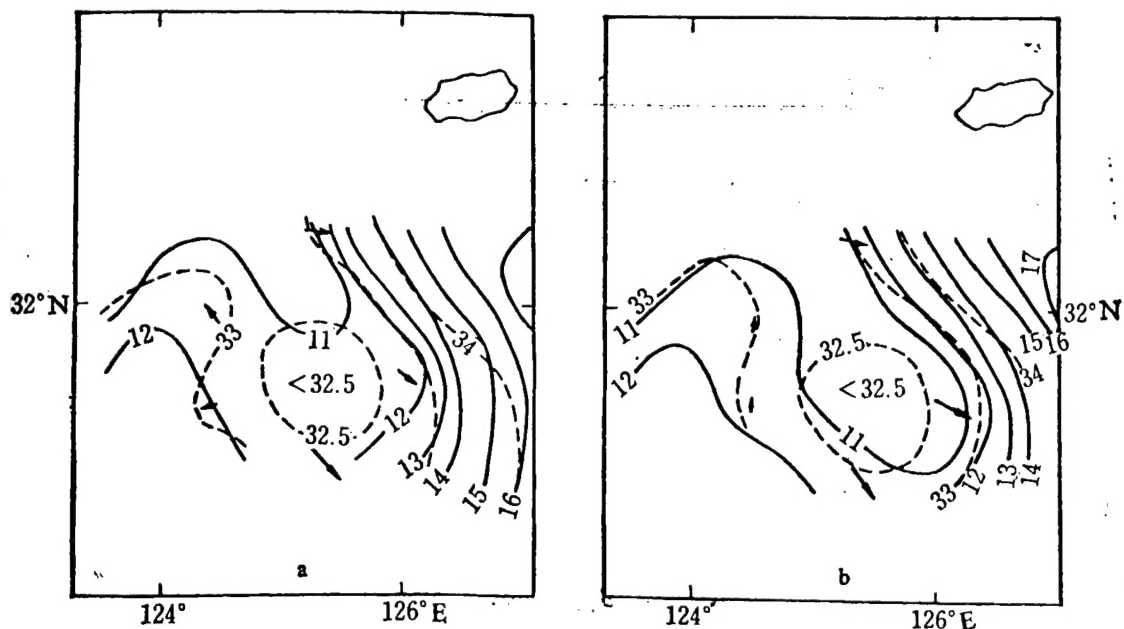
Figure 5. Temperature and Salinity Distribution and Residual Current in April 1983 (same as in Figure 3)

a. 20 m level
b. 35 m level
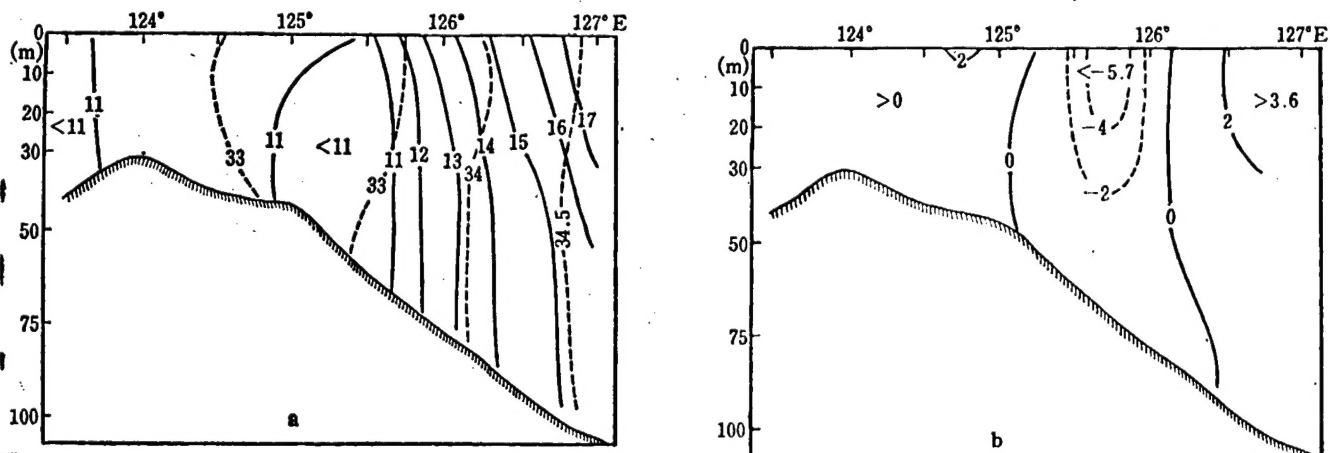
Figure 6. 32°N Cross-section Diagrams Obtained in April 1983

a. temperature and salinity
b. goestrophic flow speed

Figures 5a and b show the distributions of temperature, salinity and residual current vector obtained in this survey at 20 m and 30 m. Based on the figure, there is a low temperature, low salinity tongue in the middle of this area extending from NNW toward SSE. This shows the tendency for the low salinity

6

cold water of the Huanghai Sea to extend into northern East China Sea. On either side of this tongue, two high temperature, high salinity tongues are extending northward. The west one is due to the northward extension of the Taiwan Warm Current and the east one is due to the northwestward extension of the Huanghai Warm Current. From Figure 5 we can see that the two high temperature, high salinity tongues are approaching the cold water tongue north of 32°N. It is more apparent for the Huanghai Warm Current. Due to this effect, the low temperature, low salinity tongue south of 32°N appears as the head of a snake. Although temperature is rising in April, however, lamination effect is not obvious. From surface to bottom, the overall trend for horizontal distribution of temperature and salinity remains the same.
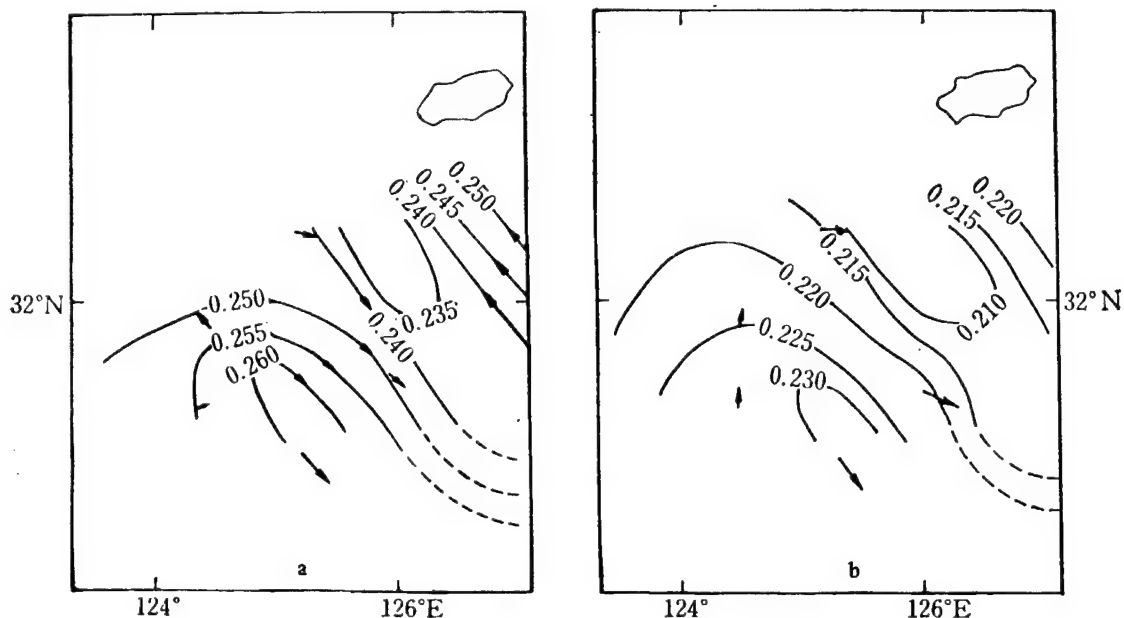
Figure 7. Dynamic Height Obtained in April 1983

a.   20 m level
b.   30 m level

The residual current vector obtained in this survey is relatively small, usually not more than 10 cm/s. Its direction is more or less in agreement with the tongue axis of temperature and salinity (see Figure 5). Dynamic calculation shows that the trend for geostrophic current in the cold water region agrees with that of the measured residual current. Based on Figure 6a, a low temperature, low salinity center exists at 125°-126°E. This is the bulk of the southward Huanghai Cold Current. From Figure 6b, the geostrophic current calculated to the right of this cold center moves southward and reaches a maximum. The calculated geostrophic currents on both sides are pointing northward. Thus, the geostrophic current pattern agrees with that based on the temperature and salinity tongue distribution. Similar tendency was found along several cross-sections in the south. The difference is that the center of the southward geostrophic current also moves southeastward as the cold center moves in the same direction.

Figure 7 shows the dynamic height obtained in this survey at 20 m and 30 m. Due to lack of data, only a partial elliptical cyclonic circulation is drawn southwest of Cheju. Considering the flow of the Huanghai Warm Current southwest of Cheju in the spring, it is possible to complete the ellipse. Hence, during this survey period the cyclonic eddy also existed.

II.   Huanghai Coastal Current in Northern East China Sea

There is a wide range of low salinity cold water in northern East China Sea. As for the important questions such as the dynamic nature of the area, how does it reach northern East China Sea, and how fast does it flow, some fundamental understanding has been obtained based on analyses of the three surveys.

Based on Figure 2, the summer Huanghai Coastal Current flows southeastward with the cold water density circulation in southern Huanghai Sea. When it reaches the 32°N line east of 124°E, it is deflected toward the southeast on the west side of the cyclonic eddy described above. Then, it merges with the Taiwan Warm Current south of 31°N and east of 124°E and then moves toward southeast. Based on residual current vector measured, Huanghai Coastal Current reaches 10-15 m/s after it gets to East China Sea. It mixes with the surrounding seawater continuously. First, it mixes with the warm water carried by the western branch of the Huanghai Warm current near 32°N and then merges with Taiwan warm water further south (south of 31°N). In addition, the upper layer is mixed with the fresh water of the Changjiang River.

As described earlier, cold water is delivered to East China Sea by the spring Huanghai Coastal Current in the direction of the tongue axis (southeast). At this time, the direction of Huanghai Coastal Current is monotonous. It flows consistently southeastward from southern Huanghai to northern East China Sea. Based on the data and dynamic calculation, its flow speed can also reach 10 cm/s in the spring.

Based on a comparison of dynamic calculation and residual current measurement, in spring and summer, the Huanghai Coastal Current is basically geostrophically balanced as it moves south. But, the situation in spring is different from that in the summer. In spring, the temperature difference between the southbound cold water and the surrounding water is relatively small. Because of its apparent low salinity, although the Huanghai) Coastal Current is geostrophic, it moves along the axis of the temperature and salinity tongue. In summer, it moves southward along the west side of the cold center. At this time, the isotherms approximately reflects the geostrophic flow. We do not have any residual current data in fall and winter seasons. However, based on the geostrophic flow, its distribution in winter is more or less similar to those shown in Figures 6 and 7. In the fall, before the end of October, it is approximately the same as that in the summer. Thus, the coastal current in winter is expected to be the same as spring and the situation in the fall is similar to that in summer.

III.   Flow Field Measured in Eddy Region

Another important question to be explained is that whether the flow velocity vectors measured on the west side of the eddy agrees with other vectors observed

during the same period in the past. Figures 8 and 9 show the results combining the residual current vectors observed in the summer (solid lines) and those obtained in July-August 1972 (dotted lines). Figures 8a and 9a show the residual current distribution at 10 m and Figures 8b and 9b show that at 20 m. Based on these four figures, the residual current vectors observed in the summer of 1980 and 1982, together with those measured historically in the same period, form a complete cyclonic eddy motion. The center of the eddy is approximately located at 126°E and 31°30'N. The diameter of the eddy is 2 lattitude units. It should be pointed out that this situation not only occurs at 10 m and 20 m. From 5 m to 50 m, similar trend exists.
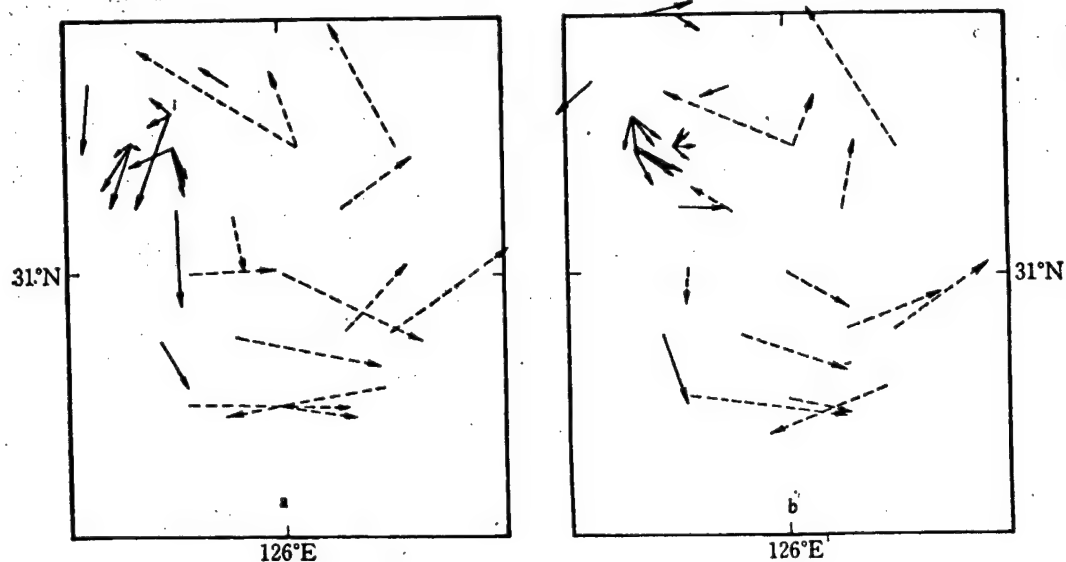
Figure 8. Residual Current Together with Data Obtained in Summer 1972

a. 10 m layer
b. 20 m layer
(Dotted vectors are 1972 summer data.)
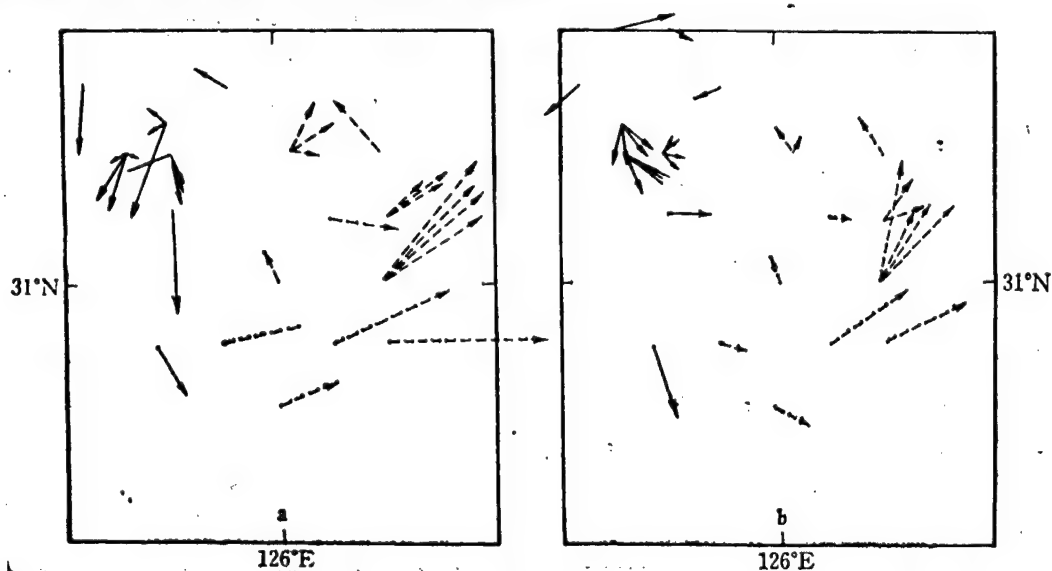
Figure 9. Measured Residual Current Combined with Summer 1973 Data.

a. 10 m layer
b. 20 m layer
(Dotted lines represent 1973 summer data.)

9
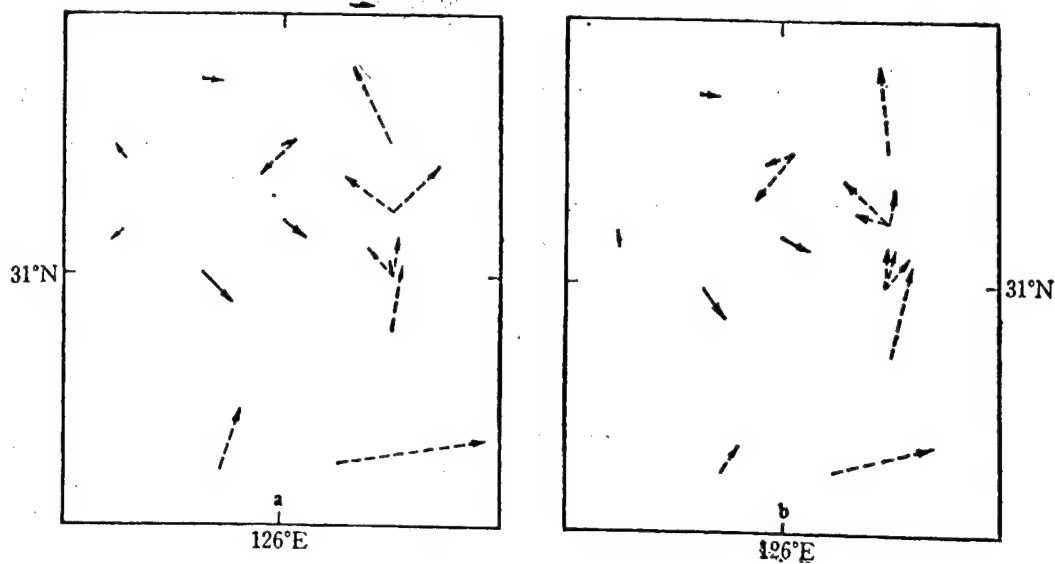
Figure 10. Measured Residual Current Combined with Spring 1973 Data

a. 20 m layer
b. 30 m layer
(Dotted lines represent spring 1973 data.)

Figure 10 shows the combination of the residual currents measured in April 1983 and April-May 1973. Based on the figure, similar to the summer flow field, the combination of flow velocities measured over the years in the spring form a complete cyclonic flow field. The difference is that the spring flow field appears as an ellipse in the north-south direction which is consistent with the distribution curve shown in Figure 7. Furthermore, the center of the eddy is shifted southeastward by a half latitude unit. The spring eddy thickness is over 50 m.

IV. Conclusions

Major findings of hydrological surveys conducted in northern East China Sea have been described above. The flow of Huanghai Coastal Current into northern East China Sea has been explained. We also pointed out that a cyclonic eddy southwest of Cheju Island was present during every survey. By plotting all the historic residual current data together, the result shows a complete cyclonic eddy in that region. This cyclonic eddy motion indeed exists in the region. Consequently, we proved that the conclusion reached by Hu Dunxin [7579 2414 2946] et al[3] and Mao Hanli et al [5,6] that a semi-permanent year round cyclonic eddy exists southwest of Cheju Island is correct.

REFERENCES

[1] Lu Lianghong [0712 5328 3163], 1982, "Analysis of Flow Measurement by Anchored Buoys in Northern East China Sea," HAIYANG KEXUE [OCEANIC SCIENCE] 6: 4-8.

[2] Hu Dunxin, Ding Zongxin [0002 1350 0207] and Xiong Qingcheng [3574 1987 2052], "Preliminary Analysis on Cyclonic Eddy in Northern East China Sea," 1980; KEXUE TONGBAO [SCIENCE COMMUNICATIONS] 25 (1): 29-31

[3] Hu Dunxin, Ding Zongxin and Xiong Qingcheng, 1983, "Preliminary Analysis on Cyclonic Eddy Sea in the Summer," HAIYANG KEXUE JIKAN [SYMPOSIUM ON OCEAN SCIENCE] 21: 87-99.

[4] Xiong Qingcheng and Zhao Baoren, 1984, "Observation and Analysis of Temperature, Salinity and Current in Cold Eddy Region in Northern East China Sea in July 1980," HAIYANG KEXUE [OCEAN SCIENCE] 1: 1-6.

[5] Mao Hanli, Hu Dunxin, Zhao Baoren and Ding Zhongxin, 1983. "A Cyclonic Eddy in the Northern East China Sea." Proceedings of International Symposium on Sedimentation on the Continental Shelf with Special Reference to the East China Sea, 12-16 April 1983, Hangzhou, China. Oceam Press, pp 280-287.

[6] Mao Hanli, Hu Dunxin, Zhao Baoren and Ding Zhongxin, 1984. "Mesoscale Eddy Movement in the Northern East China Sea," CHINESE JOURNAL OF OCEAN-OLOGY AND LIMNOLOGY 1 (3): 237-247.

[7] Zhao Jinsan, Qiao Ronghen, Dong Ruzhou, Zhang Jialin and Yu Shanging, 1983. "An Analysis of the Current Condition in the Investigation Area of East China Sea." Proceedings of International Symposium on Semimentation on the Continental Shelf with Special Reference to the East China Sea, 12-16 April 1983, Hangzhou, China. China Ocean Press, pp 288-301.

PHYSICAL SCIENCES

SPECTRAL ANALYSIS OF WAVES IN GULF OF TONKIN DESCRIBED

[Article by Wang Wenzhi [3769 2429 6347], Nanhai Oceanography Institute,
Chinese Academy of Sciences, "A Preliminary Analysis of the Wave Spectrum in
the Gulf of Tonkin during the Passing of a Cold Wave"; paper received
10 October 1978]

[Text] Although lots have been accomplished in the study of sea-wave spectrum,
its spectrum form has not yet been unified. The various spectrum representa-
tions that have been proposed give the results that are quite different from
one another. Therefore, it is extremely important to analyze the observed wave
spectra of a selected area of the sea. On the one hand, it will produce know-
ledge about the composition of the wave spectrum of a certain sea zone, which
will be useful for areas such as constructions at sea, ship-building and wave
forecast. On the other, it will provide information helpful to the comprehen-
sive efforts in the theoretical study of sea-wave spectrum.

Spectrum calculations were carried out on 12 wave records from a fixed site in
the Gulf during the passing of a stormy cold wave and a preliminary analysis and
discussions of the results are presented in this article. Among the 12 calcu-
lated correlation function graphs, some are not perfect. Either they don't
oscillate along the time axis or they are far from approaching zero. These are
probably due to insufficient measuring time and the presence of the "zero-line
drifting" phenomenon, which will be discussed in this article.

1. Source of Data

The wave data used in this article were measured by a wave gauge on board a
Chinese ship at a hydrological station (109°15'E and 20°45'N) in the Gulf of
Tonkin between 23:30 of 16 January 1973 and 14:00 of 17 January 1973. For
practical reasons, each measurement lasted only about 10 minutes. At the same
time waves were measured, wind speed, wind direction, and water level were
also recorded. Wind speed was recorded by an automatic anemometer, which re-
cords the average wind speed at 2 minute intervals. Table 1 lists the wind
speed, wind direction and water level changes recorded during the passing of
this storm and Figure 1 shows the changes of wind speed and tide level.

Figure 1. Changes of wind speed and water level at a hydrological station in the Gulf of Tonkin during a storm on 17 January 1973.
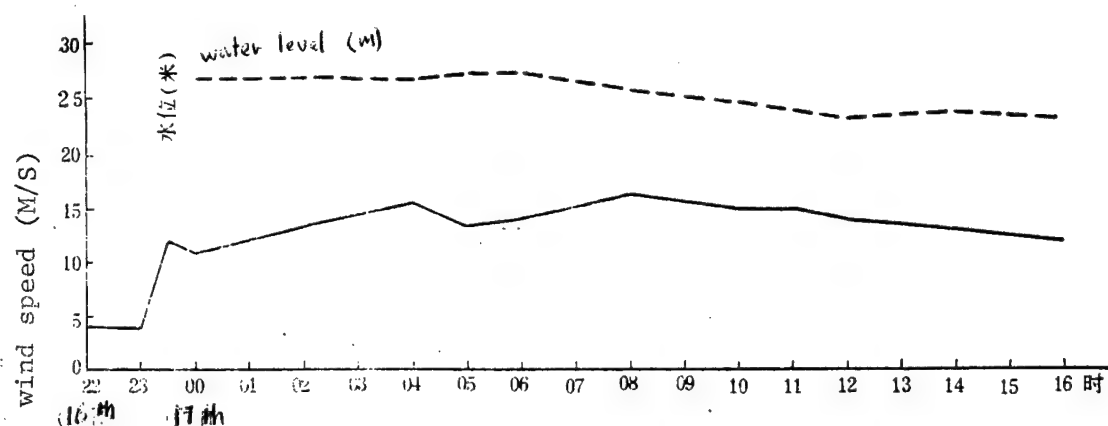
Table 1. Recorded wind and water level data

a 观测时间 （日,时:分）	b 风　速 （米/秒）	c 风　　向	d 风区长度 （公里）	风区内平均水深 e　（米）	f 实测水位 （米）
16,23:30	12.0	N	77	20	
16,23:52				20	
17,00:00	11.0	NNE	95	20	26.7
17,02:00	13.5	NNE	95	20	27.0
17,04:00	15.6	NNE	95	20	26.8
17,05:00	13.5	NE		20	27.3
17,06:00	14.0	NNE	95	20	27.3
17,08:00	16.5	NNW		20	25.8
17,09:00				20	
17,11:00	15.0	N	77	20	
17,12:00	14.0	N	77	20	23.0
17,14:00	13.0	N	77	20	23.5

Key:

a. Observation Time (day, hr:min)　d. Fetch length (Km)
b. Wind speed (m/s)　e. Average depth within the fetch (m)
c. Wind direction　f. Measured water level (m)

(Subsequently, the data will be designated by their observation times.)

2. Methods and Results of the Spectrum Calculations

We treated the sequences of wave observed as a quasi-stable process. The continuous wave records were scattered by a time interval of $\Delta t = 0.375$ s to get a series of samples from the time sequence $\{x_i = x(i\Delta t), i = 1, 2, \cdots, N\}$. The wave spectra were then calculated in four stages.

(1) Calculations of the average values

$$\bar{x} = \frac{1}{N} \sum_{i=1}^{N} x_i \qquad\qquad (1)$$

13

(2) Calculations of the correlation functions

$$C_\gamma = C(\gamma \Delta t) = \frac{K^2}{N-\gamma} \sum_{i=1}^{N-\gamma} (x_i - \bar{x})(x_{i+\gamma} - \bar{x})$$

$$\cong \frac{K^2}{N-\gamma} \sum_{i=1}^{N-\gamma} x_i x_{i+\gamma} - K^2 \bar{x}^2$$

$$\gamma = 0, 1, 2, \cdots, m \qquad\qquad (2)$$

where K is a factor for the conversion of height on chart paper into actual height.

(3) Calculations of the unrefined wave spectrum

$$V(\omega_h) = \frac{2\Delta t}{\pi} \left[C_0 + 2 \sum_{\gamma=1}^{m-1} C_\gamma \cos \frac{\pi \gamma}{m} h + C_m \cos \pi h \right]$$

in which

$$\omega_h = h\Delta\omega = \frac{\pi}{m\Delta t} h$$

$$h = 0, 1, 2, \cdots, m \qquad\qquad (3)$$

(4) Calculations of the refined wave spectrum

$$S(\omega_0) = 0.54 V(\omega_0) + 0.46 V(\omega_1)$$
$$S(\omega_h) = 0.54 V(\omega_h) + 0.23[V(\omega_{h-1}) + V(\omega_{h+1})]$$
$$h = 1, 2, \cdots, m-1$$
$$S(\omega_m) = 0.54 V(\omega_m) + 0.46 V(\omega_{m-1}) \qquad\qquad (4)$$

Actual calculations were carried out on a model DJS-21 computer. The data for each time sequence are shown in Table 2. Through the calculations, 12 correlation functions and spectra were obtained, 4 of them are shown together in Figure 2. To make it easier for comparison, we divided the 12 spectra into 2 groups: those before 170800 in one group and those after in the other. They are shown as a group in Figures 3 and 4.

In the program for wave spectrum calculations, we also included the calculations of three relevent features:

(1) Calculations of the zero-, 2nd-, and 4th-order moments of the spectrum, Mo, M2, M4, and the spectrum width coefficient $\mathcal{E}$. The equations are as follows:

$$M_0 = \frac{1}{3} \left(\frac{\pi}{m\Delta t} \right)^1 [1 \cdot S(\omega_0) + 4 \cdot S(\omega_1) + 2 \cdot S(\omega_2) + \cdots$$
$$+ 4 \cdot S(\omega_{m-1}) + 1 \cdot S(\omega_m)]$$

$$M_2 = \frac{1}{3} \left(\frac{\pi}{m\Delta t} \right)^3 [1 \cdot 0^2 \cdot S(\omega_0) + 4 \cdot 1^2 \cdot S(\omega_1)$$
$$+ 2 \cdot 2^2 \cdot S(\omega_2) + \cdots + 4 \cdot (m-1)^2 \cdot S(\omega_{m-1})$$
$$+ 1 \cdot m^2 \cdot S(\omega_m)]$$

14

$$M_4 = \frac{1}{3}\left(\frac{\pi}{m \triangle t}\right)^5 [1 \cdot 0^4 \cdot S(\omega_0) + 4 \cdot 1^4 \cdot S(\omega_1)$$
$$+ 2 \cdot 2^4 \cdot S(\omega_2) + \cdots + 4 \cdot (m-1)^4 \cdot S(\omega_{m-1})$$
$$+ 1 \cdot m^4 \cdot S(\omega_m)] \tag{5}$$

$$\varepsilon = \sqrt{1 - \frac{M_2^2}{M_0 M_4}} \tag{6}$$

The calculated values of Mo,M2,M4, and are listed in Table 3. The calculated Mo should equal to 2Co.
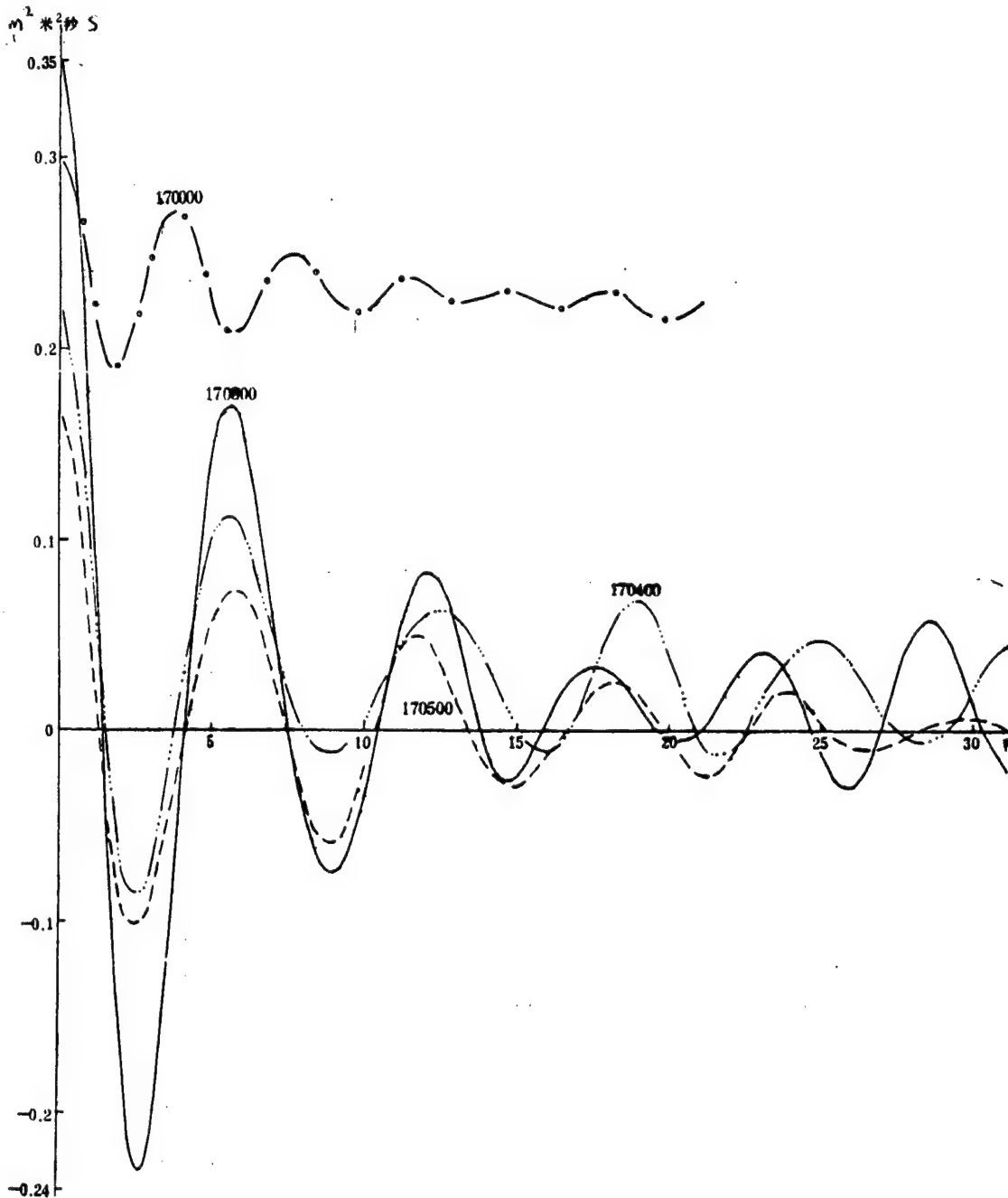
Figure 2. The correlation functions of four sets of reccrds.

15

Table 2. Related parameters in the spectral analysis of the recorded data.

编 号 No.	Δt (s) (秒)	N	T (min) (分)	# of wave 波的个数	m	df
162330	0.375	1124	7.0		42	53
162352	0.375	1440	9.0		56	51
170000	0.375	1468	9.2	145	56	51
170200	0.375	2048	12.8	153	84	48
170400	0.375	2048	12.8	154	84	48
170500	0.375	2048	12.8	150	84	48
170600	0.375	1440	9.0	100	56	51
170800	0.375	2048	12.8	154	84	48
170900	0.375	1500	9.4	109	56	53
171100	0.375	2048	12.8	147	84	48
171200	0.375	1512	9.5	110	56	54
171400	0.375	2048	12.8	151	84	48

t--time interval; N--sample capacity of a time sequence; T = N t--total duration of a time sequence; m--# of data point for correlation function and spectrum; df = 2[N/m-1/4]--degree of freedom of the calculated values. Values of 50-60 are appropriate for wave spectrum analysis.

Table 3. Calculated values of moment and spectrum width coefficient.

编 号 No.	M_0 (米²) (m²)	M_2 (m² S⁻²) (米²秒⁻²)	M_4 (m² S⁻⁴) (米²秒⁻⁴)	ε
162330	0.026	0.240	7.408	0.834
162352	0.106	0.356	4.014	0.837
170000	0.592	0.430	3.490	0.954
170200	0.278	0.578	3.852	0.829
170400	0.430	0.840	9.826	0.912
170500	0.328	0.688	4.946	0.841
170600	0.512	0.888	4.788	0.823
170800	0.702	1.240	9.964	0.883
170900	0.588	0.972	5.394	0.838
171100	0.292	0.578	4.862	0.875
171200	0.428	0.854	8.750	0.897
171400	0.360	0.870	11.006	0.900

(2) Examining the changes of the correlation functions. Given $\delta > 0$ and a positive integer δm, a number m is selected by computer such that the absolute values of the final δm correlation function values Cj do not exceed δ, that is

$$|C_j| \leqslant \delta \qquad j = m - \delta_m + 1, m - \delta_m + 2, \cdots, m$$

16

Figure 3. The Spectra of 162330-170800.
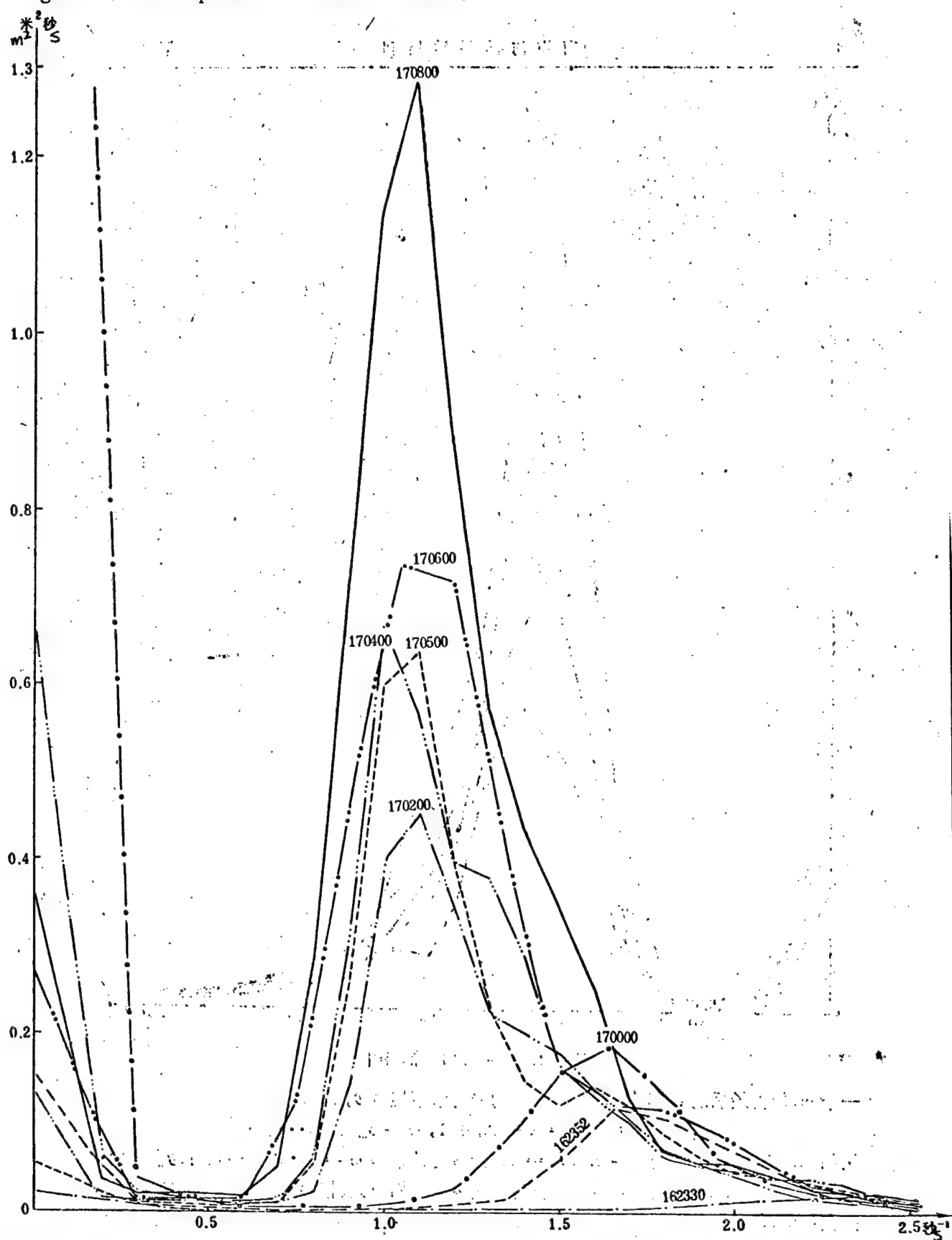
Figure 4.   The spectra of 107800-171400.
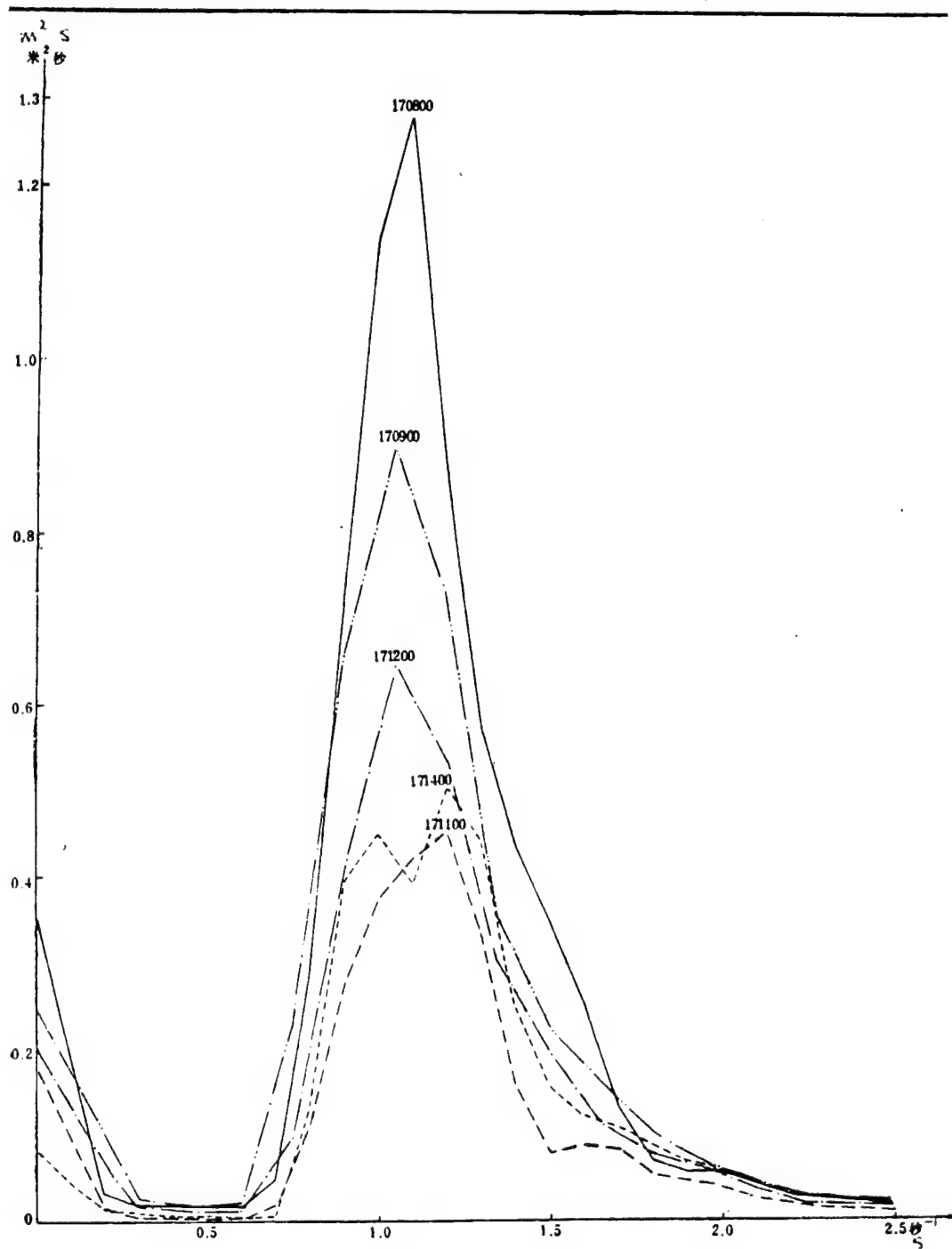
Take 170800 as an example. When $\delta = 0.1$ and $\delta m = 20$, the result is m = 38; When $\delta = 0.01$ and $\delta m = 20$, it is m > 222. It is clear that even with a very large m the oscillation amplitude of the correlation functions is not completely reaching zero.

(3) Dividing each time sequence into four sections and calculating their averages. Given the averages of the four sections, comparisons of them with the total average of the time sequence can be made. We define the maximum deviation of the section averages from the total average as

$$\bar{\Delta} = \frac{\max_{l} \{ |x_l - \bar{x}| \}}{\bar{x}} \qquad l = 1, 2, 3, 4 \qquad (7)$$

From the values of the maximum deviation we can determine whether the average values of a time sequence are constant or near constant, which would lend support to our treating the sequences of wave as a stable process. Of course, this is not the only criterium. To be a stable process, the condition that "correlation function is related only with time interval" has to be satisfied also. We did not check if this condition was met.

The $\bar{\Delta}$ values for the 12 time sequences are listed in Table 4. Except for 170000, the $\bar{\Delta}$ values of all sequences lie between 0.8-6.7 percent. The deviations are very small. This provides some ground in our treating approximately the sequences of wave as a stable process.

Table 4. Maximum deviations of section averages from the total average.

编 No. 号	$\bar{\Delta}$ (%)	编 No. 号	$\bar{\Delta}$ (%)
162330	2.1	170600	5.4
162352	5.5	170800	4.4
170000	31.7	170900	3.9
170200	4.0	171100	3.2
170400	6.7	171200	5.5
170500	0.8	171400	1.4
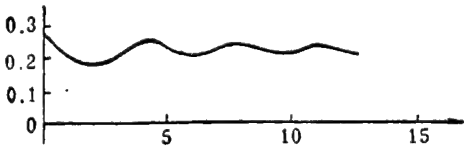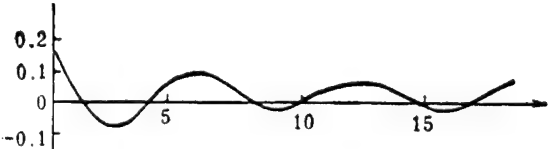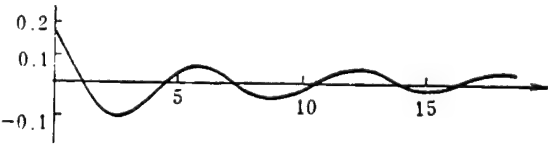
3. Analysis and Discussions of the Results

From their appearances, our graphs show only the energy distributions of the component waves within a frequency range and particularly that their peaks all fall within a narrow frequency range. It can be seen from Figure 3 that the curves become steeper as wind speed, wind duration and fetch increase and the total area under the curve also increases. Also the spectral peaks span a wider frequency range and the corresponding wave height and period of the wind-wave increase accordingly. Meanwhile, during the over 2 hours period between 162330 and 170200, the peaks shift rapidly toward low frequency end so the spectra look quite different at low frequency region but very similar at high frequency region. But the phenomenon becomes insignificant after 170200. Though the peaks still shift toward low frequency end, it happens at a far slower speed. Not only the curves are very similar, but the maxima of

19

the spectra occur at nearly the same frequency. The values of later-stage spectra are generally greater, at all frequencies, than the corresponding ones of early-stage spectra. It can be seen from Figure 4 that the peaks diminish and the areas under them decrease as wind speed and fetch decrease. But the frequency range of these peaks changes very little and the decrease of the corresponding wave height is more noticeable than that of the period.

There is a common feature in this two groups of spectral graphs, namely the spectrum values do not approach zero at the very low frequency end of these spectra (near ω = 0). This is physically impossible. To certain extent, this phenomenon can be attributed to calculation errors. And these errors have to do with the errors introduced in our determination of the zero-line of a wave profile. In other words, the time sequences are not completely centered. In the spectral analysis of these wave data, we simply used the total averages of the time sequences and that is not good enough. Due to the effect of tidal fluctuations, the effect of "zero-line drifting" in the recorded data, or other errors in calculation, the time sequences are not completely centered. The hint and extent that the 12 sets of the data analyzed are not completely centered can be seen from their $\bar{\Delta}$ values, correlation function graphs and spectra. Three key data are listed in Table 5. It reveals that the spectrum value at ω = 0 (i.e. the nondimensional quantity S(0)MoT in table 5) is not associated with wave strength but is dependent on the $\bar{\Delta}$ value and the position of the correlation function curve. To be specific, the greater the and the farther the correlation function curve is away from the time axis, the greater the spectrum value at ω = 0 and the worse it is off the center.

Table 5. The effect of off-center on the correlation function graph and spectrum.

No. 编 号	$\bar{\Delta}$ (%)	Correlation Function Graph 相 关 函 数 图 形	$\frac{S(0)}{M_0 T} \times 10^{-3}$
170000	31.7		10.3
170400	6.7		2.0
170500	0.8		0.2

When we selected the scattered data points xi from the record, we assumed the zero-line of the measured curve was a straight line and the readings were made based on a line parallel to the assumed zero-line (such as baseline I in Figure 5). When the zero-line of the measured curve drifts (line the curve in Figure 5), then it is unlikely to be completely centered. If we re-examine the circumstances under which the curves were measured and draw as closely as possible the actual zero-line (not necessarily a straight line), and then select a baseline II that is parallel to it (as shown in Figure 5) for data readings, the extent that the time sequences are centered can be greatly improved. We purposefully applied the method on 170000 and 170400, which have the largest zero-line drifting, to modify the data and carried out similar calculations. The results are shown in Figure 6 and Table 6. When compared with the graphs of 170000 and 170400 in Figures 2, 3 and Table 5, it is obvious that there is a great improvement. In the part that $\omega > 0.5$, the spectral density graphs almost completely coincide with each other. Also for the part that $\omega < 0.5$, particularly near where $\omega = 0$, the spectral density values are very close to zero. The same for the correlation fucntions. Their graphs agree totally with each other and they oscillate around the time axis and are more symmetrical. In short, they are closer to reality.

Figure 5. Schematic plot of baseline I and II.
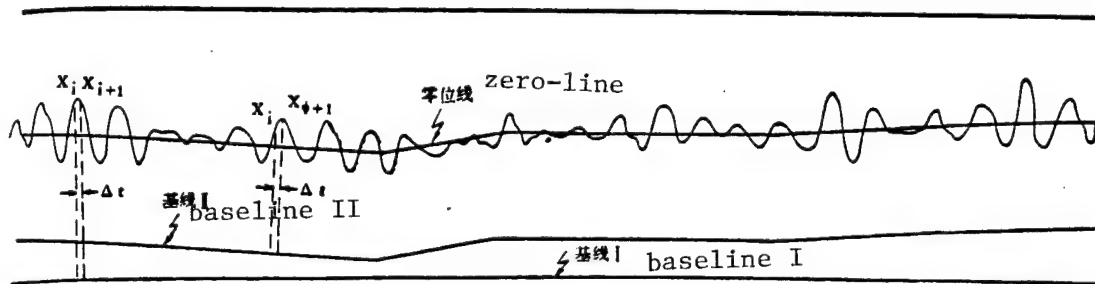
Table 6. The improvements in correlation function graphs and spectra after the degree of centering is improved.

编 号 No.	$\bar{\Delta}$ (%)	Correlation Function Graph 相 关 函 数 图 形	$\frac{S(0)}{M_0 T} \times 10^{-3}$
170000	0.6		0.3
170400	1.4		0.3

21

Figure 6-a. The calculated correlation function graphs of 170000 and 170400 using the data based on baseline II.
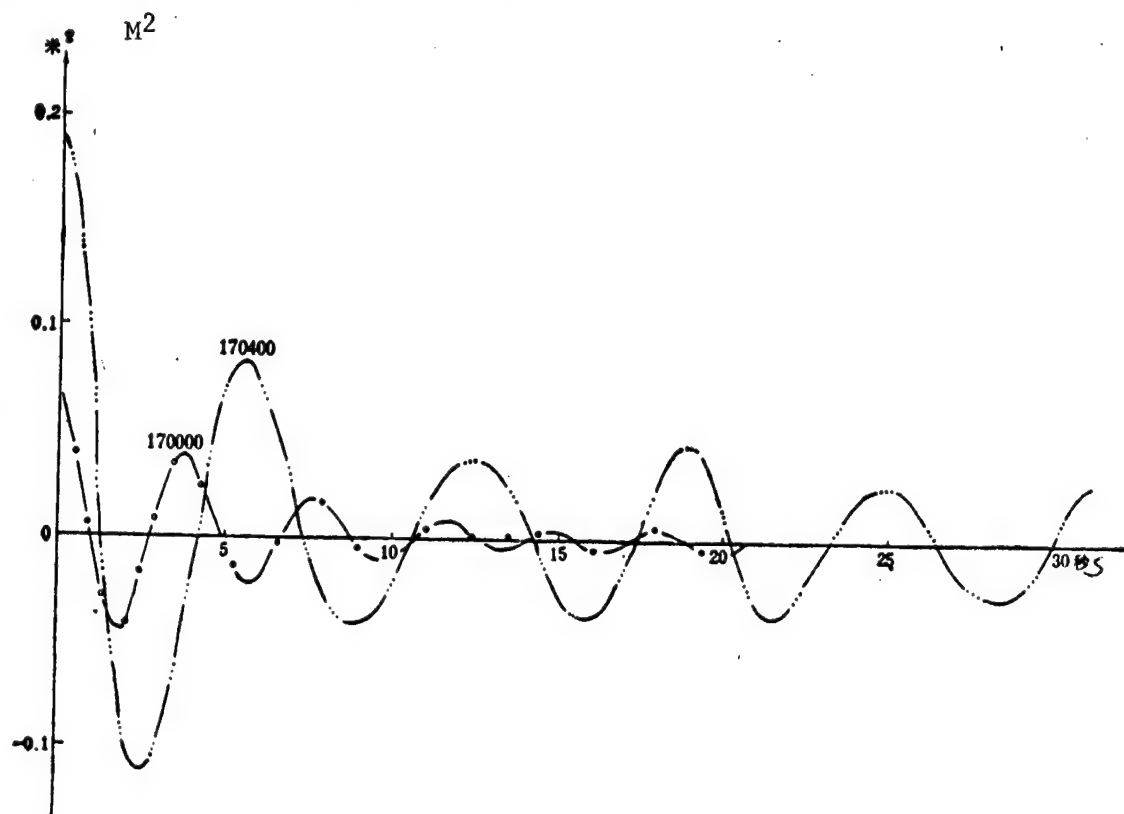
Figure 6-b. The calculated spectra of 170000 and 170400 using the data based on baseline II.
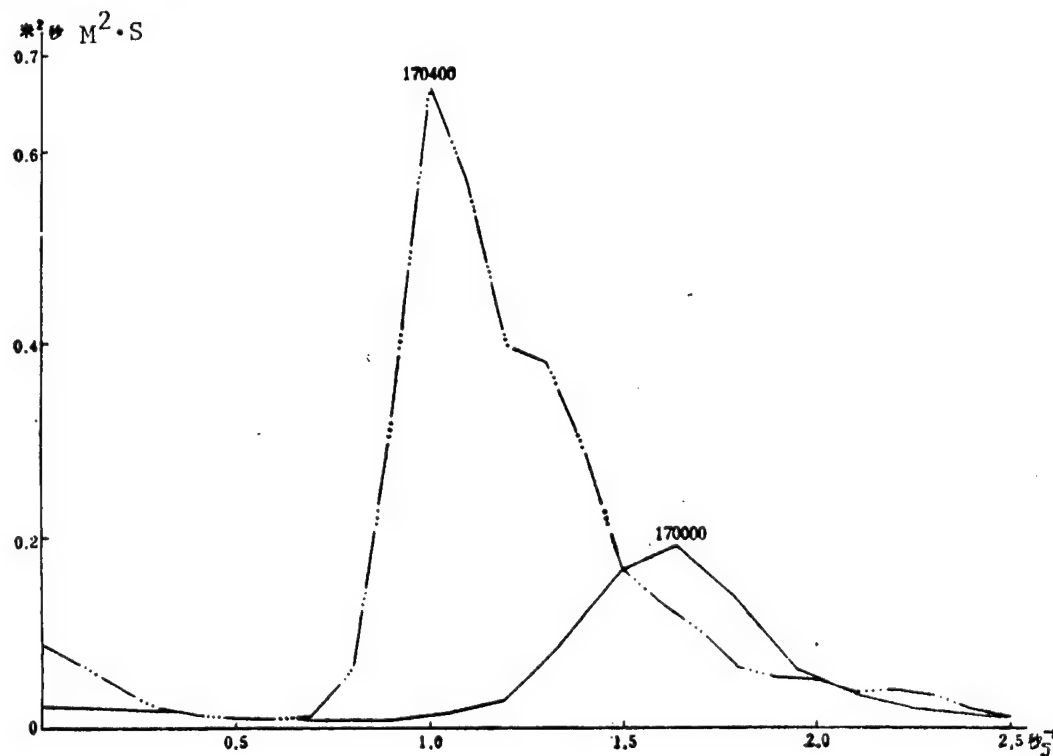
In order to accurately estimate the total area of the spectral peaks (equivalent to the total energy of the wind-wave), we extracted ΔMo, the area corresponding to the region of $0 \leqslant \omega \leqslant 0.25$ s^{-1}, from the total area Mo to get the modified total area E of the spectral peaks. The results are listed in table 7. Figure 7 depicts the changes of the total area based on the data in table 7.

Table 7. The calcualted areas of the spectral peaks.

No. 编 号	$M_0 (M^2)$ (米²)	ΔM_0 (米²)(M²)	$(M^2)E$ (米²)	编 No 号	$(M^2)M_0$ (米²)	$(M^2 \Delta M_0$ (米²)	$\frac{E}{(米²)}(M^2)$
162330	0.026	0.0042	0.022	170600	0.512	0.0398	0.472
162352	0.106	0.0224	0.084	170800	0.702	0.0040	0.698
170000	0.592	0.4734	0.119	170900	0.588	0.0398	0.548
170200	0.278	0.0146	0.263	171100	0.292	0.0202	0.272
170400	0.430	0.0738	0.356	171200	0.428	0.0308	0.397
170500	0.328	0.0080	0.320	171400	0.360	0.0102	0.350

Figure 7. Changes in spectral peak areas.
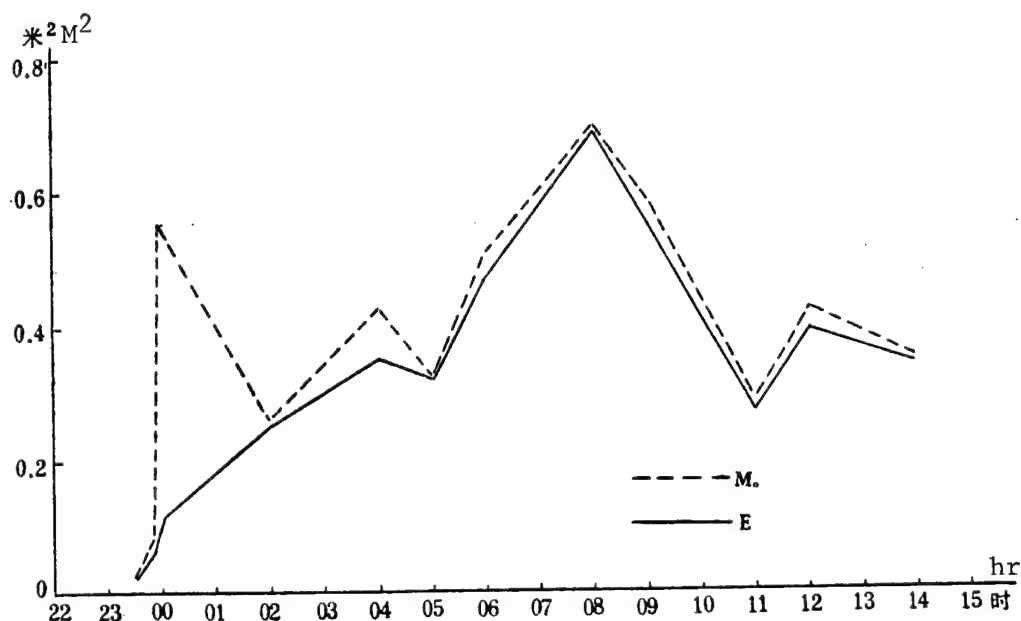
We have mentioned earlier that, as shown in Figure 3, the frequency range that covers the peak and major energy distributions of the wind-wave spectrum shifts from high toward low frequency end. But after 170200, the change becomes less obvious. The major distributions of energy are concentrated within the frequency range of [0.65, 1.75]. Table 8 lists the exact values of $[S(\omega)]$max of the individual spectrum before 170800, which reach the maximum near the frequency ωm. The frequency ranges that cover the major distributions of energy are also listed.

23

The last column in Table 3 were calculated from eq.(6). This is one way to obtain the spectrum width coefficient $\mathcal{E}$ from the internal structures of the wave. One can also get $\mathcal{E}$ from the shape of the measured curves for comparison.

Table 8. The distribution characteristics of the wind-wave energy with respect to frequency

编 a 号	$[S(\omega)]_{max}$ (米²秒) $(M^2 \cdot S)$	ω_M (秒⁻¹) (S^{-1})	主要能量集中的频率范围 b	
			频率范围(秒⁻¹) c	占总能量的百分比 d
162330	0.018	2.20	[0.8,5.8]	85
162352	0.120	1.70	[1.35,2.55]	86
170000	0.190	1.65	[1.35,2.10]	85
170200	0.468	1.05	[0.65,1.75]	85
170400	0.676	1.01	[0.65,1.75]	85
170500	0.664	1.06	[0.65,1.75]	85
170600	0.796	1.11	[0.65,1.75]	85
170800	1.300	1.07	[0.65,1.75]	85

Key:
- a. No
- b. Frequency range that covers the major distribution of energy
- c. Frequency range (s⁻¹)
- d. Percentage of the total energy

If one defines the average period of the measured curve x(t) as $T_\tau = t'/N_\tau$, and the average period of dx(t)/dt as Tc = T'/Nc where t' is the time duration of x(t), N_τ is the number of times that x(t) reaches zero within time t' and Nc is the number of peaks (the maxima of x(t) values) within the t', it can be proved that $Tc/T_\tau)^2 = M_2^2/M_0M_4$. Therefore, eq.(6) can be rewritten as

$$\varepsilon = \sqrt{1 - \left(\frac{T_c}{T_\tau}\right)^2}$$

or

$$\varepsilon = \sqrt{1 - \left(\frac{N_\tau}{N_e}\right)^2} \tag{8}$$

The $\mathcal{E}$ values listed in table 9 were calculated from eq.(8).

It is known that $\mathcal{E}$ is a distinctive quantity depicting the degree the wind-wave energy is concentrated with respect to frequency and that $0 < \mathcal{E} < 1$. When $\mathcal{E}$ is closer to 0, the frequency range in which the spectrum densities converge becomes narrower. In the literature [3], those with $\mathcal{E} < 0.4$ were referred to as narrow sepctrum and those with $\mathcal{E} > 0.4$ wide spectrum. As evident from Tables 3 and 9, our calculations show that the results from eqs.(6) and (8) are quite different, although these equations are theoretically identical. Generally, the calculations of moment involved in eq.(6) are inaccurate, particularly for higher order moments M2 and M4. Therefore, the calculation results of eq.(8) seem more reliable.

24

Table 9. The calculated values based on the shape feature of the measured curves.

No	N_τ	N_e	ε
162330	131	147	0.454
162352	147	166	0.465
170000	148	157	0.334
170200	176	204	0.506
170400	180	196	0.396
170500	191	205	0.363
170600	120	131	0.401
170800	172	193	0.454
170900	103	116	0.460
171100	155	175	0.464
171200	119	136	0.484
171400	167	190	0.477

The spectrum is a function of such wave elements as wave height and average period. For example,

$$\bar{H} = 1.77\sqrt{E}, \quad \bar{H}_{\frac{1}{3}} = 2.83\sqrt{E}$$

$$\bar{H}_{\frac{1}{10}} = 3.60\sqrt{E} \tag{9}$$

$$\bar{\tau} = 2\pi\sqrt{\frac{M_0}{M_2}} \tag{10}$$

Table 10 gives the comparison of the measured values of wave height and period with those calculated from eqs. (9) and (10), in which the "measured values" were obtained by statistical means from the measured curves. It can be seen that the measured and calculated wave heights agree well while the calculated periods are significantly lower than the observed, which is probably due to the larger errors in the second-order moment M2.

Table 10. Comparison of the calculated and observed values of wave height and period.

No	E (*²)(m²)	$\sqrt{E}$ (*)(m)	H (*)(m) H_{CAL}*	H_{OBS}	$H_{1/3}$ (*)(m) $H_{1/3 CAL}$*	$H_{1/3 OBS}$	$H_{1/10}$ (*)(m) $H_{1/10 CAL}$*	$H_{1/10 OBS}$	M_0 (*)	M_2 (*²s⁻²)	τ (s) τ_{CAL}*	τ_{OBS}
162330	0.022	0.148	0.26		0.42		0.54		0.026	0.240	2.6	
162352	0.084	0.289	0.51		0.82		1.05		0.106	0.356	3.4	
170000	0.119	0.343	0.61	0.59	0.97	0.97	1.24	1.31	0.592	0.430	7.4	3.7
170200	0.263	0.512	0.91	0.97	1.45	1.48	1.85	1.99	0.278	0.578	4.4	5.0
170400	0.356	0.595	1.06	1.08	1.69	1.65	2.15	2.15	0.430	0.840	4.5	5.0
170500	0.320	0.564	1.00	1.06	1.60	1.64	2.04	2.17	0.328	0.688	4.3	5.1
170600	0.472	0.685	1.22	1.30	1.94	2.01	2.48	2.52	0.512	0.888	4.8	5.4
170800	0.698	0.833	1.48	1.30	2.36	2.30	3.01	2.90	0.702	1.240	4.7	5.0
170900	0.548	0.739	1.31	1.30	2.10	2.06	2.67	2.60	0.588	0.972	4.9	5.2
171100	0.272	0.520	0.92	0.98	1.48	1.57	1.88	1.99	0.292	0.578	4.5	5.2
171200	0.397	0.629	1.12	1.14	1.78	1.84	2.27	2.31	0.428	0.854	4.4	5.2
171400	0.350	0.589	1.05	1.04	1.67	1.65	2.13	2.22	0.360	0.870	4.0	5.1

25

4. Conclusions

The spectral analysis of 12 sets of observed wind-wave data during the passing of a storm was carried out and certain insights about the wind-wave spectrum of the Gulf of Tonkin during the passing of a cold wave were gained. However, some of the information needs to be verified with additional observations. As to the collected wave data, we have to further improve the aspect of data treatment and further refine our analysis methods. First, zero-line drifting exists to a varying extent in the observed wave data. In our attempts to eliminate this effect, we should try various approaches and compare their results; secondly, lots of personal judgment were involved in our selections of m values in eqs.(2), (3) and (4). Different m values will give different spectra. The greater the m, the sharper the spectrum peak. So which m value will give a corresponding spectrum that matches the real spectrum? Thirdly, regarding the problem that the two spectrum width coefficients as calculated from the internal structure and external characteristics of the wind-wave are different, how can they be unified on the basis of their formulas and the physical meaning of ε'? Fourthly, the data collecting during the passing of the storm was rather thorough. We ought to investigate further the relationship of the spectrum change with wind speed, wind duration, etc. In summary, the analysis of these wave data has to be continued.

REFERENCES

[1] Wen Shengchang, "Wave Theory," Shangdong People Press, 1964.

[2] Blackman, R.B. and J.W. Tukey, 1959, "The Measurement of Power Spectrum from the Point of View of Communications Engineering," New York, Dover.

12922/12232
CSO: 4008/1052

PHYSICAL SCIENCES

PHYSICAL, MECHANICAL EFFECT OF VELOCITY OF SOUND IN OCEAN SEDIMENTS

[Article by Liang Yuanbo [2733 0337 0590] and Lu Bo [4151 0590] of the Chinese Academy of Sciences, South China Sea Institute of Oceanography, Guangzhou; paper received 12 October 1982, finalized 4 April 1983]

[Text] Abstract: The use of acoustical methods to obtain information on the physical-mechanical properties of the ocean floor sedimentary layer has been one of the fast developing ocean floor research methods[1-4] in recent years. Observations during the last 10 to 20 years using electron microscope technology have led to the discovery of a few important microscopic characteristics of sedimentation; for example, the condition of granular sediment buildup, the pore structure, and aspect ratio of pores, etc. All these have effects which cannot be overlooked when considering the propagation characteristics of sound in ocean floor sediments, particularly in terms of the velocity of sound. In order to clarify the structure of ocean floor sedimentation and the physical mechanism of the mechanical factors that influence the propagation characteristics of sound, the authors investigated the relationship between the microscopic structure of sediment and macroscopic acoustical phenomena. Also, taking one representative area of the continental shelf in the northwest section of the South China Sea as an example, regression analysis was carried out on a set of test data from 17 test sites. Letting the unidimensional compressive strength, q_u, be equivalent to a factor which comprehensively expresses the macroscopic effect of the granular buildup and pore structure of ocean floor sediment, the porosity, n, was used to calculate a supplementary revised term for the speed of sound, c, in the sediment layer. The following empirical formula was obtained:

$$f(c,n,q_u) = c - 4195 + 90.5833n - 0.7695n^2 + 94.6968q_u - 64.4603q_u^2 = 0,$$

The formula raises the calculation precision of the often used formulae (for example, the Anderson formula[5]) which do not consider pore structure; and, at the same time, it eliminates the necessity of carrying out a statistical survey of corrected sound velocity calculations on microscopic pores.

I. Theory and Present Problems

Experimental results and theoretical analysis point out that, when sound waves passing through a type of fluid such as ocean floor sediment become oversaturated in the medium contained in the pores, their propagation velocity should be influenced by the fluid portion and the solid portion of the medium. M.A. Biot, in a series of papers[6], proposed a theory for sound propagation in oversaturated pore-contained fluids. This theory was also the first to point out the second power relationship of the speed (i.e. sound velocity, c):

$$c^2 = (P + 2Q + R)/\rho, \tag{1}$$

where P, Q and R are the Biot coefficients, namely:

$$P = \frac{(n-1)^2 C_s + (n-1)C_{sp} + C_w}{C_t(C_w - C_{sp}) + C_s C_{sp}} + 4/3\mu,$$

$$Q = -n \frac{(n-1)C_s + C_{sp}}{C_t(C_w - C_{sp}) + C_s C_{sp}},$$

$$R = \frac{nC_t}{C_t(C_w - C_{sp}) + C_s C_{sp}},$$

in which, C_t is the volume compression coefficient of the total sedimentary framework; C_{sp} is the solid granular compression coefficient; C_p is the pore compression coefficient; C_w is the fluid compression coefficient; n is the porosity; and $C_t = nC_p + C_{sp}$.

Although Biot's considerations may be all-encompassing in theory, in practical application these coefficients have almost no possibilities for total measurement. Empirical results also indicate clearly that it is not necessary to measure all these coefficients. For this reason, the simple M.R. Wyllie model and the "Wyllie sound time averaging formula" for porosity in oil bearing sediment and sound velocity related calculations are generally adopted as a basis.

An example of Wyllie's sound time calculation model is shown in Figure 1. It indicates the two substances (a solid consisting granular solids and a liquid or gaseous material consisting of fluid saturated with granular particles) composing the porous media. The propagation velocity of longitudinal waves is equivalent to the velocity through the two types of media according to their volumes when totally separated. Therefore, the sound time, t = 1/c [1], in passing through the composite medium should equal the sound time of passing through the solid portion plus the sound time of passing through the fluid portion:

$$t = (t_f - t_{ma})n + t_{ma} \tag{2}$$

---

1) 1 has a unit of length, dimension: L.

28

in which, t_f is the value of the sound time in the fluid within the sediment pores and t_{ma} is the value in the solid framework of the sediment.
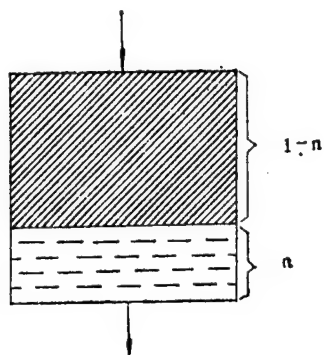
Figure 1.   Fundamentals of the Wyllie sound time averaging formula model; the slanted line portion denotes the solid medium, the remainder is the fluid medium; arrowheads indicate the direction of sound wave propagation.

From this, we obtain the relationship between the sediment porosity, n, and the sound velocity, c:

$$c = \frac{1}{n(c_{ma} - c_f) + c_f}(c_{ma} \cdot c_f),$$ (3)

where the subscripts of c are the same as in Equation (2).

These concepts have found extensive application over the last 20 years in areas of petroleum geology and acoustical well logging; moreover, they have become the theoretical basis for applied formulae for sound velocity/porosity calculations often used in sediment acoustics (for example, the Anderson formula[5] and formulae quoted in other papers[2,8]).

But, the Wyllie model and its resulting relationships also fail to take into account the natural condition of the pattern of buildup of granular sediment and the state of mechanical coupling. They especially do not consider the form of the sediment porosity and the influence of the dominant orientation of the porosity. Generally speaking, the form of the sediment porosity is a random distribution, but in view of all existing primary and secondary structures like microstrata, microcrevices, spaces between layers, or conditions of statistically dominant orientation of pores of long axis (Figure 2), there appears to be a relatively large discrepancy between the value of sound velocity as derived from the Wyllie formula and that from actual measurements. Biot's theoretical model and Equation (1) have problems similar to these. Because of this, in 1976, M. Nafi Toksoz et al. furthered the investigation into these problems. In calculations based on porous media of equivalent elasticity constant, they showed evidence of porous media of non-spherical pores with different aspect ratios. The velocity of longitudinal and transverse waves showed very great differences as compared to porous media of near spherical pores; among the differences, the effect of

longitudinal waves were greater than that of the transverse waves[9]. Because of this, they proposed the concept of a pore shape chart and also proposed the necessity of determining the aspect ratio of pores, α, to carry out corrections on sound velocity calculations. Wei Moan [7614 1075 4152] and Zhu Zhengya [2612 2973 0068][10] furthered the advances by obtaining a pore structure factor, K, on the basis of the determination and analytical calculation of actual microscopic patterns of pores. This describes, in the longitudinal wave direction, the effect of pore shape and effective pore diameter on sound velocity.
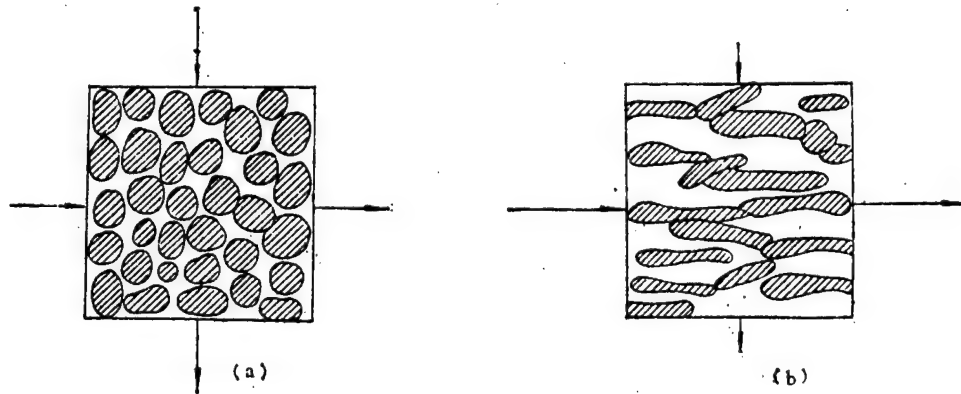
Figure 2.   Structure of granular sediment buildup and inter-granular pore orientation; arrowheads indicate the direction of sound wave propagation
(a) ideal isotropic structure of sediment and particle axes; pores have no dominant orientation; sound velocity in each direction is equivalent
(b) the long axes of the particles and the pore shapes have a definite dominant orientation; sound velocity varies in each direction

Nevertheless, regardless of Toksoz's pore shape spectrum and the aspect ratio, or the pore structure factor, K, correction applied by Wei Moan and Zhu Zhengya to the Wyllie model, each must make accurate measurements of pore size and shape, again carry out statistical operations, and definitely include the differences of the aspect ratios. This requires the use of water or oil saturation of future samples, or use of vacuum manometer methodology, even to the point of using the method of vacuum impregnation of colored organic glasses, and the microscopic examination of pore shapes, and more calculations of their horizontal and vertical contrast, α, or pore structure parameter, K. This way of doing things is not only technologically tedious, it's also difficult to obtain solutions to practical problems. Moreover, one must guess at the porosity, the aspect ratio, and the pore structure in a statistical distribution which is homogeneous, particularly in regard to the effect of a closed pore medium which does not allow a way to carry out an observation. All this limits the practical use of the theory and also limits further advances in this aspect of the research.

II. Sediment Mechanical Parameters and Velocity of Sound Data

Since 1980, at a 2100 square kilometer area of the continental shelf in the northwest section of the South China Sea (60 kilometers east-west by 35 kilometers north-south), we carried out a series of gravitational column samplings of ocean floor sedimentation, included work on an ocean floor acoustics investigation, and researched the physical-mechanical characteristics of this ocean bed material. Figure 3 shows the distribution of the column sampling points and the sound velocity measuring points within the investigated area of ocean. Analytical test results of each earth-mechanical parameter and elasticity parameter of this area of ocean floor sediment are listed in Table 1 and Table 2.
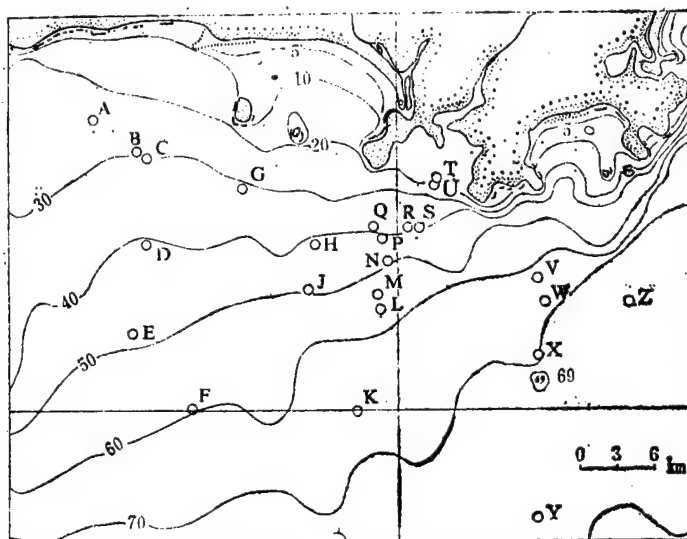
Figure 3. Distribution of test points in the experimental ocean area

The sediment mechanical parameters listed in Table 1 are all according to the People's Republic of China 1979 issue of SDS 01-79 soil mechanics regulations for carrying out testing and test conclusions; errors are all compatible with regulation requirements. The included specific gravity, G, is the specific gravity as measured by the bottle method; experimental results indicate that in the sediment in this area of ocean, the variation in specific gravity values is not large; it is near the average specific gravity of quartz and the carbonate type minerals. The determination of the unidimensional compressive strength, q_u, besides the previously discussed soil mechanics regulation for carrying out testing, is according to the Ministry of Geology and Mineral Resources, System Unit 9 Rock and Acoustics Group's methods regarding the handling of test data. Table 2 includes important parameters generally used to establish the ocean floor sediment elastic model which is usually used. Table 3 lists the sound velocity values of several of the present experimental ocean area's representative test sites as determined by reflectance methods[2]. Sound velocity data from the other test sites can be found in Table 2 of Reference [11].

---

2) In this experimental ocean area, sound velocities below the ocean floor surface were all determined from reflectance data.

Table 1. Average Mechanical Parameters in a 100 cm Layer of Sediment in the Experimental Ocean Area

Data Classification*	Porosity $n(\%)$	Porosity Ratio e	Water Content $\omega(\%)$	Wet Density $\rho_a(g/cm^3)$	Specific Gravity G	Particle Diameter ϕ	Unidimensional Compressive Strength $q_u(kg/cm^2)$	Flow Limit $W_L(\%)$	Plasticity Limit $W_p(\%)$	Plasticity Index I_p
1	55.11	1.286	46.19	1.822	2.72	5.252	0.637	33.81	19.98	14.79
2	62.4	1.660	65.81	2.440	3.08	6.780	1.480	46.90	23.00	22.30
3	42.82	0.781	19.07	1.692	2.66	3.884	0.078	24.05	14.85	9.20

* Data Classification: 1--average value, 2--maximum value, 3--minimum value

Table 2. Average Elasticity Parameters in a 100 cm Layer of Sediment in the Experimental Ocean Area

Data Classification*	Characteristic Impedance $Z(g/cm^2 \cdot s \cdot 10^5)$	Compression Coefficient β	Volumetric Modulus $\kappa(dyne/cm^2 \cdot 10^{10})$	Lame Constant λ	Poisson Ratio σ	Shear Modulus $\mu(dyne/cm^2 \cdot 10^{10})$
1	2.776	0.234	4.326	4.340	0.499	0.149
2	3.050	0.266	5.588	5.875	0.542	--
3	2.532	0.179	3.765	3.609	0.419	--

* Data Classification: 1--average value, 2--maximum value, 3--minimum value

Table 3. Some Representative Test Site Sound Velocity Data From the Experimental Ocean Area (based on Reference [11])

Test Site Designation	T		S		F		V	
Water Depth (m)	20		39.5		60		69	
Month of Observation	Oct 1980		Oct 1980		Sep 1981		Mar 1980	
Sound Velocity in Bottom Layer of Ocean Water, c_0 (m/s)	1539.7		1540.3		1538.7		1530	
Sound Velocity in Layers of Ocean Floor Sediment, c_1 (m/s) (depth is figured from the ocean floor surface)	Depth (m)	Sound speed (m/s)	Depth (m)	Sound speed (m/s)	Depth (m)	Sound speed (m/s)	Depth (m)	Sound speed (m/s)
	0	1514	0	1520	0	1530	0	1520
	1.94	~1685	9.2	~1575	2.35		1.3	1543
	98		30		3.4	1663	1.5	1551
	>98	4800	>30	1705	>3.4	1663	2.3	1569
							2.7	~1585
							36	
							>36	1701

III. Mechanical Factor, q_u, Which Influences the Velocity of Sound

R.S. Anderson[5] has extensively investigated each physical-chemical property of sediment which influences sound velocity. These include the specific gravity, G, the carbon content, C, the porosity, n, the water content, ω, the porosity ratio, e, the average particle diameter, ϕ, the particle group kurtosis, K, the skewness, SK, the weight of moisture, etc., but, except for porosity, none has given very satisfying results. Merely according to the data calculated from empirical formulae dealing with the porosity-sound velocity relationship (for example, the double parameter equations, f(c,n) = 0, of Anderson and Hamilton, etc.), still there is a relatively large difference in values with the actual sound velocity measurements due to non-linear relationships. This was already pointed out by Zhou Zhiyu [0719 1807 1946] et al. in 1983[11]. In addition, the results we obtain in the laboratory by repeatedly applying acoustical rock parameter determining instrumentation to samples, clearly show that the difference in sound velocity with the same

sample (horizontal and vertical directions) at its maximum could reach 150 to 200 meters/second; this cannot be explained using porosity alone[3]. Thus, it is clear that, besides porosity, there are still more independent parameters which influence sound velocity.

Based on previous analysis, we differed from Anderson and adopted other approaches to a solution to the problem. We took the soil mechanical parameters of sediment, including the flow limit, W_L, the plasticity limit, W_p, the plasticity index, I_p, and the unidimensional compressive strength, q_u, etc., along with the porosity parameter, n, and carried out regression analysis on the relationships to sound velocity, c, via a computer. Results clearly show that taking the sediment compressive strength, q_u, as a supplementary factor when using the porosity, n, to calculate sound velocity, compared to merely using the porosity factor, there is a better degree of correlation. For example, in comparison with Anderson's empirical formula[5] which is based on just ocean sediment sound velocity and porosity, when q_u is added as a third parameter and applied to calculation of the sound velocity in this ocean area, the standard deviation is lowered to 14.9 m/s from the 35 m/s of the Anderson formula; relative error is less than 0.95 percent. Then the three parameter regression formulas we obtain from our work in this ocean area has the following form:

$$f(c,n,q_u) = c - 4195 + 90.5833n - 0.7695n^2 + 94.6968q_u - 64.4603q_u^2 = 0. \tag{4}$$

Our calculation model is shown in Figure 4. Taking experimental ocean area test site V as an example, a comparison of calculations of sediment sound velocity using Equation (4) and other often used formulae can be inspected in Table 4.

The implications of Equation (4) are such that in practice there is the possibility for the statistical characteristics of microscopic pore structure to be reflected in the macroscopic whole, and supplementary revised results of ocean floor sediment sound velocity calculations will be obtained. q_u is just this kind of mechanical factor which can reflect microscopic pore structure as well as the nature of the granular buildup and the comprehensive effects of the state of mechanical coupling, when used as a supplementary term in calculations of the sound velocity, c.

In order to further examine the utility of Equation (4), we used it to calculate data from layers from several other positions in this ocean area.

---

3) Liang Yuanbo and Lu Bo, "Acoustical and Mechanical Properties of Shallow Ocean Floor Sediment," 1983.

Test Site V Media Parameters

Layer #	Layer thickness (cm)	Sediment type	Porosity (%)	Average particle diameter (mm)
I	34	sticky earth	57.0	0.0810
II	36	powdery sand	56.6	0.0545
III	24	sticky earth	59.3	0.0560
VI	36	sticky earth	48.6	0.0680

Ocean water

Ocean floor

Sound velocity of bottom layer of ocean water, $c_0 = 1530$ m/s

Area 1

0 (cm)

I

34

II

47

III

09

VI

130

Area 2

sedimentary sound velocity, $c_1 = 1520$ m/s

average porosity, $n = 55.4\%$

unidimensional compressive strength, $q_u = 0.078$ kg/cm^2

calculation formula: $c_c = 4195 - 90.5833n + 0.7695n^2 - 94.6968q_u + 64.4603q_u^2$

$c_1 < c_0 < c_2$

$c_2 = 1543$ m/s

Figure 4. Media Parameter Model

Table 4. Comparison of Various Calculation Results on Sedimentary Layers in the Experimental Ocean Area

Test Site	On-site Experimental Sound Velocity c_1(m/s)	Porosity n (%)	Unidimensional Compressive Strength q_u(kg/cm^2)	Formula	Calculated Results, Sound Velocity c_c(m/s)	Deviation* Δc(m/s)
				1. Anderson Formula[6]:		
				$c=2506-27.58n+0.1868n^2$	1551.4	+31.4
				2. Hamilton Formula[8]:		
				$c=2455.9-21.716n+0.126n^2$	1639.5	+119.5
V	1520	55.4	0.078	3. Formula cited in Reference [2]:		
				$c=2475.5-21.764n+0.123n^2$	1647.3	+127.3
				4. Formula (4) of this work:		
				$c=4195-90.5833n+0.7695n^2-94.6968q_u+64.4603q_u^2$	1531.3	+11.3

*$\Delta c = c_c - c_1$

Results were as follows (same units as in Table 4):

Test Site	Layer (cm)	n	q_u	c_c	c_1	Δc
F	43	59.1	0.151	1516	1530	14
L	60	62.2	0.451	1507	1520	13
U	40	62.4	0.754	1504	1514	10

Δc is within the range of the standard deviation.

IV. Some Discussion

The physical significance of Equation (4) is easy to understand because taking q_u as the upper limit of a sediment's resistance to vertical pressure, it is certainly one of the intrinsic physical-mechanical properties (or characteristics) of natural sediments; it is, due to the granular composition of the porous media, a determining factor of the pattern of granular buildup and the state of mechanical coupling. Then, speaking of relatively broad diameter particles on powdery sand, the important effective elements are the internal friction of the solid particles, and the cementing effect. As for the pattern of granular buildup, although Graton and Fraser[12] analyzed buildup in simple spherical systems and found that there are six common and important patterns, and that sediment is influenced by density and unit weight, natural sediments rarely have isometric, homogeneous, spherical buildup, leading to a situation in which there is no way to obtain a full set of factors through concrete testing (see plates 2, 3 and 4), thus, they cannot simply be accounted for using density or unit weight. Additionally, due to the cementing activity in back of the sediment (plates 5-8), one is also unable to use suspended solids equations for mineral particles in sea water to describe sedimentation (Reference [16], pp 7-11).

We have taken another look at what happens in the situation where we merely use q_u and don't consider the porosity. Gen An [2704 1489] and others have dealt with rock cores from Hokaido, Japan as well as rock experiments carried out in several of our large test areas by China's Ministry of Geology and Mineral Resources, System 9 Unit Rocks and Acoustics Group. Their results are as follows:

$$\lg(q_\bullet)=2.671\lg(c_r)+1.09$$

or,
$$q_\bullet=12.3c_r^{2.67}$$
(5)

which omits the effect of the rock porosity on sound velocity. This type of double parameter formula ($f(c,q_u) = 0$) deals with this problem from a different approach, but its results are applicable only in cases of the lowest porosity (for example, $n < 10\%$), since in this case the sound waves are basically propagating through a solid framework. Moreover, the few empirical formulae discussed above apply to test results of igneous rocks and metamorphic rock layers. But, speaking in terms of the water-saturated porous media of contemporary ocean sedimentation, the porosity, n, cannot be neglected. This point has already been amply expounded upon by Biot[6].

In common with any of the empirical formulae, Equation (4) was established from test data from specific experimental ocean areas and its coefficients in different ocean areas can have some variation. Our work, and the above analysis, just point out one way to deal with this; namely q_u is an effective factor which, together with the porosity, n, conditions the velocity of sound propagation in ocean waters. It naturally includes the macroscopic effect of the pore structure of the porous media. The results of our regression analysis of this area's sediment test data clearly show that this is the case.

37

V. Conclusion

1. Adopting the mechanical factor, q_u, comprehensively expresses the overall effects of granular buildup of ocean floor sediment and pore structure and can serve as an additional corrective factor in calculations of sedimentary layer sound velocity. It raises the calculation precision of the often used formulae which don't consider pore structure, and at the same time, it eliminates the necessity of carrying out statistical measurements of microscopic pores for correcting sound velocity calculations.

2. This work and related analyses make clear that the use of ocean floor acoustical characteristics to distinguish the engineering and mechanical properties of sedimentary layers is not only possible, but also there are broad areas which need investigation and research; for example, investigation of the relationships among the shearing strength, S, the Adebao [7093 1779 1027] liquid limit, W_L, acoustic impedance, Z, etc. As to the problem of sedimentary shear wave propagation and shear modulus, μ, we will discuss that further in a future paper. In essence, these are established through acoustical methods together with sediment mechanical properties and work dealing with relationships among geological factors. With this aspect of investigative research we can hope to more perfectly develop the technology for remote sound sensing and telemetry of ocean floor material.

PLATE CAPTIONS

Electron micrographs of ocean floor sediment structure:

1. Structure of near spherical and equal granular buildup (consisting of pyrite particles. South China Sea, northwest section continental shelf, ocean floor area #551, magnified 30,000 times.

2. Structure of granular buildup of natural sediment. Ibid., #262, magnified 5,000 times.

3. Structure of sedimentary pores having definite orientation. Ibid., #336, magnified 30,000 times.

4. Microscopic structure of plate-like bioclastic sediment. Ibid., #328, magnified 7,500 times.

5. Cementation of sediment particles (cementing of aragonite needles). Ibid., #686, magnified 8,000 times.

6. Microscopic structure of aragonite needle cementite. Ibid., #683, magnified 7,500 times.

7. Skeletal structure of network shape formed by aragonite needle cementite. Ibid., #352, magnified 30,000 times.

8. Filling and proliferating conditions of aragonite needle cementite among granular pores. Ibid., #361, magnified 15,000 times.

REFERENCES

[1] Meng Jinsheng [1322 6855 3932], Guan Dinghua [7070 1353 5478], SHENGXUE XUEBAO [ACTA ACUSTICA] (English Language Edition), 1(1980),1.

[2] Wang Dezhao [3076 1795 2507], Shang Erchang [1424 1422 2490], "Hydroacoustics," Science Press, 1981.

[3] Liang Yuanbo, Lu Bo, HAIYANG DIZHI YANJIU [OCEAN GEOLOGICAL RESEARCH], 1(1981),2.

[4] Liang Yuanbo, Lu Bo, RADAI HAIYANG [TROPICAL OCEANS], 2(1983),3.

[5] Anderson, R.S., In: "Physics of Sound in Marine Sediments," Plenum Press, 1974, 481-518.

[6] Biot, M.A., JASA, 28(1956),2.

[7] Wyllie, M.R.J., GEOPHYSICS, 21(1956),1.

[8] Hamilton, E.L., In: "Physical and Engineering Properties of Deep-Sea Sediments," Plenum Press, 1974, 1-43.

[9] Toksoz, M.N. et al., GEOPHYSICS, 41(1976): 621-645.

[10] Zhu Zhengya [2612 2973 0068], SHENGXUE JISHU [ACOUSTICS TECHNOLOGY], 1(1982),1.

[11] Zhou Zhiyu, HAIYANG XUEBAO [ACTA OCEANOLOGICA SINICA], 5(1983),5.

[12] Graton, L.C. and H.J. Fraser, JOUR. GEOL., 43(1935): 785-909.

[13] Smith, D.T., In: "Physics of Sound in Marine Sediments," Plenum Press, 1974, 41-61.

[14] Matviyenko, V.N. and Yu.F. Tarasyuk, "Dalnost' Deystviya Gidroakusticheskikh sredstv," Sudostroyeniye Publishing House, 1976.

[15] Shirley, D.J. et al., "Sediment Acoustics," AD-A084738, 1980.

[16] Kuperman, W.A. and F.B. Jensen (ed.), "Bottom-Interacting Ocean Acoustics," Plenum Press, 1980.

[17] Sun Chengdong [1327 2052 2767], "Rock Acoustics Testing," Geological Publishing House, 1981.

13226/6091
CSO: 4008/1057

PHYSICAL SCIENCES

COMPARISON OF DEEPWATER WIND-WAVE PREDICTION MODELS

[Article by Wang Bingxiang [3076 3521 4382], Zhang Jiuzi [1728 1432 5417], Department of Physical Oceanology and Marine Meteorology, and Wu Guiqiu [2976 2710 4428], First Institute of Oceanography, National Bureau of Oceanography: "Comparison of Deepwater Wind-Wave Prediction Models"; paper received 5 May 1984]

[Text] English Abstract: Presently, there are about 36 models used in deep-water wind-wave forecasting by incomplete statistics. To select from among these models 12 that are more important and currently employed are confirmed by field observations, and are compared with each other. The calculations based on the 12 have been compared with wave data proffered by Iu.M. Krylov (1958) and Bao Qiangsheng et al. (1983); so far as the cases examined are concerned, the accuracy of the results given by Wang's model are superior to those of the other 11 models. In order to investigate typhoon waves at station "Xiaomaidao" at 1800 hours 30 August 1939, the above approaches to wave prediction are used to hindcast again; the wave height on a basis of Wang's model is found to be more consistent with a 50-year return period wave at the wave station than those found for the existing models. According to the prediction technique of hurricane waves the wave height and period of the most probable first highest wave within the area of the typhoon are estimated at about 39 meters and 24 seconds respectively.

Ocean wave wave height and period are two important parameters in marine engineering site selection and structure design. There are generally two applications of these two wave factors obtained for a designated region: One is if there are already wave observation materials, then spectrum or non-spectrum methods can be relied on; the other is if there are no materials, then with the help of wave materials for neighboring marine regions, they can be deduced using refraction-diffraction theory or, after determining the wind factors from historical weather maps, they can be hindcast using wave forecast methods. We followed the second method in the second category to estimate the marine typhoon wave factors.

41

Since Sverdrup and Munk first published their method for forecasting effective wave in 1974[1], many methods have been proposed. Counting only those in references 2-10 there are 36. Although there are so many forecasting models, they can be reduced to two categories: quasi-experimental and purely experimental. We selected 12 of the more important ones which are frequently used, for verification and comparison and carried out a wind-wave hindcast based on a strong typhoon in the history of the Huanghai.

For the verification which was carried out on each method using the materials published in Table 2 of reference 6 and Table 1 of reference 11, the method of reference 4 provided better results than the other methods.

The methods were applied to hindcasting typhoon waves at Xiaomaidao at 1800 hours on 30 August 1939; based on the results of the method in reference 4, conformity to the observation values was better than the other methods. As concerns the results obtained using the hurricane wave forecast methods, the maximum probable values of the wave height and wave period within the typhoon area are 39.3 meters and 24.19 seconds, respectively.

I. Verification and Comparison of Models

1. The models were verified on the basis of the data provided in Table 2 of reference 6 and Table 1 of reference 11.

Apart from the eight models in references 3, 4, and 6, 4 of the 12 models used were newly selected for uniform units, and after conversion were

(1) G.B. Rzheplinskii (1972)[12]:

$$\left. \begin{array}{l} (H_{5\%})_x = 1.7872 \times 10^{-3} \cdot U^{4/3} \cdot x^{1/3} \\ T_x = 0.1126 \cdot U^{3/5} \cdot x^{1/5} \end{array} \right\} \tag{1}$$

$$\left. \begin{array}{l} (H_{5\%})_t = 6.6911 \times 10^{-4} \cdot U^{19/12} \cdot t^{5/2} \\ \overline{T_t} = 6.1437 \times 10^{-2} \cdot U^{3/4} \cdot t^{1/4} \end{array} \right\} \tag{2}$$

(2) B.W.Wilson, IV (1965)[10]:

$$\left. \begin{array}{l} (H_{5\%})_x = 3.7277 \times 10^{-2} \cdot U^2 \cdot [1 - (1 + 1.2528 \times 10^{-2} \cdot U^{-1} \cdot x^{1/2})^{-2}] \\ T_x = 0.7590 \cdot U \cdot [1 - (1 + 1.7126 \times 10^{-2} \cdot U^{-2/3} \cdot x^{1/3})^{-5}] \end{array} \right\} \tag{3}$$

42

(3) D.J.T.Carter(1982)[14]:

$$(H_{5\%})_x = 6.2821 \times 10^{-4} \cdot U \cdot x^{1/2}$$
$$\overline{T}_x = 5.5267 \times 10^{-2} \cdot U^{0.4} \cdot x^{0.3} \quad\} \quad (4)$$

$$(H_{5\%})_x = 3.0225 \times 10^{-2} \cdot U^2$$
$$\overline{T}_x = 0.566 \cdot U \quad\} \quad (5)$$

$$(H_{5\%})_t = 5.1292 \times 10^{-5} \cdot U^{9/7} \cdot t^{5/7}$$
$$\overline{T}_t = 1.2534 \times 10^{-2} \cdot U^{4/7} \cdot t^{3/7} \quad\} \quad (6)$$

$$(H_{5\%})_t = 2.9250 \times 10^{-2} \cdot U^2$$
$$\overline{T}_t = 0.566 \cdot U \quad\} \quad (7)$$

in which

① $t > 33.3713 \cdot U^{-0.4} \cdot x^{0.7}$

② $x < 2.32 \times 10^3 \cdot U^2$

③ $t < 7.2306 \times 10^3 \cdot U$

(4) The method in reference 2 (abbreviated QQQ) (1980):

$$(H_{5\%})_x = 3.4786 \times 10^{-2} \cdot U^2 \cdot [1 - \exp(-2.5057 \times 10^{-2} \cdot U^{-1} \cdot x^{1/2})]$$
$$\overline{T}_x = 3.645 \sqrt{H_{5\%}} \quad\} \quad (8)$$

The units U (wind velocity), x (wind area), and t (wind time) in equations (1)-(8) are, respectively, m/sec^{-1}, meters, and seconds; the $H_{5\%}$ (accumulation rate is 5 percent of wave height) and $\overline{T}$ (average period) units are meters and seconds, respectively.

The wave data in Table 1 of reference 11 was used in references 3, 4, 6, and 13; the wind factors given in this table were substituted in the relevant forms in equations (1)-(8). The results of the wave factors calculated are given in Table 1.

From the figures in Tables 2 and 3 we know that the wave height given by the method in reference 4 is better than the other methods.

Here we should explain that conversion between the wave heights was induced according to theoretical results[15], i.e.,

$$H_{5\%} = 1.95\overline{H}$$
$$H_{\frac{1}{10}} = 2.032\overline{H} \quad\} \quad (9)$$
$$H_{1/3} = 1.598\overline{H}$$

43

Table 1. Comparison of Methods

No	1.深度（米）	2.风速（米/秒）	3.风时（小时）	4.风区（公里）	5. 波高（H5%）米					6. 周期.秒				
					P	C	WIL	QQQ	7.观测	$P(\overline{T})$	$C(\overline{T})$	WIL—(T)	QQQ_(T)	7.观测(T5%)
1	146	6	18	200	1.13	1.05	0.98	1.05	0.7	3.78	3.39	3.34	3.75	3.7
2	76	7	10	250	1.15	1.12	1.31	1.40	1.0	3.64	3.41	3.85	4.34	3.6
3	193	7	17	400	1.43	1.43	1.42	1.52	1.2	4.15	3.96	4.10	4.50	4.7
4	180	8—9	4	40	1.06	0.75	1.08	1.11	1.0	3.38	2.57	3.10	3.85	3.6
5	180	8—9	12	40	1.06	1.06	1.08	1.11	1.0	3.38	3.12	3.10	3.85	3.6
6	43	8—9	18	200	1.81	2.11	1.71	1.83	1.5	4.67	4.81	4.25	4.94	—
7	—	8—9	3	400	0.94	0.61	1.97	2.11	0.9	3.11	2.27	4.73	5.31	—
8	—	8—9	9	400	1.50	1.33	1.97	2.11	1.4	4.10	3.64	4.73	5.31	4.0
9	—	8—9	16	400	1.90	2.01	1.97	2.11	1.8	4.73	4.67	4.73	5.31	4.2
10	450	8—9	22	400	2.17	2.11	1.97	2.11	1.8	5.13	4.81	4.73	5.31	4.2
11	30	9	11	120	1.65	1.66	1.64	1.74	1.4	4.36	4.10	4.03	4.81	4.0
12	30	9	18	120	1.65	1.95	1.64	1.74	1.5	4.36	4.44	4.03	4.81	4.6
13	86	9—10	4	70	1.27	0.86	1.51	1.56	1.3	3.64	2.74	3.73	4.57	3.2
14	86	9—10	5	70	1.40	1.02	1.51	1.56	1.3	3.85	3.02	3.73	4.57	3.2
15	86	9—10	9	160	1.79	1.54	1.92	2.03	1.8	4.46	3.88	4.39	5.21	4.5
16	86	9—10	11	160	1.94	1.78	1.92	2.03	1.8	4.68	4.23	4.39	5.21	4.5
17	220	10—11	12	170	2.27	2.15	2.26	2.40	2.0	5.13	4.65	4.73	5.64	5.1
18	43	11	26	200	2.55	3.09	2.53	2.67	2.0	5.45	5.61	5.02	5.97	—
19	61	11—12	14	400	2.91	2.70	3.20	3.44	2.9	5.74	5.24	5.84	6.76	6.0
20	61	11—12	18	—	3.23	3.24	—	—	2.9	6.10	5.84	—	—	6.0
21	60	12	3	30	1.52	0.95	1.51	1.50	1.1	3.93	2.77	3.49	4.49	3.7
22	60	12	7	30	1.52	1.30	1.51	1.50	1.1	3.93	3.29	3.49	4.49	3.7
23	220	12	18	150	2.60	2.91	2.64	2.77	2.0	5.42	5.33	5.01	6.07	—
24	240	12	26	600	4.03	4.21	3.72	4.00	3.4	6.92	6.79	6.41	7.30	8.0
25	85	12	2.5	180	1.51	0.83	2.78	2.92	1.2	3.85	2.56	5.20	6.25	3.7
26	85	12	5	180	2.02	1.37	2.78	2.92	1.8	4.58	3.45	5.20	6.25	4.3
27	85	13	7	180	2.64	1.93	3.12	3.28	2.2	5.29	4.17	5.45	6.60	5.3
28	85	13	8	180	2.80	2.12	3.12	3.28	2.2	5.47	4.42	5.45	6.60	5.3
29	85	14	10	180	3.40	2.74	3.46	2.63	2.5	6.16	5.07	5.70	6.94	5.6
30	85	15	12	180	3.73	3.41	3.81	3.96	3.1	6.43	5.71	5.94	7.26	6.0
31	85	15	13	180	3.73	3.61	3.81	3.96	3.3	6.43	5.91	5.94	7.26	6.4
32	60	13	22	400	4.02	4.37	3.86	4.13	3.9	6.92	6.82	6.33	7.41	6.4
33	38	14	11	170	3.34	2.93	3.40	3.55	2.5	6.09	5.29	5.63	6.87	—
34	85	14	11	180	3.40	2.93	3.46	3.63	2.5	6.16	5.29	5.70	6.94	5.6
35	2415	14	14	600	3.97	3.48	4.75	5.11	4.0	6.66	5.86	7.12	8.24	—
36	3780	14	20	1000	4.61	4.49	5.27	5.67	3.7	7.28	6.83	7.70	8.68	6.5
37	340	15	13	300	4.30	3.61	4.43	4.68	4.1	6.88	5.91	6.58	7.89	7.0
38	340	15	16	300	4.42	4.19	4.43	2.68	4.1	7.12	6.46	6.58	7.89	—
39	67	15	18	400	4.87	5.96	4.80	5.11	4.5	7.54	7.82	6.97	8.24	7.0
40	—	15	4	300	2.63	1.55	4.43	4.68	1.9	5.12	3.56	6.58	7.89	4.8
41	96	16	20	30	2.23	1.74	2.14	2.11	1.4	4.67	3.69	4.02	5.30	—
42	38	16	14	170	3.99	4.14	4.08	4.23	3.5	6.60	6.33	6.09	7.50	—
43	6370	20	20	300	6.49	6.88	6.64	6.90	5.5	8.46	8.05	7.81	9.58	—
44	3350	21	25	900	9.62	8.88	9.7_3	10.39	9.0	10.43	9.48	9.97	11.75	—

[Key on following page]

Key:
1. Depth (meters)
2. Wind velocity (m/s)
3. Wind-time (hours)
4. Wind area (km)
5. Wave height ($H_{5\%}$) meters
6. Period, seconds
7. Observations

Note to Table 1: The letters SM, B_1, K, PNJ, WEN, WANG, B_2, NOR, P, C, WIL and QQQ in Tables 1, 2, and 3 represent the methods of Sverdrup-Munk (1947), Bretschneider (1952), Krylov (1958), Pierson-Neumann-Japnes (1955), Wen Shengchang (1960), Wang Bingxiang (1964), Bretschneider (1970), norm (1978), Rzheplinskii (1972), Carter (1982), Wilson (1965), and the Shandong College of Oceanography-First Institute of Oceanography-Institute of Oceanography of the Academy of Sciences (1980), respectively. When these letters appear later in this paper, they carry the same meaning.

Table 2. Maximum Error of Wave Height Calculated According to Table 1*

(1) 方　　法	(2) 波高的最大误差	
	%	NO
SM	108.6	41
B_1	82.9	41
K	78.6	41
PNJ	75.0	18
WEN	41.1	7
WANG	35.0	41
B_2	61.0	22
NOR	51.0	40
P	61.4	1
C	50.0	1
WIL	133.2	40
QQQ	146.3	40

*SM, B_1, K, PNJ, WEN, WANG and B_2,
NOR are taken from references 4 and 6.

Key:
1. Method
2. Maximum wave height error

45

Table 3. Maximum Error of Wave Height of the Various Methods Calculated in
Table 2 According to Reference 6*

(1) 方 法	(2) 波高的最大误差	
	%	NO
SM	100.0	12
B₁	98.0	6
K	52.0	7
PNJ	105.0	2
WEN	46.0	3
WANG	32.0	5
B₂	55.0	2
NOR	51.0	12
P	61.8	2
C	42.3	2
WIL	81.7	1
QQQ	93.2	2

*Cited according to reference 6
except for P, C, WIL, and QQQ.

Key:
1. Method
2. Maximum wave height error

The relationship between periods is according to experimental equation[16]

$$T_{\frac{1}{3}} = 1.156 \, \overline{T} \tag{10}$$

This value is almost equivalent to the 1.15 of reference 17.

2. It was difficult to carry out a systematic comparison of the models.
The main difficulty was that of the 12 methods to be compared in the paper,
if we relied on the wind-wave dimensions for their growth stage we were
restricted to three essential divisions of wind, the three were: 1, simul-
taneously relative wind area and wind time growth[4]; 2, only relative to wind
area growth[2,10]; 3, growth relative to either the wind area or wind time.
To overcome this difficulty and get on with the comparison, first of all,
we handled it as reference 3 in comparing this item, and selected only one
representative wind velocity, for example, 15 m/sec⁻¹; next, since there
were two in the paper which were only relative to wind area growth, and
therefore for wave theory of growth relative to their wind area or wind
time, we took only the expression for the former; for processing reference 4,
two wind times were provided: one was the wind time (3.42 x 10⁵ sec)
necessary for the wind wave to achieve full growth at the corresponding
wave velocity of 15 m/sec⁻¹, and the other was 10² sec, which was changed
into only relative to wind area growth.

In Figures 1 and 2, the series marked WEN, SM, B$_1$, K, and PNJ reproduce Figures 7.7-3 in reference 15, the rest are calculated and drawn using various methods.
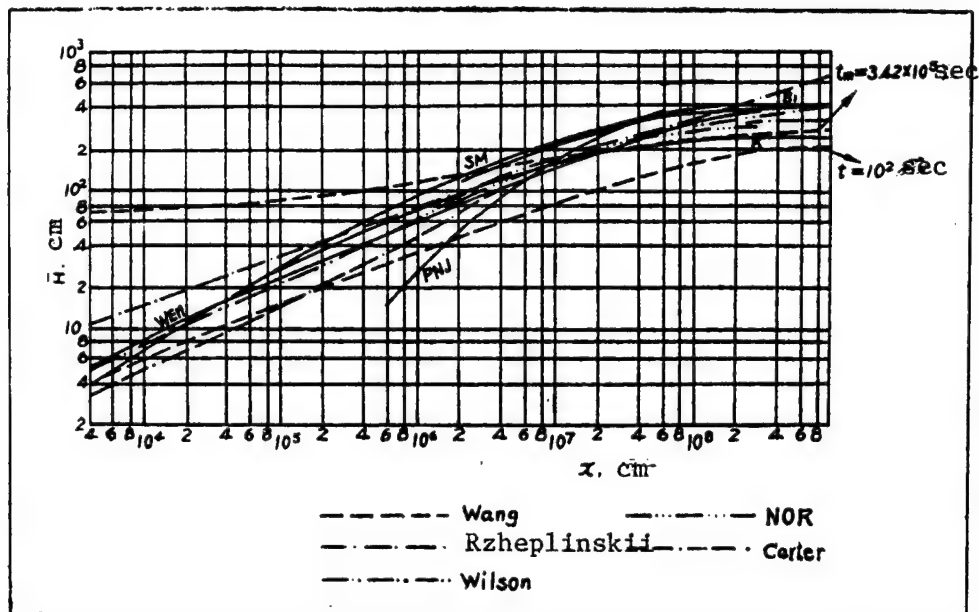
Figure 1. Comparison of Wave Height of Various Methods With Growth of Wind Area
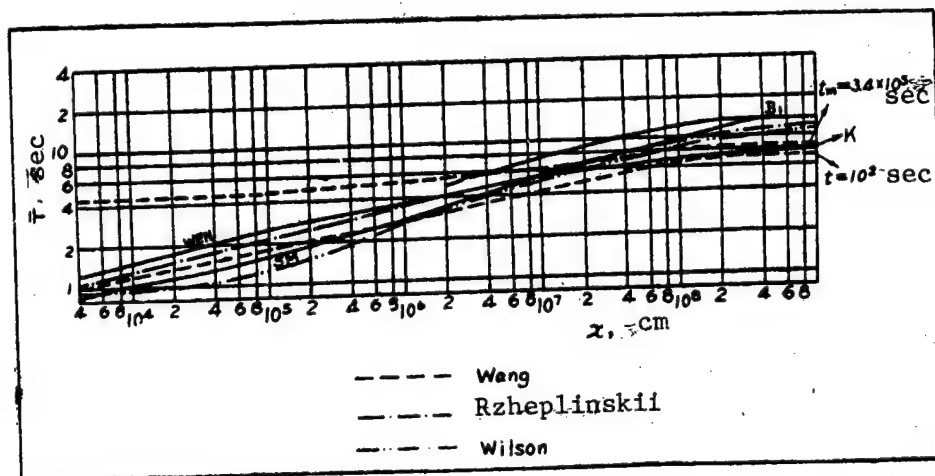

Figure 2. Comparison of Wave Period of the Various Methods With Growth of Wind Area

From the curve in Figure 1 the following characteristics can be seen: 1) The K curve from beginning to end is within the upper and lower limits of the Wang curve; 2) the Carter and PNJ curves are both below the lower limits of the Wang curve when the wind region length is smaller than 10^5 cm and

47

2×10^6 cm, respectively; 3) the SM curve first goes 30 km beyond the upper limit of the Wang curve, and continues to go beyond it, next are the B_1, Wilson, Rzheplinskii, NOR, B_2, Carter, and PNJ curves, and finally 300 km beyond it is the WEN curve.

Because the lines in the figure are so concentrated, there isn't any way to draw the B_2 curve, therefore it is explained below: 1) within the 3-200 km range, B_2 is slightly higher than WEN and slightly lower than K; 2) from 500 km it almost overlaps WEN and is higher than K; 3) in between 3 and 2000 km, is lower than B_1.

The curves in Figure 2 reveal: 1) B_1 initially goes beyond the upper limit of the Wang curve, those which continue to go beyond it next are NOR, SM, Rzheplinskii and Wilson; 2) in the wind region under discussion, WEN and K throughout are located between the upper and lower limits of the Wang curve; 3) SM and Wilson are below the lower limit of the Wang curve when the wind area is smaller than 6 km and 10 km respectively.

Three interesting relationships must be explained here: 1) At $4 \times 10^3 < X < 10^4$ cm, the Carter and Wilson period curves are both almost congruent; at $2 \times 10^4 < X < 10^7$ cm, the former is lower than the latter; at $10^7 < X < 10^8$ cm, it is the reverse; when $X > 10^8$ cm, the former is again lower than the latter. 2) At $X < 440$ km, NOR is higher than SM and Rzheplinskii; at $X > 400$ km, it is the opposite. 3) At $3 < X < 60$ km, $B_2 > SM$; at $X > 60$ km, $K < B_2 < SM$; B_2 is always lower than B_1.

From Figure 1 and Figure 2 it can be clearly seen that wind area and wind time have an influence on the wave height and period computed on the basis of the method in reference 4; when the wind area is short, wind-wave dimensions increase very rapidly with the wind time, and when it is long, the role played by the wind time gradually diminishes until $X = 3240$ km, the wind time effect becomes so weak that even the wind height and period at $t_m = 95$ hours and $t = 10^2$ seconds, are respectively 2.68 m and 2.00 m and 8.22 seconds and 7.10 seconds.

II. Hindcast of Huang Hai Typhoon Waves

In summer and autumn China's Huang Hai is occasionally hit by typhoons giving rise to typhoon waves, which have a catastrophic impact on China's coast[18].

A survey of historical materials on typhoons reveals that in the 84 years of this century the one whose impact on the southern coast of Shandong was most severe was the typhoon that went through the Huang Hai on 28-31 August 1939. It goes without saying that the dimensions of the typhoon waves which accompanied it also should be the largest. So, how high and how long were its wave height and period? On the one hand, this paper used the 12 models verified and compared in the previous section to hindcast the typhoon waves at Xiaomaidao at 1800 hours on 30 August 1939, and on the other hand relying on wave factors provided by the hurricane wave forecast methods[19] for the first largest wave likely within the typhoon area, we attempted to give a probable answer to this question.

The present problem is how to determine the wind area, wind velocity, and wind time required by wind-wave forecasts.

Since the wind velocity materials of the surface temperature map of 1800 hours on 30 August 1939 given in Figure 3 is far from able to satisfy the demands of wind-wave forecasting, we followed the read-outs of the wind velocity curve of the Qingdao meteorological station and after calculation treated the values obtained as the wind velocity required.
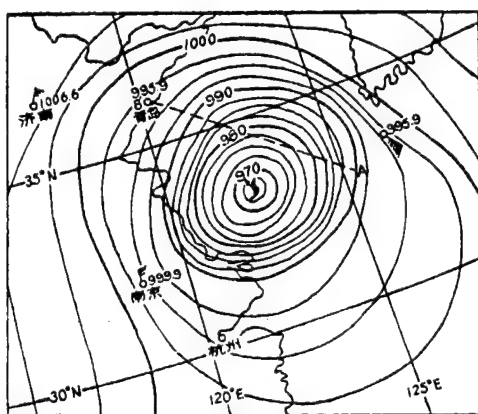

Figure 3.   Weather Map of 1800 Hours
            (Beijing time) 30 August
            1939
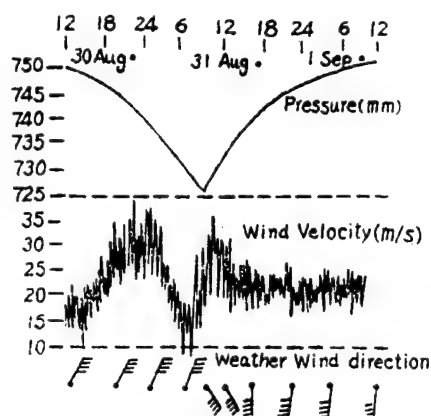
Figure 4.   Chart of Meteorological
            Changes at Qingdao
            30 August–1 September
            1939 (cited from Figure 3
            in reference 18)

From the curve in Figure 4 we read the average wind velocity at 1200 hours and 1800 hours on the 30th as $U_1 = 17.5$ m/sec^{-1} and $U_2 = 27$ m/sec^{-1}, then using the formula for when the wind velocity continues to increase we solved for the representative value between 1200 and 1800[20]:

$$U(Z_1)_1 = 0.2U_1 + 0.8U_2 = 25.1 \text{ m/sec}^{-1} \tag{11}$$

which is 0.6 m/sec^{-1} greater than the lower limit for a force 10 wind (24.5 m/sec^{-1}). Experience tells us that the wind velocity over the sea is greater by one or two grades than over the land. Thus, we took its upper limit, i.e., 2 grades, because from Figure 3 the wind area under consideration was situated on the right side of the typhoon's direction of advance, which was the area where the wind velocity was greater than its left side[19]. Therefore, the wind at sea corresponding to the Qingdao Guanxiangshang wind velocity meter, a point 103.8 meters above sea level (Z_1) the wind was the lower limit (32.7 m/sec^{-1}) of force 12 plus 0.6 m/sec^{-1}, i.e., $U(Z_1) = 33.3$ m/sec^{-1}.

According to the vertical distribution of wind velocity, we found the wind velocity at a point (Z_2) 10 meters above the surface of the sea[18]:

$$U(Z_2) = U(Z_1) \cdot \left[\frac{\log Z_2 - \log Z_0}{\log Z_1 - \log Z_0}\right] = 26.54 \quad m/sec^{-1} \qquad (12)$$

in which $Z_0 = 0.001$ is the Ellison's observation value at the sea surface.

The wind area relies on the idea of the most favorable line wind area[17], and is determined by reference to the wave propagation direction, i.e., in Figure 3, AB = 350 nautical miles.

Determination of the wind time will involve equivalent wind time t_e, for the same wave height and wave velocity, different methods will give individual values, and thus are related to the wind-wave dimensions sought. For purposes of simplification, this paper takes the norm as the standard. Assuming that at 1200 hours on 30 August the typhoon had not yet reached the area under discussion but already had waves with wave height of 5 m[18]. This value together with wind velocity $U(Z_2)$ can be found from the norm $t_e = 2.2$ hours, thus we obtain the forecast of 30 August's wind-wave wave time as 8.2 hours.

The wind factors obtained were substituted in the 12 models in the previous section to hindcast the wind-waves at Xiaomaidao at 1800 hours on 30 August 1939. The results are given in Table 4.

Table 4. Comparison of Various Methods for Wind-Wave*

1.日期 1939年8月	2.风速 (米·秒⁻¹)	3.风时 (小时)	4.风区 (公里)	5.波高 ($H_{1/10}$) 米												
				SM	B₁	K	PNJ	WEN	WANG	B₃	NOR	P	C	WIL	QQQ	H*
30—1800	26.54	8.2	648	10.30	10.17	9.55	6.10	10.09	7.52	8.13	9.0	9.12	5.64	12.99	13.51	7.2
(7) 百分误差(%)				43.0	41.2	32.6	15.3	40.1	4.4	12.9	25.0	26.7	21.7	80.4	87.6	

6. 周期 (T) 秒													
SM	B₁	K	PNJ	WEN	WANG	B₃	NOR	P	C	WIL	QQQ	T*	
6.49	9.78	9.4	8.5	8.46	9.65	8.56	10.8	9.4	6.72	10.80	13.16	11.2	
42.0	12.7	16.1	24.1	24.5	13.8	23.6	3.6	16.1	40.0	3.6	17.5		

*These data are cited from reference 21 Xiaomaidao 50-year return period design wave factors.

Key:
1. Time: August 1939
2. Wind velocity: (m/sec^{-1})
3. Wind-time: (hours)
4. Wind area (km)
5. Wave height ($H_{1/10}$) meters
6. Period (T) seconds
7. Percentage error (%)

If we make the Xiaomaidao 50-year return period design wave factor as the criterion, then from the figures in Table 4 we can tell that: 1) In terms of percent error, the errors of the various methods are smaller than the corresponding methods in Table 2 and Table 3, this seems to mean that the

50

method of determining wind factors is rational and thus the values obtained conform to reality. 2) The wave height values provided using the model in reference 4 are better than the other models, but the best period values are at the same time provided by the norm[20] and Wilson method[10]. 3) The period error is smaller than the wave heights.

The model for forecasting deepwater hurricane wave[19]:

$$\frac{P_r - P_0}{P_a - P_0} = e^{-\frac{R}{r}} \tag{13}$$

$$U_{max} = 0.868[73 \cdot \Delta P^{0.5} - R \cdot (0.575 f)] \tag{14}$$

$$U_R = 0.865 U_{max} + 0.5 V_F \tag{15}$$

$$H_{\frac{1}{3}} = 16.5 e^{\frac{R \cdot \Delta P}{100}} \cdot \left[1 + \frac{0.208 \alpha V_F}{\sqrt{U_R}}\right] \tag{16}$$

$$T_{\frac{1}{3}} = 2.13 \sqrt{H_{\frac{1}{3}}} \tag{17}$$

in which: f (Coriolis parameter) = $2\omega \cdot \sin\phi$; if ϕ is the latitude of the center of the typhoon, 33.4°N, and ω (the earth's angular velocity)= $2\pi/24$ is substituted, we get f = -0.285 arc·hours^{-1}.

α is a parameter which is determined by the forward velocity of a hurricane and the growth of the effective wind area, and for a hurricane moving slowly, it can be assumed to be 1.

      constant pressure p_n = 29.92 hours[19].
      p_0 and p are both pressure, units both are hours.
      $\Delta p = p_n - p_0$.
      units of effective wave height ($H\frac{1}{3}$) and period ($T\frac{1}{3}$) are feet and
        seconds.

If we substitute the data read from the surface weather map at 1800 hours on 30 August 1939:

      the typhoon center's distance r from Qingdao = 360 km;

the atmospheric pressure P_f at a point r distant from the typhoon center, i.e., the Qingdao Station, = 995.9mb* and the data cited in reference 18:

      the atmospheric pressure p_0 in the center of the typhoon = 959.9mb;
      the center of the typhoon advanced at the average velocity
        V_F(=8.095 knots)

---

*Document [18] misread the 30 August 1500 hours weather map time as 1800 hours, thus the corresponding errors are 434 km and 998.6mb.

in equations (13)-(17), then we get:

maximum wind velocity radius R = 76.31 nautical miles;
maximum wind velocity gradient U_{max} at a point 30 feet above the sea
surface = 68.43 knots;
for the moving wind area, the maximum continuous wind velocity U_R at
a point 30 feet above the sea surface = 63.24 knots;
the effective wave height and period at the place of maximum wind
velocity are, respectively,

$$H_{\frac{1}{3}} = 20.19 \text{ meters} \tag{18}$$

$$T_{\frac{1}{3}} = 17.34 \text{ seconds} \tag{19}$$

Assuming that according to reference 19 the most probable largest sea wave
is determined by the number N of waves; and N is determined by the length
of the hurricane's cross section in a zhundingchang [0402 1353 1603] state
and its forward velocity. It has already been shown that the largest sea
waves appeared in a range equivalent in length to the radius of the maximum
velocity, and the time needed for this length to go through a typical point:

$$t = \frac{R}{V_F} = 33936 \text{ sec} \tag{20}$$

thus

$$N = \frac{t}{T_{1/3}} \doteq 1957 \tag{21}$$

the probable maximum wave height, is calculated according to

$$H_n = 0.707 \times H_{\frac{1}{3}} \sqrt{\ln\left(\frac{N}{n}\right)} \tag{22}$$

If we take n = 1, then we get the probable first maximum wave height

$$H_1 = 39.30 \text{ meters} \tag{23}$$

If we substitute this value in equation (17), then we get the corresponding
period

$$T_1 = 24.19 \text{ seconds} \tag{24}$$

III. Conclusion and Discussion

According to incomplete figures, up to the present there have been 36 deep-
water wind-wave forecasting models proposed. We have selected the more
important and often used 12 for verification and comparison and carried out
wind-wave hindcasting for a powerful typhoon that hit Huang Hai, and obtained
the following:

52

(1) In terms of testing the models using the observation data provided by references 6 and 11, the wave height value calculated according to the model in reference 4 was better than that of the other models, the wave height percentage errors were 35 percent and 32 percent, respectively.

(2) We carried out a hindcast of waves in a typhoon in Huang Hai, and using the design wave factors of a 50-year return period wave at Xiaomaidao as the norm, then the method in reference 4 gave better wave height values than the other methods, and the best period value was provided by the norms and Wilson IV method simultaneously.

(3) As for which ratio should be selected for $T_{1/3}/\overline{T}$ is of general significance and will have to be explored further in the future.

(4) The values obtained by converting the materials read from the wind velocity record curves of a single station on the seacoast to serve as wind velocity in a wind area have more significance and also can only be determined after systematic exploration in the future.

(5) As for the examples examined, although among the 12 models selected the method based on reference 4 gave better results, before reaching any final conclusions, more extensive and systematic verification will still be required.

REFERENCES

1. Sverdrup, H.U. and W.H. Munk (1947): WIND, SEA AND SWELL: THEORY OF RELATIONS FOR FORECASTING. U.S. Navy Department, H.O. Pub. 601:1-44.

2. Shandong Haiyang Xueyuan [Shandong College of Oceanology], Haiyangju Diyi Yanjiuso [First Institute of Oceanography, NBO], Kexueyuan Haiyang Yanjiuso [Academy of Sciences Institute of Oceanography] (1980): YIGE JISUAN FENGLANG YAOSUDE JINGYAN GUANXI [AN EXPERIMENTAL RELATIONSHIP OF A CALCULATED WIND-WAVE FACTOR], Haigang Shuiwen Zhuanji [Harbor Hydrographic Editors] (Shuiyun Gongcheng Jishu Ziliao) [Water Transport Engineering Technology Materials] 12, 27-29, Renmin Jiaotong Chubanshe.

3. Wen Shengchang [2429 5110 1603] (1960): PUBIAN FENGLANGPU JI QI YINGONG [GENERAL WIND-WAVE SPECTRUM AND ITS APPLICATION], Shandong Haiyang Xueyuan Xuebao [Journal of Shandong College of Oceanology], No 1 (1960) 15-43, or SCIENTIA SINICA, 9(3):377-402.

4. Wang Bingxiang [3076 3521 4382] (1964): FENGLANGPUDE XINGSHIDE ZAI TANTAO [FURTHER EXPLORATIONS INTO THE FORM OF WIND-WAVE SPECTRUM], Haiyang yu Huzhao [Ocean and Lake], 6(1):23-37.

5. Hou Guoben [0186 0948 2609] and others, tr. (1981): HAIYANG JIANZHUWU DONGLIXUE [MARINE CONSTRUCTION DYNAMICS], Ch 4, Haiyang Chubanshe.

6. Bao Qiangsheng [7637 1730 3932], Ye Jia [0673 5521] (1983): JIZHONG
    ZHUYAO FENGLANG YUBAO FANGFADE YANZHENG YU BIJIAO [VERIFICATION AND
    COMPARISON OF SEVERAL IMPORTANT WIND-WAVE FORECAST METHODS], Haiyang
    Ziliao Qingbao [Marine Materials Newsletter], No 2, 1-7.

7. Bishop, C.T. (1983): COMPARISON OF MANUAL WAVE PREDICTION MODELS,
    J. Waterway, Port, Coastal and Ocean Engineering, 109(1):1-17.

8. Liu, P.C. and M. Asce (1976): APPLICATION OF EMPIRICAL FETCH-
    LIMITED SPECTRAL FORMULAS TO GREAT LAKES WAVES, Proc. 15th Coastal
    Eng. Conf., Ch 8, 113-128.

9. Weigel, R.L. (1964): OCEANOGRAPHICAL ENGINEERING, p 205, Fluid
    Mechanics Series, Prentice Hall, New Jersey.

10. Wilson, B.W. (1965): NUMERICAL PREDICTION OF OCEAN WAVES IN THE NORTH
    ATLANTIC FOR DECEMBER, 1959 (English). Deutsche Hydrographische
    Zeitschrift, Jahrgang 18, Heft 3, 114-130.

11. Krylov, Iu.M. (1958): STATISTICHESKAIA TEORIIA I RASCHET MORSKIKH
    VETOVYKH VOLN [STATISTICAL THEORY AND CALCULATION OF OCEAN WIND-WAVES]
    Part 2, TrGOIN, No 42, 3-88.

12. Rzheplinskii, G.V. (1972): ISSLEDOVANIE REZHIMA VETROVOGO VOLNENIIA
    OKEANOV I RASCHETY PARAMETROV VOLN [RESEARCHES ON THE RATE OF OCEAN
    WIND-WAVES AND CALCULATIONS OF WAVE PARAMETERS], Tr.GOIN, No 111, 3-184.

13. Wang Bingxiang (1962): XINXING FENGLANGPU JI CHI YINGYONG [NEW TYPE
    WIND-WAVE SPECTRUM AND ITS APPLICATION], Haiyang yu Huzhao, 4(3-4):
    142-160.

14. Carter, D.J.T. (1982): PREDICTION OF WAVE HEIGHT AND PERIOD FOR A
    CONSTANT WIND VELOCITY USING THE JONSWAP RESULTS, Ocean Engng., 9(1):
    17-33.

15. Wang Shengchang (1962): HAILANG YUANLI [SEA WAVE PRINCIPLES], Shandong
    Renmin Chubanshe, 396 pp.

16. Goda Yoshizane (1977): HARO KANSOKU KIROKU SHINISUCHI[?] SHUKI TO HA
    KO NO TESUGO BUNSEKI NO KAISEKI, Kowan Giken Shiryo, No 272, 1-19.

17. Shandong Haiyangxueyuan Haiyang Shuiwenxiang Xi [Department of Ocean
    Meteorology, Shandong College of Oceanology] (1964): HAILANG YUBAO
    FANGFA [METHODS OF SEA WAVE FORECASTING], p 93.

18. Liu Xuexian [0491 1331 0341] and Niu Shikui [3662 0013 1145] (1982):
    QINGDAO XINGANGQU TAIFENGLANG GELIE FENXI [ANALYSIS OF TYPHOON WINDS
    IN QINGDAO'S NEW HARBOR], Haiyang Diaochao, No 2, 1982, 23-31.

19. U.S. Army Coastal Engineering Research Center (1973): SHORE PROTECTION
    MANUAL, Vol 1, U.S. Government Printing Office, Washington, D.C.

20. Zhonghua Renmin Gongheguo Jiaotongbu (1978): GANGKOU GONGCHENG JISHU GUIFAN [TECHNICAL NORMS FOR HARBOR ENGINEERING] (Part 2, Vol 1, Haigang Shuiwen), Renmin Jiaotong Chubanshe, p 138.

21. Bao Qiangsheng, Zhang Rongzhen [1728 2837 3932] (1982): QINGDAO WAIHAI JI JIAOZHOUWAN NEI QIANWAN BOLANG YAOSUDE JISUAN [CALCULATING THE WAVE FACTORS IN THE FOREBAY OF JIAOZHOUWAN AND THE SEAS OFF QINGDAO], Hai'an Gongcheng, No 1, 1982, 46-58.

METHODS OF FREQUENCY SPECTRUM ESTIMATION OF SEA WATER COMPARED

[Article by Jiang Decai [5592 1795 2088], Zhang Dacuo [1728 1129 6934], Department of Physical Oceanology and Marine Meteorology, and Gao Xinsheng [7559 2450 3932], Computer Lab: "The Comparison of the Maximum Entropy Method With Conventional One for the Frequency Spectrum Estimation of Sea Wave"; paper received 31 May 1984]

[Text] English Abstract: The principle of the MEM (Maximum Entropy Method) is briefly introduced in this paper. The determination of the length of prediction filter is discussed in the case of the MEM being used for estimating the spectrum of sea wave (wind wave, mixed wave) profile. The quality of the spectrum estimation with MEM and conventional methods is also dealt with under the condition of the same sampling interval and the same sample capacity, it is shown that the MEM has higher resolution, especially for the short series of wave profile records, it is much better than conventional methods.

I. Statement of the Problem

The sea wave power spectrum is a basic characteristic parameter in describing the random processes of sea wave wave surface, it can study the distribution of sea wave energy relative to frequency, as well as study the statistical laws manifested by sea wave wave surface. Thus, it is very important for accurately determining the sea wave frequency spectrum. The correlation and period map methods are the common methods currently used for estimating the sea wave frequency spectrum. They both introduce the subjective will of some hypotheses and certain weight functions. The Maximum Entropy Method (MEM) is a method in which the materials adapt to spectrum estimation. Its window functions are not fixed, it adapts to one frequency and then another, the estimated spectrum values at one frequency are rarely disturbed by variances of other frequencies[1]. In 1972, Ulrych[2] applied Burg[3] MEM to estimate frequency spectra, demonstrating the use of short record materials in spectrum estimation, it had high resolution, and was superior to the common correlation and period map methods. This paper applies the MEM to processing random data of sea wave surface and compares it with the traditional methods of estimating sea wave frequency spectra in the search for a more effective method of estimating sea wave spectra.

The MEM has been applied to many geophysical areas with great results.
There have not been many application to sea wave frequency spectrum estima-
tion. Takahashi Tomoharu et al.[4] (1977) used MEM to estimate the frequency
spectrum of nonstationary ocean wave surfaces and obtained preliminary
results; Tsurutani Ryuichi et al.[5] (1977) used MEM for frequency estimating
of wave surface records of wind-wave trough measurements; Sverre et al.[6]
used MEM to estimate ocean wave surface frequency spectra and discussed the
relationship between the spectrum parameters (spectrum moment) and the final
prediction error filter length. The work of the above-mentioned scholars
showed that using MEM to estimate sea wave frequencies had the advantage of
high resolution, but there is still one common problem, i.e., determining
the length of the prediction error filter in MEM requires combining specific
circumstances of the wave surface (wind-wave, swell, mixed waves). This is
because if the filter length is too short it gives a smoothed spectrum, and
if it is too long, it also gives secondary peaks formed by false signals.
This paper will combine some wave surface records measured by different
instruments in China and use the MEM and traditional methods to estimate
spectra, then compare the spectral forms, spectral moment, and wave factors;
discuss the method for determining the final prediction filter length--the
Akaike fixed stage method and capacity ratio fixed stage method to derive a
more effective method of estimating sea wave frequency spectra.

II. Basic Principles of MEM

MEM estimates directly from the data a minimum phase prediction error
filter, and solves the input power spectrum by using the output power
spectrum $P(f)$ of the prediction error filter and the prediction error
filter spectrum $|H(f)|^2$

$$S(f) = \frac{P(f)}{|H(f)|^2} \tag{1}$$

MEM is a method of extrapolating the auto-correlation function to the outside
of the maximum time lag, its basic idea is to find the entropy maximization
at the time of each extrapolated auto-correlation function. It is not
restricted by the length itself of stationary random process information, it
relies on the predictability of the sampling of both ends for its better
resolution, that is, when the entropy is maximized, the auto-correlation is
extrapolated.

The relationship of entropy and the stationary Gaussian process spectral
density derived according to Smylie[11] (1973)

$$H = \frac{1}{4f_N} \int_{-f_N}^{f_N} \log S(f) df + const \tag{2}$$

in which H is the entropy of the stationary Gaussian process and f_N is
Nyquist frequency.

According to the Wiener-Khintchine relationship

$$\int_{-f_N}^{f_N} S(f)Z^k df = R(k\Delta t) \tag{3}$$

in which $\dot{Z} = \exp(i2\pi f\Delta t)$, Δt is the uniform sampling step length, $R(k\Delta t)$ is the auto-correlation function which has a time lag $(k\Delta t)$. The MEM ends up as a variation problem of solving equation (2) relying on equation (3) as the limiting condition, and the solution to the variation problem is

$$S(f) = \left(\sum_{k=-m}^{m} \lambda_k Z^k \right)^{-1} \tag{4}$$

in which λ_k is the Lagrange multiplier, determined by equation (3). The ocean power spectrum (frequency spectrum) is a real number and non-negative, thus equation (4) can be rewritten

$$S(f) = \frac{P_m/2f_N}{\left| 1 - \sum_{k=1}^{m} a_{m,k} Z^k \right|^2} \tag{5}$$

in which $\left(1 - \sum_{k=1}^{m} a_{m,k} Z^k \right)$ is the minimum phase, P_m is the average output power of the $m + 1$ prediction error filter. Rewriting equation (3) as

$$S(f) = \frac{1}{2f_N} \sum_{k=-m}^{m} R(k\Delta f)Z^{-k} \tag{6}$$

comparing the equal coefficients of Z in equations (5) and (6), and taking into account that $R(k\Delta t)$ is an even function, we get

$$\begin{pmatrix} R_0 R_1 \cdots R_m \\ R_1 R_0 \cdots R_{m-1} \\ \vdots \\ R_m R_{m-1} \cdots R_0 \end{pmatrix} \begin{pmatrix} 1 \\ -a_{m,1} \\ \vdots \\ -a_{m,m} \end{pmatrix} = \begin{pmatrix} P_m \\ 0 \\ \vdots \\ 0 \end{pmatrix} \tag{7}$$

the first matrix on the left is the Toeplitz matrix. The minimum phase filter coefficient $a_{m,k}$ and the average output power P_m are determined by equation (7).

Suppose that the data of an actual sea wave surface event is already known and is expressed as $\zeta_1, \zeta_2, \ldots, \zeta_n$, the forward and backward prediction error filters designed by Burg[7] (1967) are the coefficients $a_{m,k}$ determined by the prediction error square average (output power) minimization. The output power P_1 of the two prediction error filters $(1, a_{1,1})$ wave surface sequence $\zeta_i (i = 1, 2, \ldots, n)$ through the forward and backward prediction error filters

58

$$P_1 = \frac{1}{2(n-1)} \sum_{i=1}^{n-1} [(\zeta_i - a_{1,1}\zeta_{i+1})^2 + (\zeta_{i+1} - a_{1,1}\zeta_i)^2]$$ (8)

in which $(\zeta_1 - a_{1,1}\zeta_{i+1})$ is the ζ_1 backward prediction error, $(\zeta_{i+1} - a_{1,1}\zeta_i)$ is the ζ_1 forward prediction error, and if we wish to minimize the average output power, then $2P_1/2a_{1,1} = 0$, we have

$$a_{1,1} = 2 \sum_{i=1}^{n} \zeta_i \zeta_{i+1} \Big/ \sum_{i=1}^{n-1} (\zeta_i^2 + \zeta_{i+1}^2)$$ (9)

From equation (9) we can see that $a_{1,1} < 1$ is the minimum phase prediction error filter.

From equation (7) we get

$$R_1 = a_{1,1} R_0$$

$$P_1 = (1 - a_{1,1}^2) R_0$$ (10)

$$R_0 = \frac{1}{n} \sum_{i=1}^{n} \zeta_i^2$$

and applying the Levinson recursion formula

$$a_{m,k} = a_{m-1,k} - a_{m,m} a_{m-1,m-k}$$ (11)

which means that the filter coefficient $a_{m,k}$ relies on $a_{m,m}$ and we stipulate $a_{m,0} = -1$, when $k>m$, $a_{m,k} = 0$, the equation (11) is established for all m. $(m+1)$ prediction error filter output power P_m is

$$P_m = \frac{1}{2(n-m)} \sum_{i=1}^{n-m} \left[\left(\sum_{k=0}^{m} a_{m,k}\zeta_{i+k} \right)^2 + \left(\sum_{k=0}^{m} a_{m,k}\zeta_{i+m-k} \right)^2 \right]$$

$$= \frac{1}{2(n-m)} \sum_{i=1}^{n-m} [(B_{mi} - a_{m,m}B'_{mi})^2 + (B'_{mi} - a_{mm}B_{mi})^2]$$ (12)

in which

$$B_{mi} = \sum_{k=0}^{m} a_{m-1,k}\zeta_{i+k} = \sum_{k=0}^{m} a_{m-1,m-k}\zeta_{i+m-k}$$ (13a)

$$B'_{mi} = \sum_{k=0}^{m} a_{m-1,k}\zeta_{i+m-k} = \sum_{k=0}^{m} a_{m-1,m-k}\zeta_{i+k}$$ (13b)

The $(m+1)$ term prediction error filter's average output power minimization conditions $\partial P_m/\partial a_{m,m} = 0$, expressed by equation (12) have

59

$$a_{m,m} = \frac{2 \sum\limits_{i=1}^{n-m} B_{mi} B'_{mi}}{\sum\limits_{i=1}^{n-m} (B_{mi}^2 + B_{mi}'^2)} \tag{14}$$

From equations (11) and (13) we obtain the recursion formula of B_{mi}, B'_{mi}

$$B_{mi} = B_{m-1,i} - a_{m-1,m-1} B'_{m-1,i} \tag{15a}$$

$$i = 1, 2, \cdots, m$$

$$B'_{mi} = B'_{m-1,i+1} - a_{m-1,m-1} B_{m-1,i+1} \tag{15b}$$

The number groups B_{mi} and B'_{mi} are made up of B_{m-1} and $B'_{m-1,i}$ multiplied by a simple linear operation, the initial value $B_{0i} = B'_{0i} = \zeta_i$ and the value of B_{1i} and B_{1i} is

$$B_{1i} = \zeta_i \qquad (i = 1, 2, \cdots, n) \tag{16a}$$

$$B'_{1i} = \zeta_{i+1} \qquad (i = 1, 2, \cdots, n-1) \tag{16b}$$

Substituting equation (11) in equation (7) we get the recursion formula of P_m

$$P_m = P_{m-1}(1 - a_{m,m}^2) \tag{17}$$

Using equations (11), (14), (15), (16), and (17) we can directly solve the prediction error filter's coefficient $a_{m,k}$ and the prediction error filter's minimum average output P_m directly from the raw data ζ_1, ζ_2, ..., ζ_n, and estimate the ocean wave spectrum by equation (6). Represented as a circular frequency, equation (6) has

$$S(\omega) = \frac{1}{2\pi} \frac{P_m \Delta t}{\left| 1 - \sum\limits_{k=1}^{m} a_{m,k} Z^k \right|^2} \tag{18}$$

the sea wave spectrum is generally expressed as a single-sided spectrum $E(\omega) = 2S(\omega)$. Then the sea wave factors can be calculated through the spectral moment M_k

$$M_k = \int_0^\infty \omega^k E(\omega) d\omega \tag{19}$$

the average wave height: $\qquad \overline{H} = \sqrt{2\pi M_0} \tag{20}$

the average period: $\qquad \overline{T} = 2\pi \sqrt{\frac{M_0}{M_2}} \tag{21}$

the spectral width: $\qquad \varepsilon = \sqrt{\frac{M_0 M_4 - M_2^2}{M_0 M_4}} \tag{22}$

The length m(<n) of the prediction error filter influences the quality of the MEM estimate, determining the filter length m proper is an important issue in MEM estimates. We used the Akaike (1969a)[8], 1969b[9] and 1970[10] fixed stage method and capacity ratio fixed stage method to determine the prediction error filter length for the different kinds of information of wind-wave, swell, and mixed wave. In this paper, the Akaike step determining method took the first very small value of the minimal final prediction error (EPE) and for centralized sampling we had

$$(EPE)_m = \frac{N+m+1}{N-(m+1)} P_m \tag{23}$$

in which N is the sample capacity, m is the prediction error filter length. In the capacity ratio fixed stage method, we took

$$m = N/20 \tag{24}$$

III. Comparison of Spectral Estimates

We used different information materials (wind-wave, mixed wave) observed by different wave measuring instruments (water pressure type, gravity type, ultrasonic type). We applied auto-correlation, period mapping, and MEM for spectrum estimating and in MEM also took the prediction error filter length m determined by equations (23) and (24).

1. Comparison of Methods for Spectrum Estimating

Figures 1, 2, and 3 give the wind-wave materials observed by the water pressure wave measuring instruments, all used a sampling step length of $\Delta t = 0.375$ second, and the spectrum curve of the various methods of estimating the spectrum where sample capacities were N = 2048, 1024, and 512, respectively. In the figures, COV represents the auto-correlation function method, FFT represents the period mapping method, MES represents MEM. In the figures, in the conventional methods, k represents the free degrees, in MEM it represents prediction error filter length k, Akaike's fixed stage method is determined by the self selected first extremely small value, therefore the value k is not clearly noted. In the figures, the solid line is the spectrum curve of Akaike's fixed stage method MEM spectrum estimate. From the three figures one can see that the MEM extreme value is higher than the extreme value given by the conventional spectrum estimation, and that the curve is smooth, indicating that the spectrum deviation is small. However, in Figure 1, when N = 2048, the extreme value of the Akaike fixed stage spectrum estimation is lower than the spectrum value estimated by the capacity ratio stage fixed at N/20 method. From the figures, it can be seen that MEM spectrum estimating is generally superior to the conventional method, the application of Akaike's method of determining m by the criterion of the first extremely small value is feasible in wind-wave information, because the two methods of determining m in MEM, when capacity N is large, the capacity determinant ratio method displays better spectrum extreme values, but the high frequency spectrum values are not as smooth as the Akaike fixed stage method. From Figures 1 to 3, when the sample capacity N shrinks to N/2 or

61

N/4, the spectrum values estimated by MEM have a spectrum curve similar to N, indicated the superiority of MEM for short series spectrum estimating.
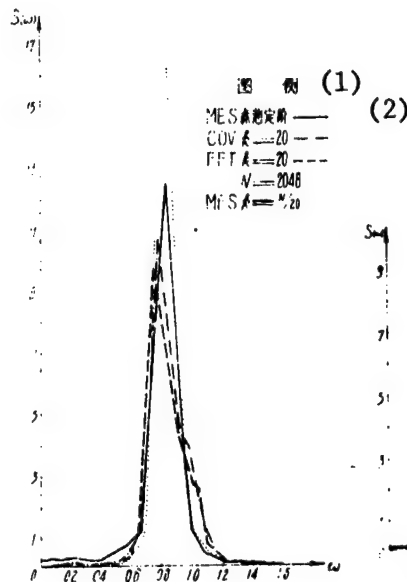

Figure 1. Spectrum Estimate (water pressure wave measurement record, N = 2048)
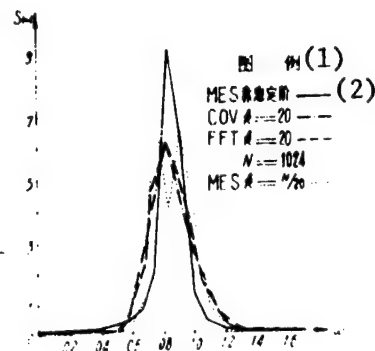
Key:
1. Legend
2. Akaike fixed stage

Figure 2. Spectrum Estimate (water pressure wave measurement record, N = 1024)
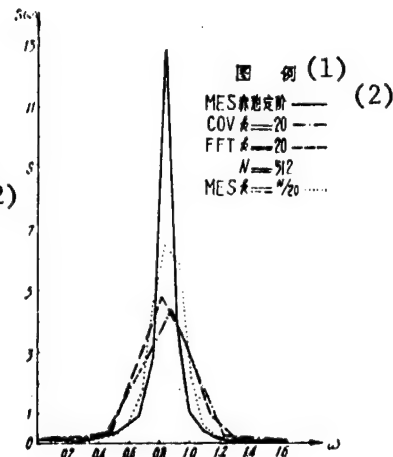
Key:
1. Legend
2. Akaike fixed stage

Figure 3. Spectrum Estimate (water pressure wave measurement record, N = 512)

Key:
1. Legend
2. Akaike fixed stage

Figures 4, 5, and 6 give the wind-wave materials observed by ultrasonic wave measuring device. The step length for all samples was Δt = 0.75 seconds, and the spectrum curve of the various methods of estimating the spectrum where sample capacities were N = 1024, 512, and 256, respectively. The solid line in the figure represents spectrum curve of the MEM estimate with capacity ratio stage fixed at N/20. Discussing the quality of the spectrum estimate from the angle of the spectrum's piandu [0252 1653 bias?] and deviation, we see that the extreme value of the spectrum estimated by the capacity fixed ratio method is the highest, but the fact that degree of freedom k = 20 in the high frequency spectrum value curve and the auto-correlation function method is rather uniform means that the capacity fixed ratio N/20 for estimating the spectrum values is rather good. The broken line in the figures represents the spectrum curve of the Akaike fixed stage MEM, the high frequency partial spectrum value deviation is small, and it is also superior to the spectrum curve of the estimate of degree of freedom k = 20 of the auto-correlation method. Therefore, Akaike

62

fixed stage MEM estimated spectrum is better. When the sample capacity is reduced by doubling [chengbei 2052 0223], the MEM spectrum estimate give an excellent spectrum curve.
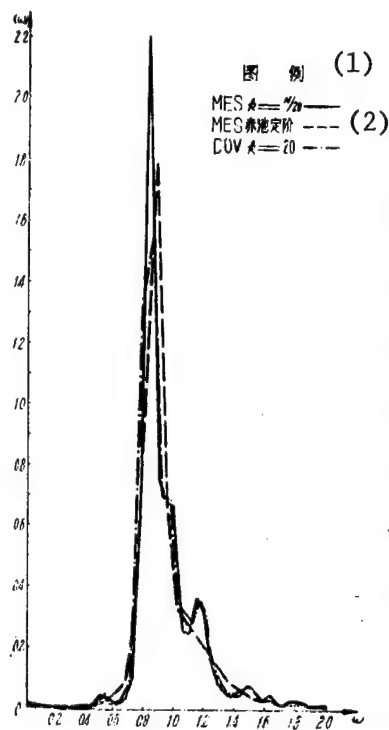

Figure 4. Spectrum Estimate (ultrasonic wave measurement record, N = 1024)
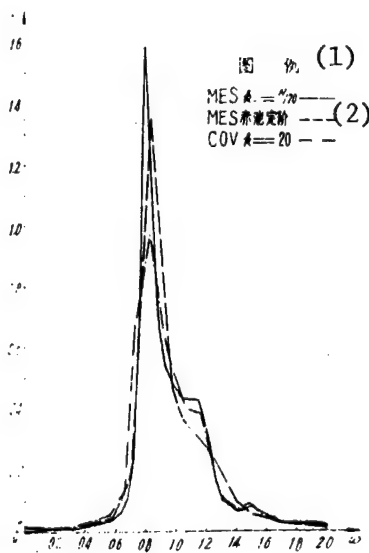
Key:
1. Legend
2. Akaike fixed stage

Figure 5. Spectrum Estimate (ultrasonic wave measurement record, N = 512)
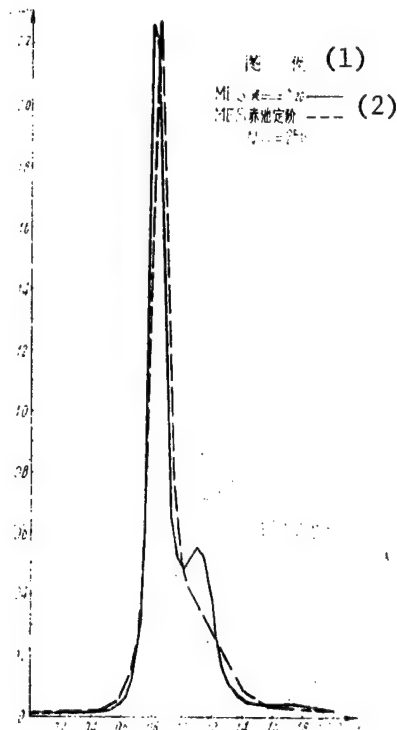
Key:
1. Legend
2. Akaike fixed stage

Figure 6. Spectrum Estimate (ultrasonic wave measurement record, N = 256)

Key:
1. Legend
2. Akaike fixed stage

Figures 7, 8, and 9 give the mixed wave materials observed by the gravity wave measuring device. The spectrum curve of the various methods of estimating the spectrum where the step length for all samples was Δt = 0.75 seconds, and where sample capacities were N = 1024, 512, and 256, respectively. The solid line in the figure representing the spectrum curve of the MEM estimate at a capacity ratio fixed stage of N/20, is superior to the spectrum curve of the conventional method and the Akaike fixed stage MEM. The MEM spectrum curve given by the Akaike first extremely small value discrimination method is a spectrum that tends to be smoothed, and the spectrum extreme value is lower than the conventional method, the corresponding frequency position difference for the spectrum extreme value is also greater. This indicates that the prediction error filter length m determined

by the Akaike first extremely small discrimination method is suited to spectrum estimates of the pure Gaussian processes, and for mixed wave information is given a smoothed spectrum.
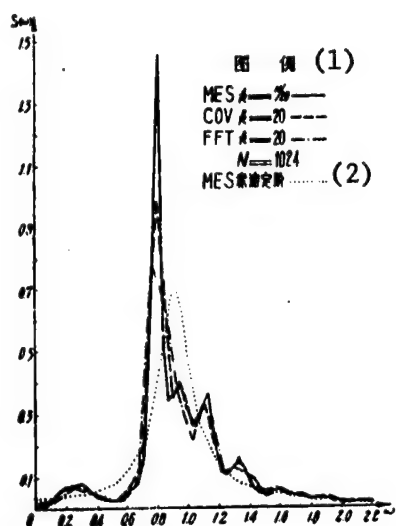

Figure 7.   Spectrum Estimate (gravity wave measurement record, N = 1024)

Key:
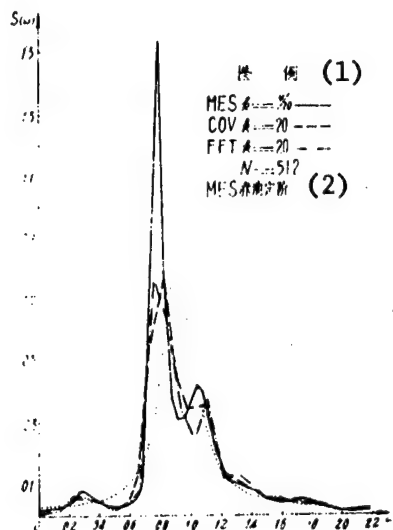   1.   Legend
    2.   Akaike fixed stage

Figure 8.   Spectrum Estimate (gravity wave measurement record, N = 512)
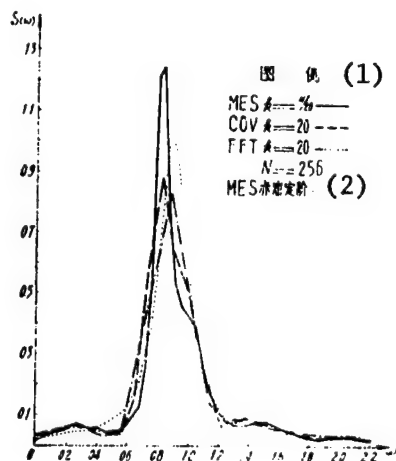
Key:
    1.   Legend
    2.   Akaike fixed stage

Figure 9.   Spectrum Estimate (gravity wave measurement record, N = 256)

Key:
    1.   Legend
    2.   Akaike fixed stage

64

2. Comparison of Spectrum Moment and Wave Factors

Table 1 gives the spectrum moment M_0, M_2, M_4, spectrum width and average wave height, and average period of the wind-wave materials observed by the pressure wave measuring device. In the first column, MESA represents the calculated spectrum moment and wave factors by the Akaike fixed stage MEM estimated spectrum, MESB represents the capacity ratio N/20 fixed state MEM, COV is the auto-correlation function method, FFT is the period mapping method. From Table 1 it can be seen that sample capacity N = 2048, 1024, 512 correspond to the spectrum moments M_0, M_2 and average wave height $\overline{H}$, average period $\overline{T}$, and spectrum width calculated by the various methods are all fairly close, only the relative changes in M_4 are larger. However, for actual application, the above described parameters are sufficiently precise, therefore the spectrum moments and wave factors estimated by the various methods have practical significance. The wind-wave materials measured by the ultrasonic wave measuring device also produced similar results, and they will not be tabulated and explained here.

Table 1. Comparison of Spectral Moment and Wave Factors (wind-wave materials)

(1)方 法	(2)容量N	M_0	M_2	M_4	ε	$\overline{H}$	$\overline{T}$
MESA	2048	2.298	2.017	16.172	0.944	3.800	6.71
MESB	2048	2.377	2.081	16.280	0.942	3.861	6.71
COV	2048	2.444	2.101	13.905	0.933	3.918	6.78
FFT	2048	2.407	2.094	15.404	0.939	3.889	6.74
MESA	1024	1.890	1.750	10.267	0.937	3.450	6.53
MESB	1024	2.070	1.878	13.308	0.934	3.607	6.60
COV	1024	2.040	1.810	11.043	0.924	3.581	6.67
FFT	1024	1.998	1.808	13.044	0.935	3.540	6.61
MESA	512	2.060	1.840	11.410	0.937	3.60	6.65
MESB	512	2.004	1.808	13.306	0.937	3.55	6.62
COV	512	2.020	1.750	10.450	0.924	3.56	6.75
FFT	512	1.919	1.712	12.589	0.937	3.47	6.65

Key:
1. Method
2. Capacity N

Table 2 gives the mixed wave materials measured by the gravity wave measuring device, and applies the spectrum moment, spectrum width and wave factors calculated for the estimated spectrum by the various methods. From Table 2 it can be seen that the statistical values found for the spectra estimated by the various methods are all very close, and have practical significance. The statistical values (spectrum moment and wave factors) of Tables 1 and 2 explain that whether wind-wave or mixed wave, although there are great differences in the spectrum curves estimated by the various methods, the statistical values are very close and can be used for general engineering.

Table 2. Comparison of Spectral Moment and Wind Factors (mixed waves)

(1)方 法	(2)容量N	M_0	M_2	M_4	ε	$\overline{H}$	$\overline{T}$
MESA	1024	0.321	0.450	1.912	0.818	1.419	5.30
MESB	1024	0.320	0.449	1.901	0.813	1.418	5.30
COV	1024	0.312	0.445	1.885	0.817	1.412	5.30
FFT	1024	0.310	0.434	1.790	0.813	1.396	5.31
MESA	512	0.336	0.457	1.898	0.820	1.453	5.39
MESB	512	0.335	0.456	1.887	0.819	1.451	5.39
COV	512	0.329	0.448	1.845	0.818	1.437	5.38
FFT	512	0.301	0.421	1.742	0.914	1.376	5.31
MESA	256	0.385	0.564	2.855	0.843	1.555	5.19
MESB	256	0.385	0.564	2.865	0.843	1.555	5.19
COV	256	0.370	0.547	2.752	0.841	1.525	5.17
FFT	256	0.344	0.515	2.532	0.841	1.471	5.19

Key:
1. Method
2. Capacity N

IV. Conclusion

1. For wind-wave materials measured by water pressure wave measuring devices, the spectrum curve estimated using the Akaike first very small value fixed stage MEM is superior to the spectrum curve estimated by the conventional method and the capacity ratio N/20 fixed stage MEM.

2. For the wind-wave materials measured by the ultrasonic wave measuring device, when the sample capacity $N \geq 512$, the spectrum values estimated using the capacity ratio N/20 fixed stage MEM are better, and it is superior to the conventional method and the Akaike fixed stage MEM, when N = 256, the spectrum values estimated by the two fixed stage MEM are close. This indicates that when the ultrasonic wave measuring records which directly reflect the wind-wave information are used to estimate the spectrum, the smoother spectrum produced by the Akaike fixed stage MEM has a resolution lower than the capacity ratio N/20 fixed stage MEM and is superior to conventional method of estimating spectra. For convenience of use, we can use the Akaike fixed stage MEM.

3. For mixed waves, the spectrum estimated by the Akaike fixed stage MEM gives a smoothed spectrum, resolution is lower than or equal to the conventional spectrum estimate, but the capacity ratio N/20 fixed state MEM estimated spectrum displays better resolution and is superior to spectrum values estimated by conventional methods. Therefore, when the Akaike fixed stage MEM is used to estimate the spectra of mixed wave materials, it is still necessary to improve the discrimination standards for determining the prediction error filter length. Otherwise, carrying out test

calculations using the capacity ratio fixed stage method is like trials using the conventional method with different degrees of freedom to discriminate the optimum quality spectrum estimate.

4. Although in using the various methods to carry out spectrum estimates on wind-wave (6 groups) and mixed wave (4 groups) wave surface records measured by different devices there are differences in the spectrum structures and difference deviations and biases are revealed, the statistical parameters--spectrum moment, spectrum width, average wave height, average period--through calculations of the estimated spectrum are all fairly close and all have practical significance.

5. For short sample capacities, the Akaike fixed stage MEM estimated spectrum exhibited that it is even more superior to the conventional spectrum estimating method.

REFERENCES

1. J.S. Goerss and A.J. Kosicelny, 1977: FIFTH CONFERENCE ON PROBABILITY AND STATISTICS IN ATMOSPHERIC SCIENCE, 1977, pp 297-302.

2. Ulrych, T.J., 1972: MAXIMUM ENTROPY POWER SPECTRUM OF TRUNCATED SINUSOIDS, J. Geophys. Res., 77, 1396-1480.

3. Burg, J.P., 1968: A NEW ANALYSIS TECHNIQUE FOR TIME SERIES DATA. Paper presented at Advanced Study Institute of Signal Processing, NATO, Enschede, Netherlands.

4. Takahashi Tomoharu [?], 1977: CONSIDERATION ON WAVE SPECTRA ESTIMATION BY MEM (MAXIMUM ENTROPY METHOD), (1) Kowan Giken Shiryo, No 273.

5. Tsurutani Ryuichi, (1977): CONSIDERATION ON WAVE SPECTRA ESTIMATION BY MEM (MAXIMUM ENTROPY METHOD), (2) Kowan Giken Shiryo, No 274.

6. Sverre Holm and Jensm Hovem, 1979: ESTIMATION OF SCALAR OCEAN WAVE SPECTRA BY THE MAXIMUM ENTROPY METHOD, IEEE J of Ocean Engineering, 1979.

7. Bury, J.P., 1967: MAXIMUM ENTROPY SPECTRAL ANALYSIS, Paper presented at the 37th Annual International Meeting, Soc. of Explor. Geophys., Oklahoma City, Okla.

8. Akaike, H., 1969a: FITTING AUTOGRESSIVE MODELS FOR PREDICTION, Ann. Inst. Statist. Math. 21.

9. Akaike, H., 1970: STATISTICAL PREDICTOR IDENTIFICATION, Ann. Inst. Statist. Math., 22.

10. Akaike, H., 1969b: POWER SPECTRUM ESTIMATION THROUGH AUTOREGRESSIVE MODEL FITTING, Ann. Inst. Statist. Math., 21.

11. Van den Bos, A., 1971: ALTERNATIVE INTERPRETATION OF MAXIMUM
    ENTROPY SPECTRAL ANALYSIS, IEEE Trans. on Inform. Theory, IT-17,
    4:493-494.

PHASE SPEED OF WIND-WAVE COMPONENT STUDIED

[Article by Xu Delun [1776 1795 0243], Department of Physical Oceanology and Marine Meteorology: "Measurements of Phase Speed of Wind-Wave Component and Interpretation of Their Result"; article received 30 June 1984]

[Text] English Abstract: Measurements of phase speed of wind-wave component were made by cross-spectrum method, separation distance between the two probes for measuring surface elevations being 2 cm.

The measured data indicate that the relationship between phase speed and frequency varies with wind speed and water depth. For one extreme condition, low wind and deep water, it obeys basically the classical linear dispersion relation. For the other extreme condition, high wind and shallow water, the components are non-dispersive, all traveling with the same speed as the component with spectrum-peak frequency. For medium conditions, the dispersion relations have some forms between the two extreme cases.

The measured result can be interpreted on the basis of a refined spectral model, which consists of the contributions of both dispersive and non-dispersive wave with the effect of drift current included. At low wind and in deep water, the wave field is of low nonlinearity: free waves are dominant and, hence, the wave components are dispersive and obey the classical dispersion relation. At high wind and in shallow water, the wave field has high nonlinearity. In this case, forced waves dominate over free waves and the wave components appear to be non-dispersive.

I. Introduction

Linear wave spectrum theory holds that wind-waves are the result of the linear superposition of simple waves of many frequencies, unequal oscillation and confused phase. According to this theory, the phase velocity of wind-waves should obey linear wave dispersion relation $c = g/n$ (n is circular frequency, g is gravitational acceleration). Does this theory really conform to a large degree to the actual wind-wave conditions? The answer relies on accurate measurements of wind-wave phase velocity. Ramamonjiarisoa

(1974)[1] of the Marseille Laboratory in France used the cross-spectrum method
to measure and obtain data. This data indicated that only the wave component
of the wind-wave whose frequency was near the spectrum peak frequency obeyed
the linear dispersion relation, wave components with higher frequencies were
non-dispersive, and both were propagated at almost identical phase velocities.

The measurement data of Ramamonjiarisoa (1974) attracted wide attention.
Some researchers (Huang, 1981; Dudis, 1981, et al.) expressed doubts about
the measurement method of this data. Through a strict theoretical analysis,
Huang (1981) pointed out that the distance between the two probes which
Ramamonjiarisoa (1974) used in measuring wave surface height was too great
(10 cm) and thus he could not measure the phase velocity of wave components
at higher frequencies. In addition, Ramamonjiarisoa's measurement data was
only obtained at medium velocity, and lacks data at low wind speed and higher
wind speeds.

This paper first of all reports the laboratory measurement results. These
data were still obtained using the cross-spectrum method, but the distance
between the probes was reduced to 2 cm, and the results include various
situations such as from low wind speed (3 m/sec) to higher wind speeds
(14 m/sec) and shallow water. Finally, there is a theoretical interpretation
of the measured results.

II. Cross-Spectrum Method

The definition of cross-spectrum $\Psi(\vec{r},n)$ is

$$\Psi(\vec{r},n) = \int_{\vec{k}} \Phi(\vec{k},n) \; e^{i\vec{k}\cdot\vec{r}} \, d\vec{R} \tag{1}$$

in which, $\phi(\vec{R},n)$ is the wave number-frequency spectrum, $\vec{k}$ is the vector wave
number, n is the circular frequency, $\vec{r}$ is the vector distance between the two
measuring probes.

The phase spectrum function can be found from the cross-spectrum

$$\theta(\vec{r},n) = \tan^{-1}\left[\frac{Q(\vec{r},n)}{C_0(\vec{r},n)}\right] \tag{2}$$

in which C_0 and Q are the real parts (equal phase spectrum) and false parts
(out-of-phase spectrum), of the cross-spectrum $\Psi(\vec{r},n)$, i.e.,

$$C_0(\vec{r},n) = \int_{\vec{k}} \cos(\vec{k},\vec{r}) \phi(\vec{k},n) d\vec{k}$$

and

$$Q(\vec{r},n) = \int_{\vec{k}} \sin(\vec{k},\vec{r}) \phi(\vec{k},n) d\vec{k}$$

70

If the wind-wave is propagated only in the single direction $\vec{r}$, then the phase velocity spectrum of the wind-wave component can be found from the wei [0143 positional?] phase spectrum

$$c(n) = \frac{rn}{\theta(r,n)}$$

(3)

This equation is the one used by Yefimov et al. (1972)[2] and Ramamonjiarisoa et al. (1979)[3] to calculate the wind-wave component phase velocity.

After stricter theoretical deductions, Huang (1981)[4] stated: The suitable conditions for equation (3) only limited to wave field is unidirectional, and the distance between the two probes must be small enough to satisfy the condition

$$|\vec{k},\vec{r}| \ll 1$$

(4)

III. Experiment and Results

Experiments were carried out in a wind-wave-flow experimental trough at the University of Delaware in the United States. The trough length was 44 meters, 1 meter wide and the water depth at the time of the experiment was 0.75 meters. Two capacitance wave measuring devices were used for measurement of the wave surface height. The distance between the two probes was 2 centimeters. Four groups of measurement data were obtained in all. Three of the groups were taken in a wind area of 30 meters, at wind speeds of 3, 8, and 14 m/sec, respectively; the other group was taken in shallow water on a slope at the end of the trough, wind speed was 12 m/sec. The recording time of each group of data was 304 seconds. The sectional direct method was used for estimating the frequency spectrum, each 304 second record was broken up into 38 sections. The sampling rate was 64 Hz, there were 19456 data points in each group, and 512 data points in each section. The frequency ($f = \frac{n}{2\pi}$) resolution of the cross-spectrum used for estimate results was 0.125 Hz, and its degree of freedom was 76.

Since the water trough was narrow, we could more or less accept that the wave field measured was unidirectional. Probe distances of 2 cm make the wave components below a frequency of 5 Hz satisfy condition (4) very well. This means that the results of the measurement are effective for wave components of below a frequency of 5 Hz. The phase velocity relative frequency f points calculated according to equations (2) and (3) from the wave surface records are plotted in Figures 1, 2, and 3. For ease of comparison, two separate curves are also plotted in these figures. The solid line is the theoretical curve calculated from the linear wave dispersion relation (including the influence of surface tension T).
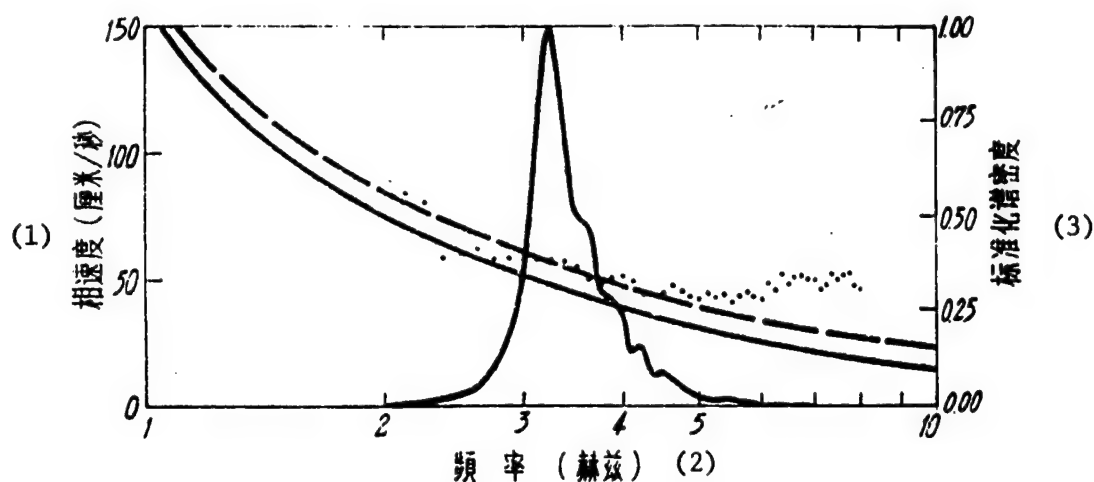
71

Figure 1. Relationship of Frequency and Phase Velocity of Wind-Wave Component
at Low Wind Speed (Wind speed is 3 m/sec, water depth is 75 cm)

Key: 1.   Phase velocity (cm/sec)
       2.   Frequency (Hz)
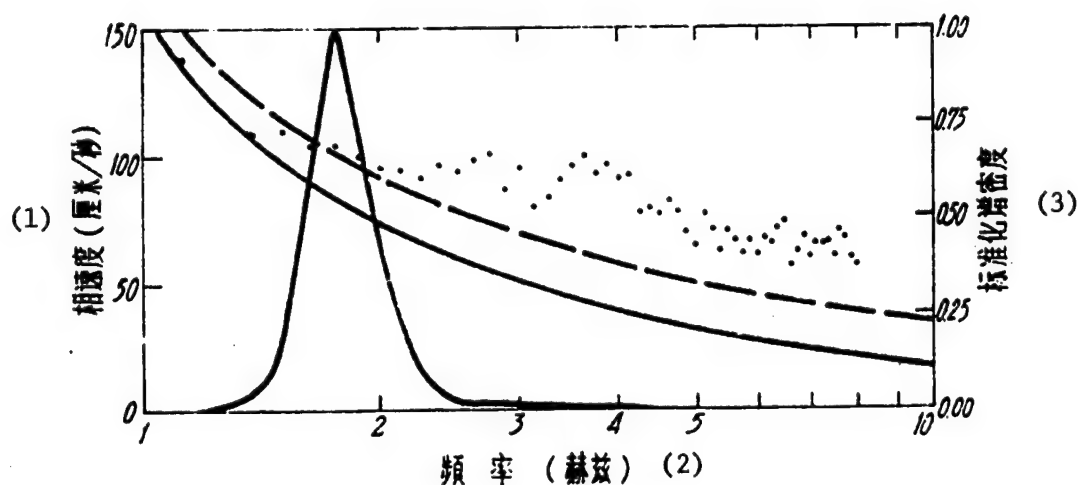   3.   Standardized spectrum density

Figure 2. Relationship of Frequency and Phase Velocity of Wind-Wave Component
at Medium Wind Speed (Wind speed is 8 m/sec, water depth is 75 cm)

Key:
       1.   Phase velocity (cm/sec)
       2.   Frequency (Hz)
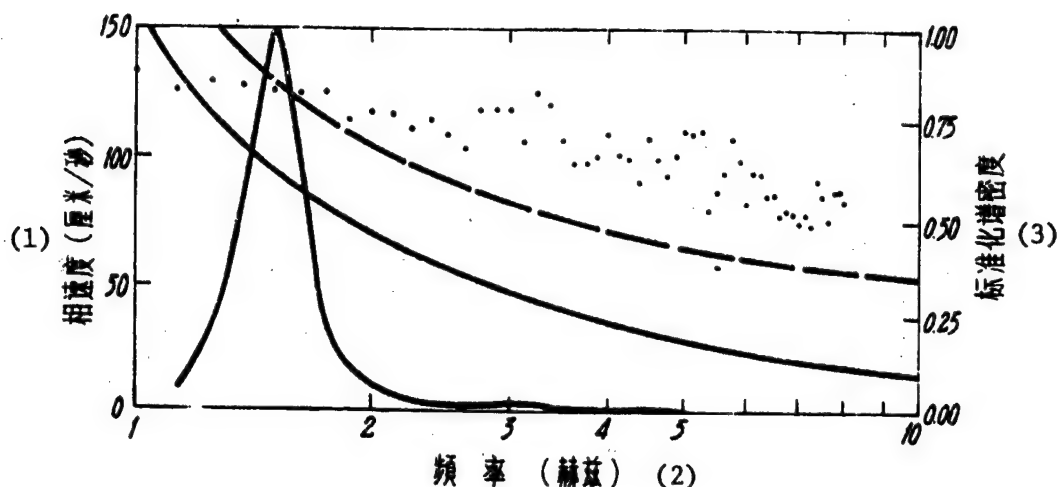   3.   Standardized spectrum density

72

Figure 3. Relationship of Frequency and Phase Velocity of Wind-Wave Component at Higher Wind Speed (Wind speed is 14 m/sec, water depth is 75 cm)

Key:
1. Phase velocity (cm/sec)
2. Frequency (Hz)
3. Standardized spectrum density

$$c = \sqrt{\frac{g\lambda}{2\pi} \frac{\rho - \rho'}{\rho + \rho'} + \frac{2\pi T}{\lambda(\rho + \rho')}} \tag{5}$$

(in which ρ and ρ' are water and air density, respectively and λ is wave length); the broken line was obtained from the right side of equation (5) plus the phase velocity c_u which increases because of wind drift, i.e., from the equation

$$c' = \sqrt{\frac{g\lambda}{2\pi} \frac{\rho - \rho'}{\rho + \rho'} + \frac{2\pi T}{\lambda(\rho + \rho')}} + c_u \tag{6}$$

In the laboratory, the drift produced by the wind had a very clear impact on wind-wave velocity. We do not yet have a theoretical method to calculate this impact, nor do we have actual measurement results which can be used. For ease of comparison, we use approximations [?], we view the differences at the spectral peak frequencies of velocity measured by the cross-spectrum method and the velocity provided by the linear dispersion relation as wave component phase velocity of value c_u which increases because of wind drift.

From Figures 1-3 it can be clearly seen that at different wind speeds, the tendency of wind-wave component phase velocity which was measured changes with frequency are slightly different. At low wind speeds (3 m/sec), the measurement data of frequencies below 5 Hz fits fairly well with the theoretical curve. At medium wind speeds (8 m/sec), beginning with a frequency of 2.3 Hz, the measurement data systematically deviates from the theoretical curve. This is generally the same as the results measured by

73

Ramamonjiarisoa. As the wind speed increases, the starting point where the measurement data deviates from the theoretical curve shifts toward lower frequencies. At 14 m/sec wind speed, it has already shifted to approximately 2 Hz in the vicinity of the spectrum peak.

In the experiment we also measured the shallow water situation. The results are displayed in Figure 4. The measurement points were on the slope at the end of the trough, the water depth at the place of measurement was 7.5 cm and the wind speed was 12 m/sec. It is very clear that under these conditions, beginning with the spectrum peak frequency (1.3 Hz), the phase velocity of the wind-wave component was almost maintained as a constant, and the wave component was non-dispersive.
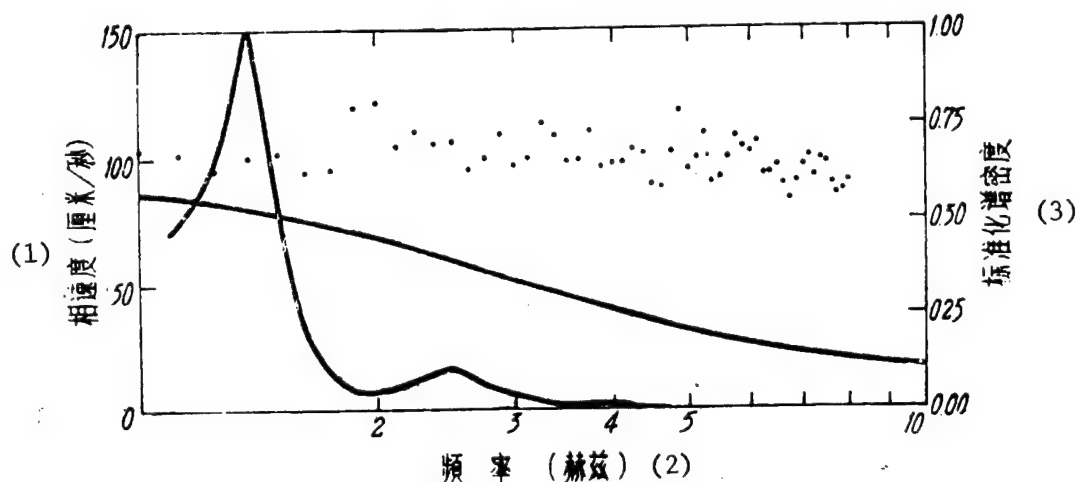

Figure 4. Relationship of Frequency and Phase Velocity of Wind-Wave Component in Shallow Water (Wind speed is 12 m/sec, water depth is 7.5 cm)

Key:
1. Phase velocity (cm/sec)
2. Frequency (Hz)
3. Standardized spectrum density

Summing up the above, the tendency of wind-wave component phase velocity relative to changes in frequency is very closely related to the wind wave field situation, and does not uniformly obey the linear dispersion relation.

IV. Interpretation of Results

Recent wave spectrum theory[5] holds that: the wind-wave spectrum is made up of non-dispersive waves (also called forced waves) and dispersive waves (also called free waves). Referring to the model proposed by Dudis (1981)[6] and taking into account the effect of wind drift, we proposed the following frequency-wave number spectrum model for unidirectional wave fields:

$$\phi(\vec{k}, n) = \phi_N(n) \, \delta\left(k - \frac{n}{c_N + c_u}\right) + \phi_D(n) \cdot \delta\left(k - \frac{n^2}{g + nc_u}\right) \tag{7}$$

in which ϕ_N and ϕ_D represent, respectively, the contributions of non-dispersive and dispersive waves to the frequency spectrum, c_N is the phase velocity of the non-dispersive waves, c_u is the phase velocity of the wave component increased due to wind drift, and δ represents the Dirac delta function.

Substituting equation (8) in equation (2) we get

$$\tan\theta(n) = \frac{\mu(n)\sin\dfrac{rn}{c_N + c_u} + \sin\dfrac{rn^2}{g + c_u n}}{\mu(n)\cos\dfrac{rn}{c_N + c_u} + \cos\dfrac{rn^2}{g + c_u n}} \tag{8}$$

in which

$$\mu(n) = \frac{\phi_N(n)}{\phi_D(n)} \tag{9}$$

is the ratio of the contributions to the frequency spectrum of non-dispersive waves and dispersive waves. In a research report, Xu et al. (1984)[7] solved $\mu(n)$ as a function of effective wave surface slope $\zeta = \dfrac{(\overrightarrow{\zeta^2})^{1/2}}{\lambda_0}$ (in which, $(\overrightarrow{\zeta^2})^{1/2}$ is the root-mean-square surface height, λ_0 is the wave length of a wave component which has the spectrum peak frequency) and the effective depth (n is the water depth). For deep water and low wind speed situation, $\mu(n) \ll 1$, thus, equation (8) is simplified to

$$\theta(n) = \frac{rn^2}{g + c_u n} \tag{10}$$

Substituting equation (10) in equation (3) we get

$$c(n) = \frac{g}{n} + c_u \tag{11}$$

Clearly, under low speed conditions, except for the added term c_u produced by wind drift, the phase velocity of the wave component fits to the linear dispersion relation equation. For shallow water and high wind speed, $\mu(n) \gg 1$, thus, equation (8) is simplified to

$$\theta(n) = \frac{rn}{c_N + c_u} \tag{13}$$
$$[\text{sic}]$$

75

Substituting this equation in equation (3), we have

$$c(n) = c_N + c_u \tag{14}$$

Clearly, under these conditions, the wave field is non-dispersive, and the wave components are propagated as constant velocity.

The above are two extreme situations. The others are ordinary situations displayed in Figures 2 and 3. The wave component phase velocity relative to changes in frequency takes a form between equation (11) and equation (12) [as published]. The results measured by Ramamonjiarisoa under medium wind speed appears to be one type belonging to the above discussed ordinary situation.

V. Conclusion

The above measurement results and the theoretical interpretation show that the wind-wave component's dispersion relation is rather sensitive to nonlinearity of the wave field. In shallow water and at low wind speed, the wave field has lower nonlinearity, the wave component's phase velocity basically obeys the linear dispersion relation (except for the influence of wind drift). As wind speed increases, the wave surface becomes steeper, the wave field's non-linearity becomes higher, the wave component phase velocity at the higher frequency deviates from the linear dispersion relation. In shallow water at higher wind speeds, the wave field has powerful nonlinearity. At such times, non-dispersive waves play the dominant role, and thus the wave field is basically non-dispersive, and all the wave components are propagated at nearly the same velocity.

The above measurement results and theoretical analysis also show that when computing wind-wave wave component phase velocity, drift produced by the wind should be taken into consideration, at least this should be the case for laboratory wind-waves.

REFERENCES

1. Ramamonjiarisoa, A., 1974: CONTRIBUTION A L'ETUDE DE LA STRUCTURE STATISTIQUE ET DES MECHANISMES DE GENERATION DES VAGUES DE VENT. Thesis de Doctorat d'etat. Inst. de Mec. Statist. de la Turb., Univ. de Provence, France.

2. Yefimov, V.V., Yu. P. Solov'yev and G.N. Khristoforov, 1972: OBSERVA-TIONAL DETERMINATION OF THE PHASE VELOCITIES OF SPECTRAL COMPONENTS OF WIND WAVES, Izv. Atmos. Oceanic Phys., 8, 435-446.

3. Ramamonjiarisoa, A. and E. Mollo-Christensen, 1979: MODULATION CHARAC-TERISTICS OF SEA SURFACE WAVES, J. Geophys. Res., 84, 7769-7775.

4. Huang, N.E., 1981: COMMENT ON MODULATION CHARACTERISTICS OF SEA SURFACE WAVES' TU A. RAMAMONJIARISOA AND E. MOLLO-CHRISTENSEN, J. Geophys. Res., 86, 2073-2075.

5. Macuda, A., Y.Y. Kuo, and H. Mitsuyasu, 1979: ON THE DISPERSION RELATION OF RANDOM GRAVITY WAVES, PART 1, THEORETICAL FRAMEWORK, J. Fluid Mech., 92, 717-730.

6. Dudis, J.J., 1981: INTERPRETATION OF PHASE VELOCITY MEASUREMENTS OF WIND-GENERATED SURFACE WAVES, J. Fluid Mech., 113, 241-249.

7. Xu Delun, Joe Wang, and Jin Wu, 1984: EQUILIBRIUM SPECTRUM OF WIND-GENERATED WAVES FROM DEEP TO SHALLOW WATER, Technical Report No JW-24, Air-Sea Interaction Laboratory, College of Marine Studies, University of Delaware.

8226/6091
CSO: 4008/1058

CHINESE LANGUAGE MICROCOMPUTER DESCRIBED

[Article by Chen Shiming [7115 0013 6900], Academy of Sciences, Guangdong: "The Characteristics and Use of the LX-80A Chinese Language Computer"]

[Text] The LX-80A associative Chinese character graphics microcomputer system (hereafter, Chinese language computer) was successfully developed by the Institute of Computing Technology of the Chinese Academy of Sciences, and is currently in production by units such as the experimental factory of the Guangdong Academy of Sciences. Its characteristics and methods of use are as follows:

Multiple Chinese Character Input Methods

Chinese character input for the LX-80A Chinese language computer is easy to learn and is broadly adaptable.

1. The "interactive" Chinese character input method.

This method is coded according to the stroke shapes of Chinese characters, so it is also called "stroke coded." There are 40,000-50,000 Chinese characters, more than 6,000 of which are in common use, and stroke coding can classify the stroke components of the character radical into 26 basic shapes. There are 6 basic strokes (一丨、丿乚フ) , 7 common radicals (土、木、氵、廾、人、扌、口),

12 stroke combinations, and 1 independent character-stroke shape. The code of each stroke uses the keyboard position of an English letter, and the name of each stroke uses the Chinese character command that may be seen at the left of Figure 1. For example, the stroke shape "廾" is called "grass and the corresponding key is the letter "Q."
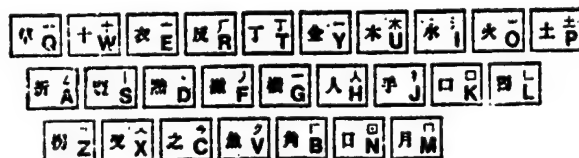

Figure 1

The input method used by the LX-80A system is called "visual keyboard input."
At the bottom of the screen of the display device there is a three line prompt
area, where after power up, the 26 stroke shapes in Figure 1 and their
corresponding English letters are all displayed in the prompt lines. To enter
a particular stroke, just press the corresponding letter key. To enter the
"grass" radical, press "Q."

Using stroke shape coding to enter Chinese characters is largely the same as
our habits in writing them. The rule in writing out strokes is that it
proceeds from left to right, from top to bottom, from the outside to the
inside, etc. The stroke shape coding method of the LX-80A system uses
the first stroke and the second stroke. Those characters that use only the
first stroke may then be found, but the majority of characters will need the
second stroke shape before they can be found. For some words that are not
divisible, called independent words, as for example "户" , after the first stroke
shape press the 'L' key (the independent word key), which will then locate
the word. The distinction between the first stroke shape and the second is
indicated by the letter appearing at the left in the prompt area. We will now
use the entry of the 5 characters of "Chinese Academy of Sciences" 中国科学院

as an example to illustrate this method. The first stroke shape of these
5 characters is as in the written example in Figure 2.

中国科学院

Figure 2.

The first stroke of 'zhong' is '1,' so push the 'S' key. At this time,
26 characters having '1' as their first stroke will appear in the prompt area
of the screen (the 26 characters in the prompt area have differing stroke counts
and will not necessarily be the same each time), and when the character 'zhong'
appears in the position of the letter 'M,' press lower case 'M' to enter the
character 'zhong' in the text. Similarly, for the character 'guo' press 'N,'
then enter the lower case 'p,' for the character 'ke' press 'F,' for 'xue'
press 'D,' and for 'yuan' press 'B,' after which you must also press 'D' for
the second stroke shape before 'yuan' will appear on the screen.

Because we are using 26 stroke shapes to find all Chinese characters, this
requires a greater representation to include all stroke shapes in Chinese
characters. For example, the stroke shape "厂" represents both "阝" and also "厂" ,
"巨"、"局"、"尽"etc., for the left part of these characters all have the shape of "厂".

When using stroke shape coding to enter the character radicals or the radical
components, the prompt area of the computer screen will display the Chinese
characters one needs, and will tell you which key should be pressed next to
enter a character. This method is called "interactive" entry.

2. The romanization entry method.

Similarly to the "interactive" entry method, use the romanization key for the LX-80A system to accomplish the task of character entry by pressing the keys that represent the initials and finals and the corresponding material in the prompt area of the screen.

3. The "arbitrary selection coding" entry method.

As of this moment, there are hundreds of different Chinese character input methods, and the design of the LX-80A has taken into consideration coding schemes with which the user may already be familiar, as for example the tele-graphic code, the Cang Jie code, or the four-corner code, and the user may select one among them as an input method for the LX-80A system. After entering the telegraphic code, press the "arbitrary selection" function key and the computer will be placed in the "arbitrary selection coding" state (i.e., telegraphic code). At this time, characters may be entered with telegraphic codes.

The LX-80A system provides users with software for "automatic generation of an arbitrary selection coded dictionary" that will allow the user to use the coding method with which he is most familiar or to change to a new coding scheme designed by the user.

4. The "international index code" entry method.

Chinese character international index codes are four-digit hexadecimal codes, used, for example, by sending a "30AE" to represent the character for "to love." The transmission steps are as follow: press the "international index code" function key and the computer will then be placed in the international code status. Then, enter a "30AE" and press the space bar. The computer will display the character for "to love." If more than 4 digits are entered, then the code will automatically be discarded, only the last four codes being accepted. With international coding, Japanese and Russian may also be entered.

The four entry methods just described are controlled by corresponding function keys, and methods may be changed at any time for greater convenience.

Independent Chinese Character Associative Functions

There is an associative dictionary in the LX-80A system that contains tens of thousands of common words and phrases. As each Chinese character is entered, the computer guesses the next possible word based on the dictionary, and then displays this word on the screen prompt area. The operator may then directly choose this word. A character will bring up a group of characters (26), which is very like the human associative function. In this way, and by interlocking associations, a large number of words, phrases, and even whole sentences can be generated. The partial associative structure for the character 'zhong' in Figure 3 is shown with arrows indicating the directions.
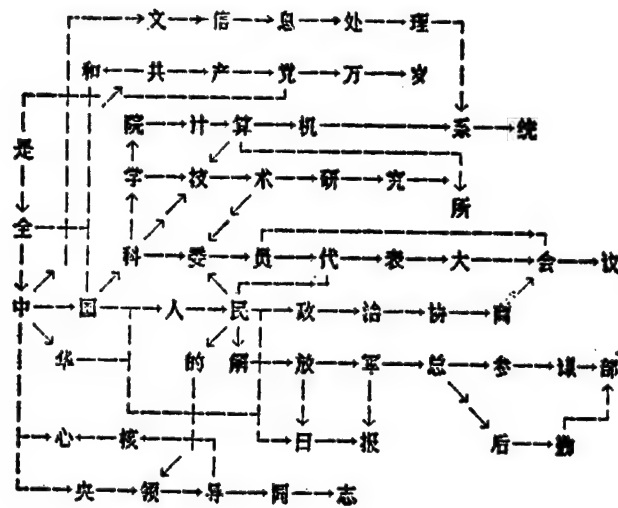
Figure 3

Use of the associative function is very easy and may be divided into the associations with "characters" and the associations with "words."

1.   Associations with "characters."

This associative function is controlled by function key F7. Pressing this key will present the word "association" in the prompt area, indicating that the computer has entered the associative state. If the character "zhong" is entered, 26 characters like "hua" and "guo" will appear in the prompt area. After choosing "guo," 26 words like "qi," "jia," and "ke" will appear in the prompt area. In this way, entry of the five characters "Zhongguo Kexue Yuan" ["Chinese Academy of Sciences"] can be by the associative method and need not be entered by the character at a time method described earlier.

2.   Associations with "words."

This is controlled by function key F9, and if after entering the character 'zhong' F9 is pressed again, many words and phrases associated with the character 'zhong' will appear in the prompt area, as for example, "leading comrades of the Central Committee," "Chinese Academy of Sciences," etc., and when there are many associated words and phrases, they may be displayed by repeated pressing of F9. If a particular phrase is to be entered, the key corresponding to the final character in the associated phrase may be pressed and the entire word or phrase will be entered into the computer. The longer the sentences are, the higher the efficiency.

There is associative function support for each of the character input methods described above, which allows character input speed to reach an average of 1.5 key presses per character.

The First Chinese Character Command System

Command operation of the LX-80A system itself is now by Chinese characters.
Twenty-six Chinese character commands have been burned onto a 64 kb EPROM,
and upon system reset, the 26 character commands are all displayed in the prompt
area by their functions. As shown in Figure 4, if the user wishes to see the
file directory of the current disk, he may press 'Q,' and the screen will then
immediately display the file directory and will also tell the user the size of
each file. If one wishes to know which operations commands are represented by
the English letter keys, press 'W' and the screen will display the meaning of
each command.

The LX-80A is a multi-function, stand-alone Chinese language computer system
having 576 kb of RAM and two floppy disk drives, with a 24 pin printer. It
can be used for document processing, storage and display, and for printing.
It is equipped with a standard interface (RS-232) and may be connected with a
variety of host computers, which makes the LX-80A a powerful Chinese language
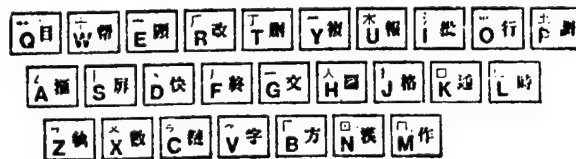terminal.

Figure 4

12586/8309
CSO: 4008/1076

82

APPLIED SCIENCES

INVESTIGATION OF UNDULATOR FOR HEFEI 800 MEV ELECTRON STORAGE RING

[Article by Chen Zihcheng [7115 1807 6134] and Liu Jian-yang [0491 1696 2254],
China University of Science and Technology, and Xu Jianming [1776 1696 6900],
Institute of High Energy Physics, Chinese Academy of Sciences: "The Investigation of an Undulator for the Hefei 800 MeV Electron Storage Ring"; paper received on 11 March 1985]

[Text] Abstract: A permanent magnet undulator for the Hefei 800 MeV electron storage ring is now under construction. This paper introduces undulator radiation characteristics and magnet design considerations and reports on the design, development, and magnetic field measurement results of a 10 period hybrid undulator model.

I. Introduction

An undulator is a periodic magnetic device which, when inserted into the electron ring's linear section, can supply quasi-monochromatic synchronous radiation light of greater brightness than the radiation produced by a wanzhuan [1737 6567 turning?] magnet, and thus becomes an important insertion component of storage rings. Its technical reliability has been verified by successful experiments by many laboratories abroad.[1] The undulator has the following three primary features: 1) The special structure of the undulator magnet makes the ring's electron beam not produce net deflection or shifting and does not have a serious influence on the electron beam movement; 2) In the wanzhuan magnet, the electron beam radiates a continuous and smooth light spectrum, but in the undulator, the interference effect of the radiation suppresses the radiation light in some wavelengths, thus in specific wavelengths it is intensified, and the radiation is concentrated within a narrow wavelength interval, and the light spectrum obtained is several narrow quasi-monochronomatic light peaks; 3) The radiation focuses within a very small space solid angle along the axis, and has a high spatial brightness and collimation, which reduces the heat given off by the beam ray components, and radiation power can be more effectively utilized.

When high magnetic energy rare earth metal permanent magnet material is used for the undulator magnet, an excitation current is not required, there is no

power loss, manufacturing expenses can be saved, and the magnetic period length is greatly reduced, to obtain short radiation wave lengths and full utilization of the limited storage ring linear section space. Permanent magnet undulators do not require other added equipment which greatly simplifies the complexity of building the magnet.[2]

This paper introduces the magnet design of the Hefei 800MeV electron storage ring's undulator and the mechanical structure of the undulator model and the magnetic field measurement results.

II. Design of the Undulator Magnet

A hybrid magnetic path design was adopted for the Hefei storage ring's undulator magnet.[3] The hybrid is an alternating arrangement of samarium cobalt ($SmCo_5$) permanent magnet and soft iron, which mix to form the magnetic path (Figure 1). The permanent magnet plays the role of the "source" which excites the magnetic flux, and the magnet's magnetized direction along the axis changes alternately by 180°, the soft iron is used as a magnetic pole, on the central plane of the magnetic a sinusoidal period magnetic field will be produced, i.e., $B_y = B_0 \sin 2\pi \frac{s}{\lambda_u}$, in which B_0 is the peak magnetic field, λ_u is the undulator magnetic period length, s is the length along the axis. The hybrid magnet has the following two beneficial features: 1) The hybrid magnet's field distribution is mainly derived from the surface shape of the mannetic pole, the homogeneity of magnetic material performance need not be strictly demanded; 2) each peak magnetic field which corresponds to the magnetic pole can be fine tuned using a magnet tuning screw, thus higher uniformity of peak field can be obtained.
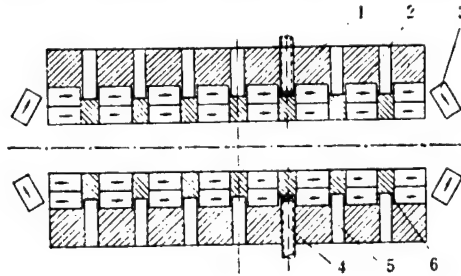

Figure 1.   Diagram of Hybrid Undulator

Key:
1. Support
2. Permanent magnet
3. Rotating magnetic pole
4. Magnet tuning screw
5. Screw-hole
6. Soft iron magnetic pole

We used a limited differential calculation program to design the magnetic path, and at the same time carried out an analysis of the hybrid magnet's field distribution.[4] The fundamental wave of the peak magnetic field can be expressed as

$$B_0 = \frac{4B_r}{\pi} \left\{ \left(\frac{4\pi M_i}{B_r} \right) \left[1 - \frac{\lambda_u}{2\pi h_1} \left(1 - e^{-\frac{2\pi h_1}{\lambda_u}} \right) \right] \sin \frac{\pi l_1}{\lambda_u} \right.$$
$$\left. + \left(1 - e^{-\frac{2\pi h_2}{\lambda_u}} \right) \sin \frac{\pi l_2}{\lambda_u} \right\} e^{-\pi g/\lambda_u} \tag{1}$$

84

in which B_r is the intensity of the permanent magnet's residual magnetism, h_1, h_2, and l_1, and l_2 are the height and length of the soft iron magnetic pole and the permanent magnet, respectively, in which

$$h_1 = \frac{2}{3} h_2,$$

$$\left(\frac{4\pi M_i}{B_r}\right) = \frac{\pi h_1 l_2}{K_f \pi l_1 l_2 / 2 + K_r \lambda_u h_1 th(\pi g / \lambda_u)}$$

K_3 and K_r are the leakage coefficient and the magnetic resistance coefficient.

Depending on the undulator radiation characteristics, when K*=1.2, the first harmonic of the radiation light has the highest brightness, and the second, and fifth harmonic also can obtain higher brightness. The undulator radiation brightness and the spectral line width are determined, to a considerable degree, by the magnetic period number, i.e., $\frac{d^2 I}{d\omega / \omega d\Omega} \propto N^2$, $\frac{\Delta\lambda}{\lambda} \propto \frac{1}{N}$. The Hefei storage ring undulator was designed on this basis. When $=4.8$cm, $l_1 = \lambda u / 6$, $l_2 = \lambda u / 3$, and $h_2 = 2.7$cm, the undulator path is more ideal and can fully utilize the magnetic performance of the magnet. When $g / \lambda u = 0.5$, the peak magnetic field can reach $B_0 = 0.29$T, correspondingly, K=1.3, the magnetic field's third harmonic component is smaller than 3.5 percent, and thus is a sinusoidal distribution which is a very good approximation. The linear section free space left in the design of the Hefei storage ring for the undulator permits the undulator length to be 2.1m. At least 40 magnet periods can be arranged in such a length, and their radiation characteristics are given in Table 1.

The minimum useful gap of the undulator magnet is limited by the beam vacuum pipe's vertical aperture. After the undulator has been inserted into the storage ring there should be a guarantee that the storage beam's life will not be influenced to obtain a beam of sufficient length and to reduce beam loss, the undulator gap should at least satisfy

$$g > 14\sigma_y \tag{2}$$

σ_y is the mean-square-root half-height of the beam at the magnet outlet, taking into account the possible closed-track distortion of the beam, it is necessary to add a certain safety coefficient. Assuming an average vertical distortion $\langle \delta y_c \rangle \simeq 6$mm , we designed vacuum tube wall thickness and installation gap, taking the minimum gap g=2.4cm.

In the vertical direction, the undulator is symmetrical relative to the central plane of the path, relative to the central point, the magnet is roughly symmetrical, and at the central point there is a maximum magnetic field value. After the electron beam goes through the undulator, it cannot have net path shift or deflection, thus is demands that there may be any net dipolar magnetic field. To compensate for the influence of a new dipolar field, it is necessary to install adjustable magnetic poles at both ends of the magnet and by adjusting

---

*K is the undulator's magnetic defelction parameter, i.e., K=0.934B_0(T)λu (cm).

marginal magnetic fields make the integral along the axis zero, i.e., $\int Bds=0$. But in fact, it is not easy to tune $\int Bds=0$, thus we provided a restriction $\int Bds \leqslant 150Gs-cm$ to make the closed track distortion caused by the net dipolar field unimportant.

When the electron beam goes through the undulator, the vertical direction movement transform matrix is

$$
M_y = \begin{bmatrix} \cos K_{eq}s & \dfrac{1}{K_{eq}} \sin K_{eq}s \\[2mm] -K_{eq} \sin K_{eq}s & \cos K_{eq}s \end{bmatrix} \tag{3}
$$

in which $K_{eq} = \dfrac{1}{\sqrt{2}} \dfrac{K}{\gamma} P_0,\ P_0 = \dfrac{2\pi}{\lambda_u}.$. Thus we bring about a change in the storage ring symmetry and work point. Through matrix operations, we can provide the vertical direction movement's phase shift, and oscillation number and the change of the partial βy function as

$$
\begin{cases}
\Delta\mu_y = -\dfrac{\beta_y K_{eq}^2 L}{2}\left(1 - \dfrac{L^2}{4\beta_y^2}\right) \\[3mm]
\Delta\nu_y = \Delta\mu_y/2\pi \\[3mm]
\Delta\beta_y/\beta_{y0} = \left(1 + \dfrac{L^2}{4\beta_y^2}\right)\sin\mu_y/(\sin\mu_y + \Delta\mu_y \cos\mu_y) - 1
\end{cases} \tag{4}
$$

The working point of the storage ring's vertical direction movement is $V^y=2.58$, on the basis of the storage ring and undulator parameters given previously, we can obtain $\Delta\mu_y = 0.0152,\ \Delta\nu_y = 0.0024,\ \Delta\beta_y/\beta_y = 0.05.$ Change in the working point is within the permitted range, and by regulating other focusing parameters, the symmetry of the storage ring can be bascially restored to its original state.

The quadruple effect of the horizontal component B_x will cause a correction in the storage ring beam optics, but for weak field undulators and higher energy electron beams, the influence of the magnetic field's quadruple effect is very small. If the maximum relative error of the magnetic field is $\dfrac{\Delta B}{B_0} = 5\%$, then when K=1.2, the path shift of the beam's lateral movement horizontally and the increase in beam angular scattering are respectively $\Delta x = 2.7 \times 10^{-3}mm$, and $\Delta x' = 2.8 \times 10^{-3}mrad$, and the disturbance of the beam is very small.

The basic parameters of the Hefei 800 MeV electron storage ring undulator insertion section center are as follows (when the ring's coupling coefficient is o.1):

Beam emmissivity	$\varepsilon_x = 0.1215mm\text{-}mrad$	$\varepsilon_y = 0.0122mm\text{-}mrad$
amplitude function	$\beta_x = 21.5481m$	$\beta_y = 3.4147m$
beam lateral dimensions	$\sigma_x = 1.6184mm$	$\sigma_y = 0.2037mm$
beam scatter angle	$\sigma_x' = 0.0751mrad$	$\sigma_y' = 0.0597mrad.$

Thus, a 40 period undulator placed in the insertion section's radiation brightness will be 10^3 hihger than the wanzhuan magnet. Figure shows the radiation spectrum in the undulator and the wanzhuan magnet.
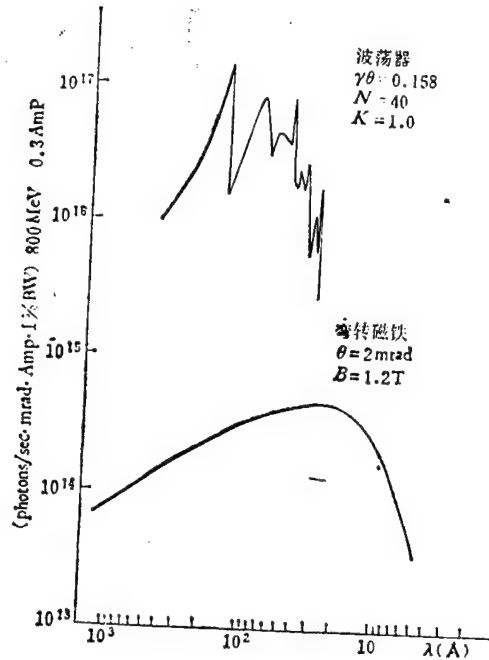
86

Figure 2.   Radiation Spectrum of Undulator and Wanzhuan Magnet

Tuning the intensity of the undulator's magnetic field can tune the radiation wave length.   When the magnetic parameter K is tuned between 0.1 and 0.2, by using first, third, and fifth harmonics, the range of the useable operating wavelength is 20-168Å.   Table 1 gives the calculated results of several groups of characteristic parameters of the Hefei synchronous radiation device using a 50 period undulator (γ=1565.56, 1=0.3A, λ_u =4.8cm, N=40).

Table 1.

magnet parameter K	harmonic number k	harmonic wave-length $\lambda(Å)$	natural line width $\frac{\Delta\lambda}{\lambda}(\%)$	radiation brightness (Phs/sec, mrad^2, A, 1%BW)	total radiation (Watts)
0.4	1	106	2.5	5.1×10^{16}	
	3	35	0.83	8.6×10^{14}	2
	5	21	0.5	1.0×10^{14}	
0.8	1	129	2.5	1.3×10^{17}	
	3	43	0.83	2.4×10^{16}	8
	5	25	0.5	2.9×10^{15}	
1.2	1	168	2.5	1.6×10^{17}	
	3	56	0.83	8.4×10^{16}	18
	5	34	0.5	3.0×10^{16}	

III. Undulator Model and Magnetic Field Measurements

The undulator magnet model was developed to build a 2.1m, 40 period undulator with the aim of gaining some experience in the magnet design, mechanical structure and processing technology, to provide measurement parameters of magnet performance. The model used the magnetic path parameters given above, but the overall length was reduced which diminished the use of a permanent magnet. Table 2 gives the basic parameters of this model.

Table 2.

Material	$SmCo_5$ soft iron
Permanent magnet residual magnetic intensity B_r	0.9T
Magnet period length λ_μ	4.8cm
Permanent magnet specifications	1.6cm (magnetized direction)x7.5cmx 1.8cm
Soft iron magnetic pole specifications	0.8cmx7.5cmx1.2cm
Magnetic period number N	10
Magnetic pole number	10 pairs
Overall model length L	0.6m
Adjustable gap range g	2.4-6.0cm
Peak magnetic field B_o	0.22T(g=2.4cm)

For ease of loading and use, the undulator model was designed in a "C" shape, the structure primarily made up of upper and lower cope plates and framework, the permanent magnet and soft iron magnetic poles are cemented to an aluminum "U" shaped holding plate which is screwed to the cope plate, so the upper and lower magnetic poles are facing each other. Three independent manual adjustment systems are used to adjust the gap and the rotating mangetic poles at the ends. When adjusting the gap, the upper and lower cope plates moved relative to the central plane, when the gap is large, the magnetic field is weak, when the gap is small, the magnetic field is strong. The rotating magnetic poles can be adjusted to any angle to facilitate adjusting the peripheral magnetic fields to make the magnetic field's axial integral $\int Bds=o$. At the outer edge there is a magnetic screen intended to eliminate the magnet's influence on other components, and to make the peripheral magnetic field rapidly drop to zero. At the other end there is also a guide rod to reduce wobbling when the cope plate is being adjusted.
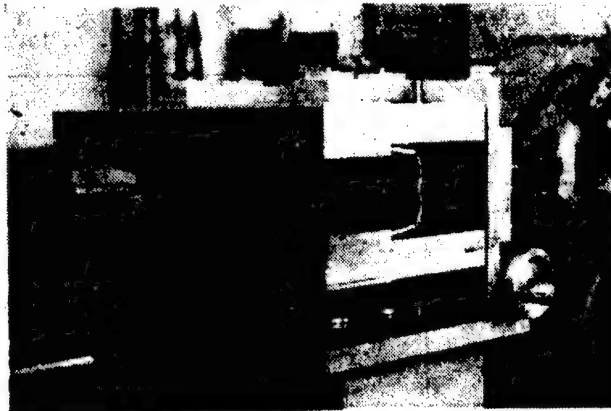

Figure 3. Photograph of Undulator Model

Each period of the model's magnet requires 16 permanent magnets, including the rotating magnetic poles at the ends, so a total of 168 permanent magnets were used. The permanent magnet performance parameters are $B_r = 9065 \pm 288Gs$, $H_c = 7544 \pm 170e$, the magnet's energy accumulation [nengji 5174 4480] $<BH>_m \simeq 18MOeGs$.

The magnet was measured by a huoerpian [7202 1422 3651] (Ge) fixed to an x-y-z three dimensional support, the huoerpian's sensitive area was $1.5 \times 4mm^2$, the temperature coefficient was $5 \times 10^{-4}/°C$, at the time of the measurement, the room temperature was held to $26 \pm 0.5°C$. The overall measurement precision was 3×10^{-3}. Measurement step length was 2mm. The magnetic field measurements are summarized below (for measurements see Table 3):

1) On the central plane of the undulator, the distribution of the vertical field component axially is sinusoidal. Figure 4 gives the magnetic field distribution when g=2.4cm and a period field distribution for different gaps, the third harmonic wave component of the magnetic field is smaller than 0.5 percent, much smaller than the anticipated harmonic wave. Because of differences in performance of the magnets and processing and installation, at the time of the initial measurements, there was a definite fluctuation of the peak magnetic field, but after using the magnet adjusting screw, the average of the peak field improved greatly with an average better than $\frac{1}{NK^2}$.

2) The magnets at the end can be adjusted to any angle, to make $\int Bds = 0$. The angle adjustment changes with the size of the gap. When g=2.4cm, the adjustable range of end rotating magnetic poles within the 90° angle range is 1900Gs-cm. The axial integral of the vertical field component and horizontal field component were measured at different gaps, and the results of the measurements were less than 150Gs-cm, satisfying design demands.
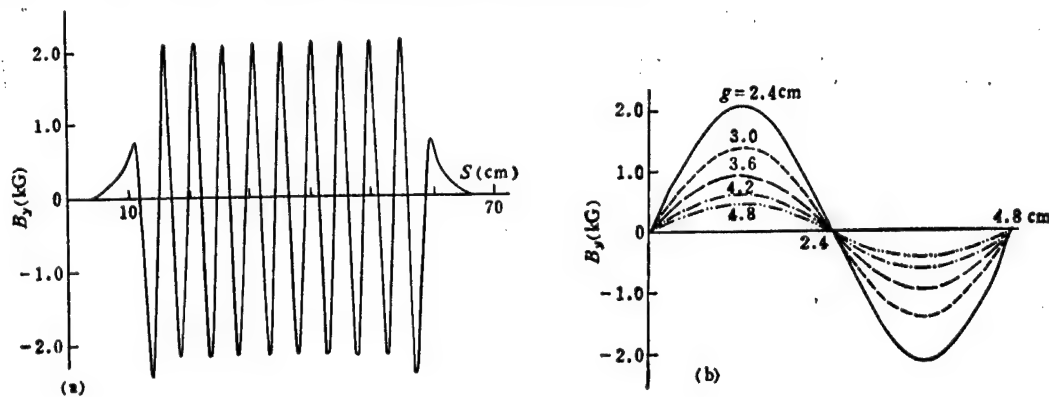

Figure 4. Magnetic Field Distribution Curves

Key:
    (a) Magnetif field axial distribution when g=2.4cm
    (b) Magnetic field distribution of one period at different gaps

3) For the vertical field component of sinusoidal distribution along the axis, where the value was at the maximum, the average area was small, thus the average area measured at the point of peak field can characterize the average

of the entire magnet. We measured the lateral field area of the deviating ±1cm from the beam axis on the central plane at different gaps, and gave the relative deviation relative to the axial peak magnetic field. It can be seen from the measurement results that the deviation is far smaller than the ±5% demanded by beam optics.

Gap (cm)	Average Peak magnetic (Gs)	Peak field average (Gs)	Vertical field integral (Gs-cm)	Horizontal field integral (Gs-cm)	Relative magnetic field deviation of ±1cm good field area
2.4	2179	39	4.8	−93.4	0.2
3.0	1466	42	−19.9	−71.4	0.29
3.6	994	41	−78.1	−67.5	0.38
4.2	672	41	−67.8	−51.0	0.43
4.8	465	40	51.0	−70.1	0.58

The mechanical structure of this model is very simple and the adjusting system flexibility is stable. The measured fields of the model's magnetic path design achieved anticipated demands.

In the area of mixed undulator field shape analysis we had beneficial discussions with Comrades Liu Maosan [0491 5399 0005] and Chen Renhuai [7115 0088 2037] of the High Energy Institute.

In the area of magnetic field measurement we were greatly aided by Comrade Yan Heping [7051 0735 1627], and here we express our gratitude to all of them.

References

1. G. Brown, K. Halbach, J. Harrio, and H. Winick, N.I.M. 208 (1983) 65.

2. M.W. Pool and R.P. Walker, PERIODIC MAGNETS FOR UNDULATORS AND FREE ELECTRON LASER, the International Conference on Magnet Technology, 1981.

3. E. Hoyer et al., IEEE TRANS., NS-30(1983) 3118.

4. Liu Maosan [0491 5399 0005], et al., PROCEEDINGS OF THE SECOND CHINA-JAPAN JOINT SYMPOSIUM ON ACCELERATORS FOR NUCLEAR SCIENCE AND THEIR APPLICATIONS, 265, Institute of Modern Physics, 1983.

APPLIED SCIENCES

SQUARE-LOOP ANTENNA FOR SHIPBOARD USE DESCRIBED

[Article by Wang Guoqiang [3769 0948 1730] and Huang Ruican [7806 3843 3503]:
"A Half-Wave Square-Loop Antenna for Ship Use"]

[Text] I. Overview

Ships navigating on the ocean are typical moving bodies. Therefore, in the VHF
and UHF bands, shipboard television reception antennas have to be omnidirectional
and have high gain along the horizontal. At present, shipboard omnidirectional
antennas in regular use are orthogonal half-wave antennas and loop antennas.
This paper proposes a half-wave square-loop antenna, which in comparison with
orthogonal half-wave antennas has higher gain when the number of elements is
the same. What we mean by a half-wave square-loop antenna is where each side
of a square-loop antenna is equal to a half-wavelength. The principle is as
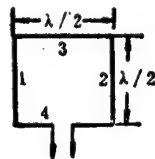shown in Figure 1.
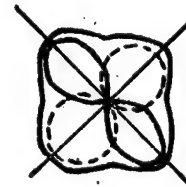

Figure 1. Square-loop Antenna Schematic   Figure 2. Directivity Chart

On the surface of the antenna, when the signal wave comes around from the vertical
at side 1 (or 2), sides 1 and 2 then form a half-wave oscillating two-element
antenna array. If the signal wave is turned around from the vertical in the
direction of side 3 (or 4), then sides 3 and 4 form a half-wave oscillating
two-element antenna array. Therefore, the gain from a half-wavelength square-
loop antenna will be greater than an ordinary orthogonal half-wave oscillating
omnidirectional antenna. Its omnidirectionality is fundamentally the same.

91

II. Directional Coefficient and Directivity Charts

As shown by the square-loop antenna in Figure 1 and by the preceding explanation, it is not hard to see that when this antenna is placed at the horizontal it is equivalent to two groups of orthogonal two-element arrays in the horizontal plane. The array elements are half-wave oscillators, and the distance between the two-element arrays is d = λ/2. Therefore, the directivity coefficient of this kind of antenna may be conveniently written as: [Zhang Fangying [1728 2455 5391]: "Antennas and Feeder Equipment," (Beijing: Beijing Kexue Joaiyu, 1962), p 431.]

$$F(\theta) = \left[\frac{\cos\left(\frac{\pi}{2}\cos\theta\right)}{\sin\theta} \cdot \sin\left(\frac{\pi}{2}\sin\theta\right) + \frac{\cos\left(\frac{\pi}{2}\sin\theta\right)}{\cos\theta} \cdot \sin\left(\frac{\pi}{2}\cos\theta\right) \right]$$

The directivity chart produced by $F(\theta)$ is shown in Figure 2. The dotted lines represent the directivity chart for sides 1, 2 of the square-loop antenna; the thin solid line is the directivity chart for sides 3, 4 of the square-loop antenna; the thick solid line is the composite directivity chart.

1. Testing the directivity chart.

When the square-loop antenna is placed at the horizontal, side 3 in Figure 1 is aligned as a radiating antenna, and this is taken as zero, then the test data is as listed in Table 1. See Figure 3 for a horizontal directivity chart as described in Table 1.

When the square-loop antenna is placed vertically, and the direction of the transmission of the signal wave on the vertical plane is zero, at this time the received signal is strongest, the test data being as in Table 2. See Figure 4 for a vertical directivity chart as described by Table 2.

Table 1

Deflection angle (degrees)	0	15	30	45	60	75	90	105	120	135	150	165	180
Maximum reading (grid)	60	57	48	36	48	57	60	57	48	33	27	48	51
Normalized value	1	0.95	0.80	0.60	0.80	0.95	1	0.95	0.80	0.55	0.45	0.80	0.85

Table 2

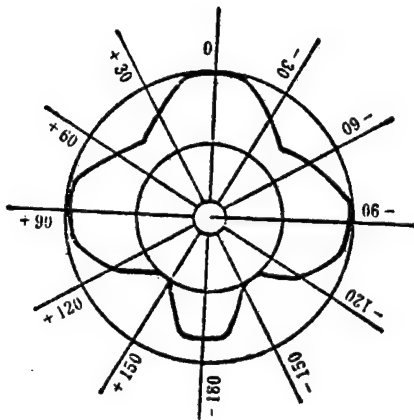| Deflection angle (degrees)	0	15	30	45	60	75	90	105	120	135	150	165	180
Maximum reading (grid)	0	15	30	48	69	70.5	72	70.5	69	48	30	15	0
Normalized value	0	0.20	0.41	0.66	0.95	0.97	1	0.97	0.95	0.66	0.41	0.20	0

92

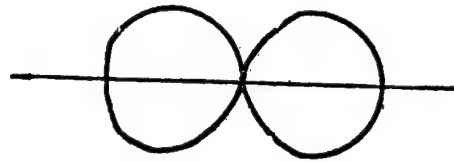Figure 3. Horizontal Directivity Chart
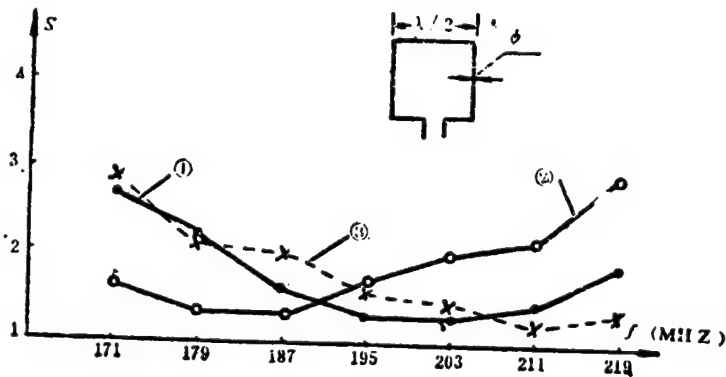

Figure 4. Vertical Directivity Chart

Figure 5. Relation Curves for Standing
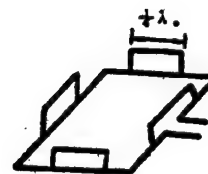Wave Ratios and Frequencies

Figure 6. Diagram for Expanding
Bandwidth

2. Testing frequency characteristics.

For these tests we selected channels 6 through 12 in the VHF band. The
frequency characteristics of the half-wave square-loop antenna were indicated
through tests of the standing wave ratio. The antenna input impedance was
300 ohms, and the antenna input terminal was connected through a broad band
impedance transformer and 75 ohm coaxial cable.

Using a square-loop antenna made of copper wire of differing diameters, the relational curve of the standing wave ration S and the frequency f is as shown in Figure 5.

Curve 1 shows the design frequency f_o=195 MHz of the square-loop antenna, where side $\alpha = \lambda/2$=770 mm and the diameter of the antenna is ϕ = 4.4 mm.

Curve 2 shows the design frequency f_o=195 MHz of the square-loop antenna, where side $\alpha = \lambda/2$=770 mm and the diameter of the antenna is ϕ =1.5 mm.

Curve 3 shows the design frequency f_o=203 MHz of the square-loop antenna, where side $\alpha = \lambda/2$=740 mm and the diameter of the antenna is ϕ =8 mm.

III.   Discussion

1.   There is a definite difference between the tested horizontal directivity charts and the horizontal directivity charts by theoretical analysis.   The direction with the greatest dip just happens to be the direction where the signal is aligned with the side that meets the feeder line.   This shows that for the side that connects with the feeder line, reception efficiency is not as good as for the sides without the feeder line.   In two tiered applications of square-loop antennas, this condition should be in mind.

2.   It can be seen from Figure 5 that the higher the frequency of the square-loop antenna application, the thicker should be the diameter of the material used. The curve 2 in Figure 5 shows that when the diameter ϕ =1.5 mm, the low point (179-187 MHz) standing wave ratio of the test frequency is smallest.   Curve 1 then shows that when the diameter ϕ =4 mm, square-loop antennas of equal dimensions will have the least standing wave ratio at the high end (195-211 MHz). Curve 3 shows that when the antenna diameter used is ϕ =8 mm, the practical frequency is even higher.

3. To further develop the working frequencies of the square-loop antenna, the method shown in Figure 6 may be used for adding shorter reception antennas.

12586/8309
CSO: 4008/1076

94

Electronics

THEORETICAL, EXPERIMENTAL STUDY OF CAVITIES IN TWT

[English abstract of article by Zhang Zhaohong [1728 2507 3163] and
Wu Hongshi [0702 7703 6684] of the Beijing Vacuum Electron Devices Research
Institute]

[Text]   An analysis of coupled cavities in TWT is presented.   The analysis
employs field equivalence principle in conjunction with Green's function
techniques.   The resulting operator equations are solved by the moment method.
The characteristics of the coupled cavities are expressed in terms of general-
ized admittance matrices which are functions both of frequency and dimensions
of the system.   The results of calculation performed with the aid of an elec-
tronic computer agree quite well with those of cold test measurements.   (Paper
received November 1984, finalized July 1985.)

References:

[1] H. J. Curnow: IEEE Trans., Vol. MTT-13, No. 9, pp. 671—675, Sept. 1965.

[2] R. I. Couier: BSTJ, Vol. 42, No. 7, pp. 1829—1861, 1963.

[3] M. A. Allen and G. S. Kino: IRE Trans, Vol. MTT-8, No. 5, pp 362~372, 1960.

[4] A. W. Scott and R. D. Wanselow: AD 275016, 1962.

[5] R. G. Catel: Proc. IEE, Vol. 130, pt. I, No. 2, pp. 67—72, 1983.

[6] J. Rodney and M. Vaughan: IEEE Trans., Vol. ED-22, No. 10, pp. 880—890, 1975.

[7] R. F. Harrington: Time Harmonic Electromagnetic Fields, McGraw-Hill, Ch. 3, New York, 1960.

[8] R. F. Harrington: Field Computation by Moment Method, Macmilan, New York, 1968.

[9] R. F. Harrington and J. R. Mautz: IEEE Trans., Vol. Ap-24, No. 9, pp. 870—873, 1976.

[10] E. G. Levchenko et al.: Radio Enginecring and Electron Physics, Vol. 14, No. 8, pp. 1260—1268, 1968.

[11] H. G. Kosmal and G. M. Branch: IEEE Trans., Vol. ED-20, No. 7, pp. 621—629, 1973.

[12] Chen-To Tai: Dyadic Green's Function in Electromagnetic Theory, PA: Scranton, Intext Educational
    Publishers, 1972.

[13] D. C. Stinson: Intermediate Mathematics of Electromagnetics, Prentice-Hall, Chapt. 5, 1976.

[14] M. Kisliuk: IEEE Trans., Vol. MTT-28, No. 8, pp 894—898, 1982.

[15] 张兆镗，微波管高频系统的测量，国防工业出版社，1982。

DYLMOS INTEGRATED CIRCUITS: HYBRID INTEGRATED CIRCUIT WITHOUT ISOLATION

[English abstract of article by Wang Shoujue [3769 1349 6030], Xia Yongwei [1115 3057 0251], Kong Lingkun [1313 0109 0961], Li Yuanjing [2621 6678 6975], and Ho Naimin [0149 0035 2494] of the Semiconductor Institute, Chinese Academy of Sciences, Beijing]

[Text]   A new hybrid integrated circuit without isolation, DYLMOSIC, has been developed.   By increasing and adjusting the technology, P channel MOS transistors and bipolar transistors with large β and small β value for the linear AND-OR gate in DYL are developed on the same wafer, based on the self-isolation characteristics among the linear AND-OR gates, the main logic unit in DYL, and MOSIC.   Using the hybrid integrated technology, an inverter unit is constructed by bipolar and MOS transistors on the same N type silicon wafer.   The benefits of DYLMOS hybrid integrated circuits are: simple and compatible technology with the linear AND-OR gate in DYL, high input and low output impedance and compatible level with DYL and TTL circuits.   (Paper received March 1985, finalized July 1985.)

References

〔1〕王守觉、孙祥义、王润梅；电子学报，No.2，pp. 43—51，1978.
〔2〕王守觉、魏书铭、郑洁；电子学报，No.1，pp.1—9，1980.
〔3〕王守觉、李致洁等；电子学报，No.5，pp. 9—16，1983.
〔4〕郑启伦、黄贯光；电子学报，No.6，pp.23—32，1981.
〔5〕王守觉、尹元茂、景士平；多元逻辑电路DYL时分式小型三用电话系统，半导体所研究报告。
〔6〕郑启伦等；MDA-016型电话系统研制报告，华南工学院研究报告，1984。
〔7〕王守觉、王宏道、李秀贤；多元逻辑电路万能函数发生器，半导体所研究报告。
〔8〕Lee Shi-chua; VLSI Design, Vol.5, pp. 98~100,1980.

INFLUENCE OF MISALIGNMENT OF ELECTRON LENSES ON IMAGE-QUALITY

[English abstract of article by Tong Linsu [4547 2651 1121] and Wu Changjin [0702 1603 3160] of the Nanjing Institute of Technology, Jiangsu]

[Text] The misalignment of the rotationally symmetrical electron optical system caused by manufacturing and assembling tolerance is an important limitation factor for further improving the image quality. The finite-difference method is first used to calculate the three-dimension field to analyze the problem of the misaligned electron lense. The influence of the misalignment of equidiameter cylinder bipotential immersion electron lense on image quality is given. Experimental tubes are also manufactured. It is shown that the theoretical computations are in good agreement with experimental values. (Paper received September 1984, finalized March 1985.)

References:

[1] O. Klemperer et al.: Electron Optics, Cambridge Press, 3rd ed., 1971.
[2] A. B. EL-Kareh et al.: Electron Beams, Lenses and Optics, Vol. I & II. Academic Press, 1970.
[3] V. K. Zworykin et al.: Electron Optics and the Electron Microscope, John Wiley, N. Y., 1945.
[4] 沈庆埃: 摄象管的理论基础, 科学出版社, 1984。-
[5] 西门纪业: 电子和离子光学原理及象差导论, 科学出版社, 1983。
[6] H. Moss et al.: Proc. Inst. Elec. Engrs (London) Part.Ⅲ, Vol, 97, p.277, 1950.
[7] D. M. Sutherland: IREE Australia, Vol. 27, p. 299, Nov. 1966.
[8] 西门纪业, 陈千寿: 电子学报, 第4期, p. 72, 1964.
[9] 西门纪业, 吴中和: 电子学报, 第3期, p.24, 1964.
[10] W. D. Riecke: Optik, Vol. 24, No.5, p.397, 1966/67.
[11] W. D. Riecke: Optik, Vol. 36, No.1, p.66, 1972.
[12] D. L. Say et al.: IEEE Trans., Vol. CE-21, No.1, p.57,1975.
[13] D. M. MacGregor: IEEE Trans., Vol. CE-29, No.3, p.318, 1983.
[14] B. A. Carre' et al.: Radio and Electronic Engineering, Vol.27, No.6, p.446, 1964.
[15] I. P. Csorba: RCA Rev., Vol. 31, p.534, 1970.
[16] I. P. Csorba: RCA Rev., Vol.33, p.393, 1972.

NEW METHOD OF MEASURING TWO-PORT DEVICES BY SIX-PORT REFLECTOMETER

[English abstract of article by Sun Jia [1327 4471] of the Chengdu Institute of Radio Engineering]

[Text] A new circuit is given for measuring scattering parameters of any two-port microwave network by means of a single six-port reflectometer. Based on the wave superposition theory and the theory of equivalent circuit, a new method of calibration and measurement is described. (Paper received July 1984, finalized July 1985.)

References:

[1] G.F. Engen: The six-port reflectometer: an alternative network analyzer, IEEE Trans., Vol. MTT-25, pp. 1075~1079, 1977.

[2] C.A. Hoer: Calibrating a six-port reflectometer with four impedance standards, NBS. Tech. Note 1004, 1978.

[3] S.H. Li, R.G. Bosisio: Calibration of multiport reflectometers by means of four open/short circuits, IEEE Trans., Vol MTT-30, pp. 1085—1090, 1982.

[4] G.F. Engen, C.A. Hoer: Thru-Reflect-Line': An improved technique for calibrating the dual sixport automatic network analyzer, IEEE Trans., Vol. MTT-27, pp. 987—992, 1979.

[5] 孙稼: 双六端口网络分析仪的校准与测量的新分析, 成都电讯工程学院学报, 第 3 期, 1984年.

[6] 孙稼: 双六端口网络分析仪校准与测量的一种新方法, 电子学报, Vol. 12, No. 6, 1984年.

[7] 李世鹤, R.G. Bosisio: 六端口反射仪的分析及最佳电路设计, 电子学报, Vol. 11, No. 2, 1983年.

[8] A.L. Cullen: Measurement of 2-port devices by a reflectometer system, IEE. Proc., Vol. 129. Pt. H, pp. 333~337, 1982.

[9] Sun Jia: New application of a single six-port reflectometer, Elec. Lett., Vol. 20, No. 22, pp920~922, 1984.

CONSTRAINED OPTIMIZATION DESIGN OF ELECTRON OPTICAL SYSTEM USING COMPLEX
METHOD

[English abstract of article by Gu Changxin [7357 2490 9515] and Shan Liying
[0830 5461 5391] of the Modern Physics Institute, Fudan University, Shanghai]

[Text]   The constrained optimization method-complex method described in this
paper is better than the simplex method for design of electron optical systems.
This method is beneficial to making optimal automatic search and can ensure
that the computed results will satisfy the design requirement.   In the complex
method as well as simplex method, it is not necessary to know the explicit
functional relation between the objective function and the searching para-
meters.   Comparing with other optimization methods, the complex method and
simplex method have significant advantage in the optimization design of elec-
tron optical systems.   (Paper received May 1984, finalized February 1985.)

References:

[1] P. P. Kas'yankov et al.: Metoday Recheta Electronno-Opticheskikh System, Novosibirsk, Vol. 62, p.68,
     1970.
[2] R. W. Moses: Rev. Sci. Instrum., Vol. 42, p. 828, 1971.
[3] R. W. Moses: Proc. Roy. Soc. (London), A339, p. 483, 1974.
[4] H. Rose, R. W. Moses: Optik, Vol. 37, p. 316, 1973.
[5] P. W. Hawkes: Computer Aided Design in Electron Optics, Computer Aided Design, Vol. 5, p.200, 1973.
[6] E. Munro: J. V. S. T., Vol. 12, p. 1146, 1975.
[7] M. Szilagyi: Optik, Vol. 48, p. 215, 1977.
[8] M. Szilagyi: Optik, Vol. 49, p. 223, 1977.
[9] M. Szilagyi: Optik, Vol. 50, p. 51, 1978.
[10] 华中一、顾昌鑫: 扩展场透镜的计算机分析，上海电子学会1978年年会论文摘要。
[11] 顾昌鑫等: 电子学报，No.2, p. 41, 1984。
[12] J. A. Richardson, J. L. Kuester: The Complex Method for Constrained Optimization, Communications of
     the ACM, Vol. 16, p.487, 1973.
[13] A. B. EL-Kareh, J. C. J. EL-Kareh: Electron Beams, Lenses and Optics, Vol. 2, p.46, 1970.
[14] 上海科学技术情报研究所: 国外电子管概况，p. 143, 1973。

ON-LINE FAULT DIAGNOSIS OF ANALOG IC

[English abstract of article by Zhao Guonan [6392 0948 0589], Xie Shuang [6200 7208], and Guo Yushun [6753 5940 7311] of the Hangzhou Institute of Electronics Engineering, Zhejiang]

[Text] The following new ideas are presented for use in on-line fault diagnosis of analog integrated circuits.

1. The number of fault elements in an analog circuit can be evaluated from the measured data upon the limited number of accessible terminals.

2. The dependent relation between any two multiple-fault sets can be classified in two kinds: the mutual dependence and the single dependence. The routine of on-line fault diagnosis can be accelerated with the use of mutual dependence.

3. The idea of effective measuring ports is helpful to the topological judgment of diagnosability of certain multiple-fault set besides the examination of the existence of loops and cutsets among the fault elements.

4. The uniqueness of the values of certain existing fault elements calculated from the measured data upon the different measuring ports can be used to distinguish the actual fault from the guessed fault.

Program based on the algorithm derived from the above ideas has been proved with success. (Paper received October 1984, finalized April 1985.)

References:

[1] Duhamel et al.: Special issue on automatic analog fault diagnosis, IEEE Trans., Vol. CAS-26, July 1979.

[2] R. Saeks, S. R. Liberty: Rational Fault Analysis, Marcel Dekker, 1977.

[3] W. Hochwald et al.: A DC approach for analog fault dictionary determination, IEEE Trans., Vol. CAS-25, pp. 523--529, 1978.

[4] L. Rapisardo, R. A. DeCarlo: Analog multifrequency fault diagnosis, IEEE Trans., Vol. CAS-30, pp. 432--441, 1983.

[5] H. Navid, A. N. Willson: A theory and an algorithm for analog circuit fault diagnosis, IEEE Trans, Vol. CAS-26, p440, July 1979.

〔6〕 T. N. Trick, C. J. Alajajian: Fault analysis of analog circuits, Proc. of 2oth Midwest Symposium on CAS, Part I, 1977.

〔7〕 R. M. Biernacki, J. W. Bandler: Multiple fault location of analog circuits, IEEE Trans., Vol. CAS-28, p. 361, 1981.

〔8〕 C. C. Wu et al,: Analog fault diagnosis with failure bounds, IEEE Trans., Vol. CAS-29, p. 277, 1982.

【9】 赵国南：模拟电路故障诊断及无接触测试，杭州电子工业学院学报，№.2,1982。

〔10〕 赵国南：端口测试在模拟电路故障诊断中失效的判断，杭州电子工业学院学报，№.2,1983.

〔11〕 赵国南：用线性故障方程的模拟电路在线诊断，杭州电子工业学院学报，№.1,1984。

〔12〕 赵国南、郭裕顺：组件连接模型多频法模拟电路的故障诊断，杭州电子工业学院学报，№.1,1985。

STATISTICAL COMPUTATION OF COMPRESSION RATIO FOR ZERO-ORDER PREDICTOR WITH FLOATING-APERTURE ALGORITHM

[English abstract of article by Guo Guirong [6753 2710 5554] and Shen Qiang [3947 1730] of the Changsha Institute of Technology, Hunan]

[Text] The problem of statistical computation of compression ratio for zero-order predictor with floating-aperture algorithm is considered. Markov Chain is proposed as the model of input process. By this, analytical expressions are derived for the mean and mean-square value of compression ratio, and then a simple and convenient algorithm is developed for the computation of these factors. Finally, several numerical results are given to demonstrate the effectiveness of this approach. (Paper received July 1983, finalized July 1985.)

References:

[1] AD-707333.

[2] L. Ehrman: Analysis of some redundancy removal bandwidth compression techniques, Proc. IEEE, Vol. 55, No. 3, pp. 278-287, 1967.

[3] А. С. Голубков, А. В. Щаронов, С. В. Касаткин: Аналитический метод оценки характеристик одного класса телеметрируемых процессов, Изв. Вузов СССР, Приборостроение , No. 5, Т. 18, 1975.

THEORETICAL ANALYSIS ON INTERMODULATION NOISE IN ANALOG MICROWAVE TRUNKS

[English abstract of article by Yang Yunnian [2799 6663 1628] of the Fourth Research Institute of the Ministry of Posts and Telecommunications, Xian]

[Text] A theoretical formula to explain the intermodulation noise, which is produced by general transmission characteristics with higher terms in an analog microwave trunk, is obtained by use of the Bessel function expression. The usual equations for calculating the intermodulation noise in engineering practice are special cases of the presented formula. To analyze a general transmission characteristic with higher terms in microwave trunk, the least-squared principle is recommended and satisfactory results are obtained. Therefore, a good way to calculate the intermodulation noise in practical transmission systems and to analyze effects of the transmission characteristics in trunk on the FM multiplex telephony signal of radio relay systems are provided. (Paper received July 1984, finalized February 1985.)

References:

〔1〕内野俊治: 通研成果報告, No.6, 1959.
〔2〕松本高士: 电子通信学会志, Vol. 40, No 9, pp.956~961, 1958.
〔3〕R G. Medhurst: PIEE, Vol. 107, No. 11, pp.120~126, March 1960.
〔4〕С. В. Бородич: Электросвязь, No.1, стр. 1~13, 1967.
〔5〕G. J. Garrison: Intermodulation distortion in FDM FM systems--A tutorial symmary, IEEE Trans., Vol. COM-16, April 1968.
〔6〕マイクロ波技術研究会編: マイクロ波通信工学, 昭和47年(1972年)。
〔7〕S. Yonezawa: Microwave Communication, Maruzen Co., TOKYO, 1965.

INPUT METHODS OF CHINESE INFORMATION PROCESSING SYSTEM

[English abstract of article by Zhao Pozhang [6392 3789 3864] of the Beijing Institute of Information and Control]

[Text] The five-layer structure model for Chinese information processing system is proposed, and the features of its input method are discussed. Also presented are the idea of general purpose Chinese character input coding module and the technical feature of natural input method--character recognition and speech recognition briefly. (Paper received May 1985, finalized September 1985.)

References:

〔1〕 赵珀璋：计算机中文信息处理(第二稿)，1~4册，中国科学院研究生院讲义，1984年7月。
〔2〕 中华人民共和国国家标准：GB2312-80信息交换用汉字编码字符集 基本集，技术标准出版社，北京，1981年。
〔3〕 嘎日迪：蒙文信息互换标准代码的设计方案，中文信息处理国际研讨会论文集，第二集，北京，1983年。
〔4〕 金跃中：蒙文信息的基本情况与蒙文八位编码设计方案，武汉工业控制计算机外设研究所资料，1984年。
〔5〕 嘎依提·木沙：维文信息互换标准代码方案设计，新疆维吾尔自治区阿克苏地区行署资料，1984年。
〔6〕 苏丹等：PC-8000(B)微型计算机上维吾尔文、哈萨克文字符号处理系统，新疆大学物理系信息科学研究室资料，1984年。
〔7〕 胡彦发：计算机藏文文字处理系统(ZWCL)简介，甘肃省计算中心资料，1984年。
〔8〕 彭东城等：壮文信息储存与检查，广西民族学院图书馆资料，1984年。
〔9〕 金虎范：微型机多种文字处理系统，中科院沈阳计算技术研究所资料，1984年。
〔10〕 汉傣英电脑处理系统，云南省印刷技术研究所资料，1984年。
〔11〕 李一端：关于联想式半合成汉字输入盘的几点说明，同〔3〕，第一集，pp.117—119。
〔12〕 郭冶方：汉字编码的现状与发展，同〔3〕，第三集，pp.1—15。
〔13〕 胡寅华等：汉字字根编码的探讨，同〔12〕，pp.134—137。
〔14〕 张普：汉字部件分析的方法与理论，同〔12〕，pp.145—153。
〔15〕 盛谦：汉字编码多路输入系统，同〔12〕，pp.177—183。
〔16〕 唐保兴等：汉字结构识别，同〔2〕，pp.129—137。
〔17〕 王绪龙：汉字输入试析，中国仪器仪表学会汉字信息处理系统研究会第一届学术年会论文选集，pp.82—88，杭州，1981年。
〔18〕 李斌：平面联想式汉字编码设计，全国汉字信息处理系统学术会议论文选集，pp.330—332，承德，1982年。

〔19〕石云程：谈谈"整字"输入的前途与字盘方案，同〔17〕，pp. 77—81。

〔20〕张普等：略谈综合键盘设计思想，同〔17〕，pp.59—67。

〔21〕金虎范：脱-联机式笔触汉字输入机，同〔18〕，pp.323—329。

〔22〕竺乃刚等：汉字输入与人机对话，计算机学报，Vol. 1, No.1, pp.33—54, 1978。

〔23〕竺乃刚：联想式汉字处理机，同〔18〕，pp.116—119。

〔24〕赵珀璋等：浅谈汉字拼音输入方案，北京信息控制研究所技术报告，1982年5月。

〔25〕李约瑟，汉语普通话新文字电脑Ⅱ型，南开大学中文信息研究室资料，1980年。

〔26〕丁一亭：四段拼音产生式汉字输入操作方法，杭州自动化研究所资料，1985年5月。

〔27〕王晓龙：汉字输入系统与系列码，哈尔滨工业大学计算机系资料，1985年2月。

〔28〕戴世宗等：字元编码法，长沙工学院计算机研究所资料，1984年4月。

〔29〕王永民：五笔字型计算机汉字输入技术，河南省中文信息开发中心资料，1984年8月。

〔30〕张武田：可读与不可读材料模拟键入的比较研究，中科院心理学研究所资料，1985年3月。

〔31〕彭瑞祥：汉字知觉与机器识别，中科院心理学研究所资料，1985年3月。

〔32〕盛焕烨等：谈谈机助编码，上海交通大学计算机系资料，1983年。

〔33〕许家椂：对汉字编码研究中几个问题的认识，计算机研究与发展，Vol.19, No.1 pp.41—46, 1982。

〔34〕赵珀璋：联想处理技术概述，计算机工程与设计，pp. 21—32. 1982.

〔35〕松本陆：汉字数据输入的动向，日本海外信息合作中日第四次信息合作技术友好代表团演讲录译文集，1983年7月。

〔36〕叶漳民：拼音中文——电算机的自然语言，同〔11〕，pp.48—62.

〔37〕叶漳民，袁晓园：拼音中文——音调制自然语言，同〔11〕，pp. 238—258.

〔38〕顾德义：汉字树形构结中文字母编码法，计算机研究与发展，Vol.20, No.12, pp. 52—56, 1983.

〔39〕肖忠义等：汉字字素编码法，计算机技术，No.2, pp. 54—62, 1983.

〔40〕钱伟长：汉字宏观字形编码，上海工业大学资料，1985年5月。

〔41〕栗兴民，CZ-2汉语词字二元编码方案可行性论证报告，河北邯郸市峰峰矿区第一小学，1985年1月。

〔42〕汉字键盘输入方法评测试行规则，中文信息研究会汉字编码专业委员会第二次学术交流会，福州，1985年5月。

〔43〕杨育彪：一九八四年上海汉字编码评测总结，同〔42〕。

〔44〕林东海等：汉字输入编码的评测，中国船舶工业总公司第709所软件开发中心资料，1985年。

〔45〕龚仁文，陈良志，中文电脑输入方法的春秋战国，资讯与电脑（台湾省），1983年7月。

〔46〕周寿令：低同码形声编码原理提纲，上海电子计算机厂资料，1983年3月。

〔47〕余明江：汉字的"形声编码"方法，浙江镇海县食品公司资料，1983年。

〔48〕许汉杰：音形数字码方案，石家庄铁路分局电子计算所资料，1982年10月。

〔49〕蒋子刚：音形信息兼容码，某部63所资料，1983年。

〔50〕孙钧锡：《汉字基本知识》，河北人民出版社，1980年。

〔51〕胡裕树：《现代汉语》，上海教育出版社，1981年。

〔52〕日本汉字信息处理技术，中国长城工业公司赴日汉字信息处理技术考察组资料，1980年3月。

〔53〕唐治和，皮智远：汉字音意编码输入设计方案，四川永川县城乡建设环保局资料，1984年11月。

〔54〕郁俊夫：汉字字形编码法，无锡电子计算机厂资料，1985年2月。

〔55〕陈明：音形分合码输入系统，上海印刷技术研究所资料，1985年3月。

〔56〕赵珀璋，中文信息处理系统的内部处理码，待发表。

〔57〕中华人民共和国国家标准：GB5199.1～5199.2-85"信息交换用汉字15×16点阵字模集及数据集"，技术标准出版社，1985年。

〔58〕中华人民共和国国家标准：GB5007.1～5007.2-85"信息交换用汉字24×24点阵字模集及数据集"，技术标准出版社，1985年。

〔59〕中华人民共和国国家标准："信息交换用汉字32×32点阵字模集及数据集"，待审定。

〔60〕北京大学计算机科学研究所和山东潍坊电子计算机厂：计算机—激光汉字编辑排版系统，照排控制机研制报告，1985年5月。

〔61〕王选等：高分辨率汉字字形的放大和缩小技术，计算机学报，Vol.7, No.6, pp. 418—426, 1984。

〔62〕程民德等：《图象识别导论》，上海科学技术出版社，1983年。

〔63〕张建平等：通用汉字输入编码模块，待发表。

〔64〕楼世博等：《模糊数学》，科学出版社，1983年。

〔65〕贺仲雄：《模糊数学及其应用》，天津科学技术出版社，1983年。

〔66〕陈贻源：《模糊数学》，华中工学院出版社，1984年。

〔67〕洪岷生：汉字识别的一种笔画抽取方法，厦门大学计算机系资料，1982年。

〔68〕Mao-Che Shi et al.: A Speaker Dependent Mandarin Speech Recognition System, Proceedings of the 1985 International Conference on Chinese Computer, February 26—28, 1985, San Francisco, pp. H-1. 1—1.7.

〔69〕Douglas Van Ziegler: A Microcomputer-Based System for Producing Highly-Intelligible Chinese Speech, Proceedings of the 1985 International Conference on Chinese Computer, February 26—28, 1985, San francisco, pp. E1. 0-E1. 13.

[70] C. T. chang et al.: A Study on Chinese Speech Synthesis in Time Domain by Spell-to-Speech Module, Proceedings of the 1985 International Conference on Chinese Computer, February 26—28,1985, San Francisco, pp. E2.1.

[71] Xu Jin-Pei et al.: Microcomputer-Based Chinese Speech 'Recognition, Proceedings of the 1985 International Conference on Chinese Computer, February 26—28, 1985, San Francisco, pp. E4. 1—4. 13.

[72] K. C. Chang & C. C. Yang: A Real-Time Pitch Extraction and Four-tone Recognition System of Mandarin Speech, Proceedings of the 1985 International Conference on Chinese Computer, February 26—28, 1985, San Francisco, pp. J-1.1.

[73] Chorkin Chan: Intonation recognition of discrete utterances in mandarin, Proceedings of 1982 International Conference of the Chinese-Language Computer Society, Washington, Sept, 1982, pp. 113—121.

[74] Rosa W. Lee & Ching Y. Suen: Distribution of mandarin initials and finals and their representation, ibid [73], pp. 122—132.

[75] Chi-Chang Lee & Hung-Wei Hsa: Speaker-independent recognition of chinese characters, ibid [73], pp. 133—143.

[76] Qichao He: An experiment in chinese speaker identification, ibid [73], pp. 144—154.

[77] Yu Tie-Cheng: Voice input to computers, ibid [73], p.155.

[78] C. H. Chen et al.: Computer speech synthesis and recognition of chinese language based on the Initial-final model, ibid [73], p.156.

[79] Samuel C. Lee et al.: Microcomputer-generated chinese speech, ibid [73],pp 157—168.

[80] L. R. Rabiner & R. W. Schafer: Digital Processing of Speech Signals, Prentical-Hall, Inc., 1978.

[81] Chin-Sung Tang: On the problem of inputting chinese characters, ibid [73], pp. 169—177.

[82] H. C. Tien,: A pinyin-based computer-chinese language system, ibid [73], pp. 178—190.

[83] Jung-tao Hsueh: A chinese Input processor phonetic symbol spelling and character selection, ibid [73] pp. 209—216.

[84] S. Y. Lo: Theoretical limit on the shortest possible input codes for chinese characters, Proceedings of the 1985 International conference on Chinese Computing, San Francisco, February 26—28, 1985 pp.A-3. 1—3.9.

[85] Zwi Barnea & Shui-Yin lo: A simple stroke ordering code and its analysis, Proceedings of 1983 International Conference on Chinese Infomation Processing, Vol. 1, Beijing October, 12—14, 1983, pp.120—132.

[86] H. R. Hwa et al.: A new chinese coding method, ibid [85], pp. 176—193.

[87] C. C. Lee & C. S. Chou: Structure analysis and coding of chinese characters, Proceedings of International Computer conference: Hong Kong 1980, October 12—15, 1980. p.2.1.

[88] T. Y. Kiang & T. H. Cheng: The analysis of chinese characters in terms of basic components, ibid [87], p. 2. 2.

[89] Y. X. Gu et al.: Application of a multilayer decision tree in computer recognition of chinese characters, IEEE Trans., Vol. PAMI-5, No. 1, January, 1983, pp. 83—89.

[90] H. J. Yeh et al.: Application of LPC distance measurement to chinese speech recognition, ibid [87], pp. 7-2, 1—16.

[91] Mao Yu-hang: The realization of machine recognition of handwritten chinese characters, ibid [73], pp. 422—432.

[92] Mao Yu-hang: Machine recognition of chinese characters, ibid [87], pp. 8-1.1—1.8.

[93] Kuoline Chai: Recognition of handprinted chinese characters by theory of fuzzy subsets, ibid [73], pp. 411—421.

[94] K. L. Chai el al. The recognition of chinese characters using black pel density for preliminary classification and amplitude spectrum of projection profiles, ibid [87], pp. 8-2. 1—2. 13.

[95] Xingzhong Zhang & Ying Xia: A method of recognizing handprinted chinese characters By the extraction of an ordered sequence of the straces, ibid [73], pp. 388—398.

[96] W. Y. Kim & S. T. Bow: Preliminary investigation on the structure of Korean characters and their machine recognition, ibid [73], pp. 352—360.

[97] Wen-Hsing Hsu & Fang-Hsuan Cheng: Recognition of handwritting chinese characters by stroke structure analysis method, ibid [84], pp. H-3. 1—3. 6.

[98] Shu Wenhao et al.: A study on on-line handwritten chinese character recognition, ibid [84], pp. H-4. 1—4. 14.

[99] Takao Suzuki: Hangeul Support System: A step to the multilingual system, ibid [84], pp. J3. 1—3. 21.

[100] J. R. Ullmann: Pattern Recognition Techniques, London Butterworths, 1973.

Medicine

OBSERVATION ON RELATIONSHIP BETWEEN MEASUREMENT OF BLOOD FIBRONECTIN AND CLINICAL COURSE OF BURNS

[English abstract of article by Huang Wenhua [7806 2429 5478], Huang Xingyu [7806 5281 3768], and Li Ao [7821 7663] of the First Affiliated Hospital of the Third Military Medical College]

[Text] Blood fibronectin (FN) is a nonspecific opsonic glycoprotein. In the phagocytic and clearing function of reticuloendothelial system, it acts as an important component. It is one of the useful indexes for monitoring critical patients suffering from severe trauma, shock, or sepsis. This paper presents the kinetic changes of blood FN, measured by agglutination assay, in 32 cases of burned patients. The preliminary impression was that the changes of FN titre closely correlated with the conditions of patients. In early postburn period (1 st wk), blood FN reduced markedly, its level paralleled with the severity of injury. In late postburn period, drop of blood FN titre to low level indicated the development of severe systemic and/or local sepsis as well as other complications.

References:

1. 黄文华，等．血中纤维结合蛋白的测定及初步试用于临床病例的观察．第三军医大学学报 1984；6:225.
2. Lanser ME, et al. Opsonic glycoprotein (plasma fibronectin) levels after burn injury: Relationship to extent of burn and development of sepsis. Ann Surg 1980; 192:776.
3. Robbins AB, et al. Clinical response to cold insoluble globulin replacement in a patient with sepsis and thermal injury. Am J Surg 1981; 142:636.
4. Scovill WA, et al. Deficits in reticuloendothelial humoral control mechanisms in patients after trauma. J Trauma 1976; 16:898.

- END -